SYNTHESIS, CHARACTERIZATION AND PROCESSING OF THERMAL MANAGEMENT MATERIALS

A Dissertation
Presented to
The Academic Faculty

by

Daron Spence

In Partial Fulfillment
of the Requirements for the Degree
of Doctorate of Philosophy in the
School of Material Science and Engineering

Georgia Institute of Technology
August 2022

SYNTHESIS, CHARACTERIZATION AND PROCESSING OF THERMAL MANAGEMENT MATERIALS

Approved by:

Dr. Shannon K Yee, Advisor
School of Mechanical Engineering
Georgia Institute of Technology

Dr. Baratunde Cola
School of Mechanical Engineering
Georgia Institute of Technology

Dr. Kyriaki Kalaitzidou, Advisor
School of Mechanical Engineering
Georgia Institute of Technology

Dr. Jaswinder Sharma
Electrification and Energy Infrastructure Division
Oak Ridge National Lab

Dr. Natalie Stingelin
School of Chemical and Biomolecular Engineering
Georgia Institute of Technology

Date Approved: [April 29, 2022]

To my beloved family, Ronald, Barbara, Shawna, Deidra, and Shannon Spence.

ACKNOWLEDGEMENTS

I want to thank my family for their unconditional love, encouragement, and support, which helped me navigate through the difficult times I've experienced during my journey through graduate school. I would especially like to thank my parents, Barbara, and Ronald Spence, for setting an excellent example of being resilient, patient, level-headed, and teaching me to never give up on myself regardless of the adversity. To my eldest sister, Shawna, I'd like to thank you for exemplifying black excellence and exposing me to the extracurricular organizations that fostered my academic growth. To my second eldest sister, Deidra, I'd like to thank you for encouraging me in the moments where I was at my lowest, without knowing you single-handedly kept me together on days I felt like giving up. To my best friend, counselor, heartbeat, and twin sister, Shannon Spence, words cannot describe your importance throughout the process. I am eternally grateful for your unyielding support and affirmations. To my grandmother Melva McFarlane, "you dah my two-five" thank you for your prayers and love. I can't wait to spend more time with you after finishing this accomplishment. To my dearest aunts Claudette, Cherry, Jackie, Cherrymae, Anna, Karen, Kieanna and my godmother Marva thank you for nurturing me. They say, "it takes a village to raise a child" and I am a direct reflection of our selfless love and support. To my uncles Emerson, Dave, Lennox, Richard, Greg and Delvin, and Elroy thank you for all the advice and guidance you've provided throughout my life. I especially want to thank my uncle Paul McFarlane for his daily counsel and friendship. You have been a staple in my life and one of my most significant role models. To my closest friends Marcus Smith, Mark Harris, Tyrrick Nance, Jeramie Humphrey, Shayla Dean, Mark Reyes, Manny Reijer, Terah Rubin, Gordon Victor Fon, Corban Bell, Dion Watson and Duvar

Rutherford, thank you all from the bottom of my heart for your friendship. You all have decorated my life experience with unforgettable memories and have never failed to pick me up when I'm down. To my partner, Bre, thank you for walking with me during this journey's last/most critical leg and reminding me daily that there is always an inherent beauty to life. I am truly blessed to have all of you as my support system. This outstanding achievement would not be possible without you and the individual roles you all have played in my life.

I am very thankful for my mentor and adviser, Shannon Yee. I came to you as an unpolished gem, and you meticulously developed me into a proud, confident, and well-informed graduate student. I am so fortunate and grateful to have had the privilege of being under your tutelage. My matriculation through graduate school has been unconventional. Still, you've seen me through my darkest days by going above and beyond your duties as an advisor, and I cannot thank you enough for your dedication, patience, and direction. I am also grateful to my MSE and industry advisors, Kyriaki Kalaitzidou and Jaswinder Sharma, for their guidance and encouragement. I am very thankful to my committee members, Natalie Stingelin and Baratunde Cola, for their support. I want to thank my fellow NEST and STEEL members past and present for their valuable friendship; Erik, Zhe, Ali, Tom, Matt, David, Sampath, Andrey, Bettina, Sonja, James, Alex, Josh, and Frank. I want to thank my lab mates Jordan, Mike, Eric, Amalie, Shawn, and Aravindh for their selfless willingness to teach me the concepts I needed to navigate through this program successfully and for genuinely being invested in my personal growth. I am humbly indebted to everyone mentioned in these acknowledgments and hope to one day reciprocate all the love and support you all have poured into me to make this achievement possible.

TABLE OF CONTENTS

LIST OF TABLES

LIST OF FIGURES

LIST OF SYMBOLS AND ABBREVIATIONS

R	R-value of insulation
l	Thickness
k	Thermal conductivity
k_{gas}	Modified thermal conductivity of the gas
$k_{gas,0}$	Free volume thermal conductivity of the gas
β	Energy transfer parameter between gas and solid
Kn	Knudsen number
l_{gas}	Mean free path of the gas
d_j	Diameter of the pore
k_{eff}	Effective thermal conductivity
k_{sol}	Thermal conductivity of the solid
k_{gas}	Thermal conductivity of the gas
k_p^{ITR}	Thermal conductivity of the particle with interfacial thermal resistance
k_m	Thermal conductivity of the matrix
k_s	Thermal conductivity of the shell
k_c	Thermal conductivity of the core
α	Kapitza resistance term
v	Geometrical factor
r	Radius
t	Thickness of the shell
R_{Bd}	Contact parameter

n_L	Refractive index of the low index material
n_H	Refractive index of the low high material
d	Thickness
m	Integer constant
λ	Wavelength
λ_0	Operating wavelength
d_L	Thickness of the low index material
d_H	Thickness of the high index material
π	Pi constant
Γ	Reflectivity
n_a	Refractive index of the initials medium
n_b	Refractive index of the back medium
λ_1	Left bound bandwidth wavelength
λ_2	Right bound bandwidth wavelength
ΔG	Gibbs free energy
ΔG_{mixing}	Gibbs free energy of mixing
$\Delta G_{elastic}$	Gibbs free energy of elasticity
v_2	Volume fraction of the swollen polymer
X_1	Flory- Huggins interaction parameter
M_c	Molecular weight between chains
M	Molecular weight
s	Refractive index of glass
$n(\lambda)$	Index of refraction at a given wavelength
$T_{\mathrm{Min}\ (\lambda)}$	Minimum transmittance at a given wavelength
$T_{\mathrm{Max}\ (\lambda)}$	Max transmittance at a given wavelength

d_f	Thickness of the film
$h_{o(L)}$	Height of the low index dip coated film
$h_{o(H)}$	Height of the high index dip coated film
η	Viscosity
U_0	Withdrawal speed
Υ	Surface tension
h_o	Height of the dip coated film
ρ	Density of polymer
g	Gravitational constant
c	Constant
T_K	Temperature in Kelvin
R	Resistance
ΔT_{s+f}	Change in temperature of the substrate and film
ΔT_s	Change in temperature of the substrate
P	Power
b	Half width of the heater line
L	Length
k_f	Thermal conductivity of the film
V	Volume
u	Energy density
ξ	PCM usable volume

SUMMARY

Due to increasing average global temperatures, the energy used for space cooling in buildings will increase by 300% by 2050 and account for 13% of all electricity usage worldwide. Consequently, to meet global cooling demand, fossil fuels and refrigerants, which release carbon dioxide and volatile chemicals with large global warming potentials, will be used at higher rates. This increase in greenhouse gas emissions results in a growing demand for space cooling. Several energy consumption models indicate the importance of reducing energy usage to slow the rate of global warming.[1] Improving the performance of thermal materials can directly reduce the amount of energy required for space cooling by reducing the thermal load on buildings.[2]. Therefore, the synthesis, characterization and processing of passive and dynamic thermal management materials will be critical in efforts to reduce these thermal loads in buildings.

In this thesis, the theoretical framework that predicts the effective thermal conductivity of superinsulating hollow silica nanoparticles in a binary matrix is first presented. Discussion of the framework is then followed by the synthesis process needed to achieve the designated particle parameters. Additionally, electromagnetic properties of thin films are presented to inform the design parameters for dielectric mirrors. This thesis addresses four specific questions to contribute to working scientific knowledge of passive and dynamic insulating materials. First, a parametric study was completed to investigate the physical parameters that govern the effective thermal conductivity of hollow silica nanoparticles. Second, the thermal assessment of ternary composite materials consisting of hollow silica nanoparticles with carbon fillers in between particle clusters was evaluated. Third, the means for characterizing the mechanism and degree of thermal switchability

achieved by polymer dielectric mirrors used to variably reflect solar radiation over a tunable range was elicited and detailed. Lastly, *in-situ* techniques to characterize the dielectric mirror's thermal conductivity and chemical state as a function of switching degrees is presented. The thesis provides a deeper understanding of the relationship between hollow silica nanoparticles design and performance and provide necessary information to further develop the foundation of thermally switching used for dynamic thermal conduction and radiation management.

CHAPTER 1. INTRODUCTION

1.1 Motivation and Background

According to the United States Energy Information Administration, carbon dioxide (CO_2) emissions are projected to increase by 15% as a byproduct of meeting projected energy demands by 2050. This increase in energy demand is expected to produce an output of approximately 42 billion additional metric tons of CO_2 by that time, resulting in higher greenhouse gas emissions that further exacerbate global warming.[1] Average global temperatures have already increased by 1 °C over the past century.[2] This increase in temperature has intensified natural disasters begetting, among other issues, unprecedented weather anomalies, historical flooding and droughts, and the destruction of marine ecosystems. These environmental catastrophes are expected to worsen given that the average global temperature is expected to rise by another 1.5 °C to 3.5 °C by 2050.[3-5]

Moreover, this unprecedented rise in global temperatures will cause social strain by making habitation in tropical and subtropical climate zones unfavorable due to the growing number of lethal heat wave anomalies and destruction of inhabitable regions through flooding. In the latest Groundswell report released by the World Bank it was reported that nearly 216 million people will be forcibly displaces by these changes and become climate refugees.[6-8] This migration towards natural or synthetically cooler regions inherently contributes to a negative feedback loop from an energy perspective as the population density increases in more developed cities.[9] Increasing energy demands, which elicit projected global temperature rise, are driven by two main factors: population increase and an increase in global living standards. The human population is projected to increase by

28%, from 7.8 to over 9 billion, within the next 20 years.[10] This population increase is expected to be concentrated in countries with rapidly developing economies and five of the world fastest growing economies are located in tropical or subtropical climate zones, regions that are projected to bear the brunt of the aforementioned migration of humans seeking more favorable living conditions.[11-14]

An increase in the standard of living, from an energy perspective, is characterized in the form of access to electricity, transportation, and increased electrical and gas usage. Efforts to reduce population and thus reduce necessary energy resources as seen in China's failed "One Child Policy" proved to have substantial negative consequences on the country's economy due to a decrease in workers to support social securities needed by the aging citizens.[15] Although clean energy offers humanity a solution to reduce our carbon footprint, its usage is only expected to meet approximately 50% of the world's energy needs by 2050.[16]

This increase in the use of renewable energy is not substantial enough to reach global goals to reduce carbon emissions as outlined in the 2016 Paris Agreement.[17] According to the NDC Synthesis Report release by the United Nations Climate Change Committee an immediate transformation to reduce the use of greenhouse emitting forms of energy generation is critical to simply achieve the lower 1.5 °C bound of our climate increase projection.[18] Specifically, the report indicates that the total reduction in greenhouse gas emissions in countries that account for 30% of all global emissions is on pace to be less than 1% by the year 2030.[19] The Intergovernmental Panel on Climate Change puts this projected reduction in perspective in their Special Report on Global Warming by indicating that there needs to be at minimum a 45% global reduction in CO_2

emission in order to reach the lower limit global temperature increase of 1.5 °C.[20] Therefore, it is imperative that we implement a new degree of efficiency standards in order to reduce the amount of energy required to maintain our growing standard of living and circumvent emitting higher quantities of greenhouse gasses into the atmosphere.

1.1.1 The rise in demand for global cooling

"Growing demand for air conditioners is one of the most critical blind spots in today's energy debate. Setting higher efficiency standards for cooling is one of the easiest steps governments can take to reduce the need for new power plants, cut emissions and reduce costs at the same time."- Faith Birol, IEA Executive Director

The imminent increase in global energy demands will be dominated by the desire for electricity, making this a prime area to implement energy-saving technologies. It is known that buildings currently consume nearly one third of all global electricity produced and corresponds to nearly 38% of all CO_2 emissions.[21] More specifically, the growing global demand for space cooling is projected to consume 13% of the world's electricity and is will be the largest end use application of energy in residential and commercial building.[22] Although air conditioning manufactures strive to make continuous improvements to the efficiency of this product, the number of units produced will increase rapidly from 1.6 to 5.6 billion, corresponding to 2 billion metric tons of CO_2 emissions by the year 2050.[23]. Figure 1 illustrates the breakdown of energy consumption of building structures by the year 2050 and clearly shows that space cooling and heating will account for nearly 50% of all energy consumed by in buildings globally.[24] Air conditioning efficiency is commonly assessed using the Seasonal Energy Efficiency Ratio (SEER) and

is a numeric efficiency value given by dividing the number of British Thermal Units (BTUs) of heat removed from a space by the total energy required by the air conditioner in watt-hours. As AC efficiency standards increase, additional improvements

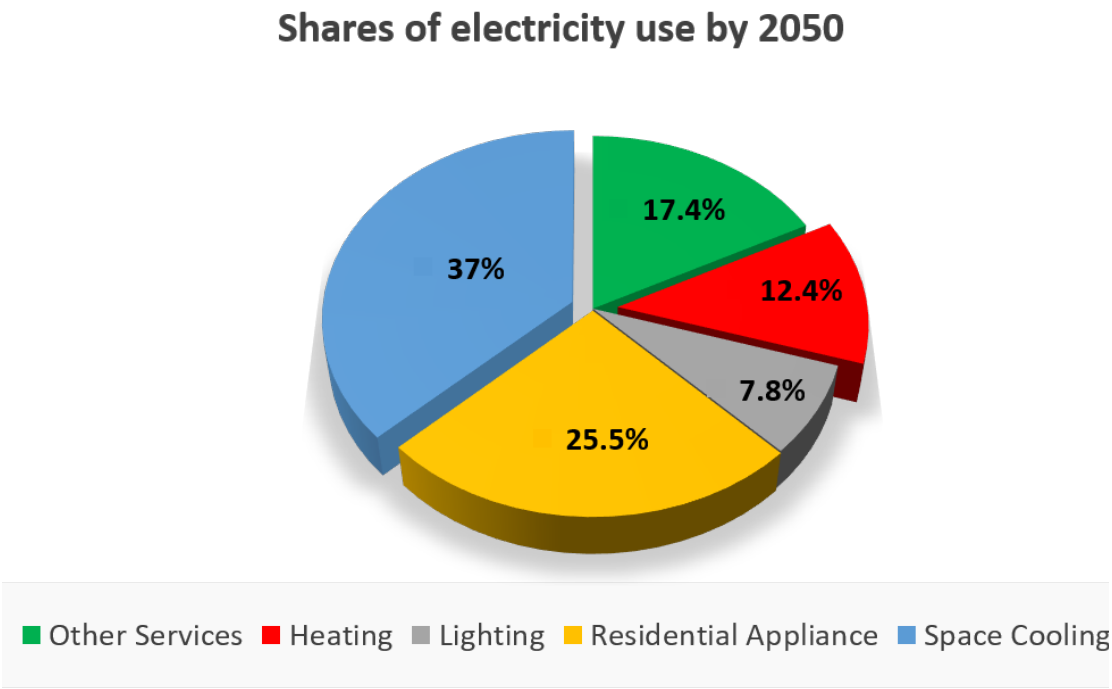

Figure 1 Shares of electricity use in building structures by the year 2050 as reported in the 2019 Future of Cooling report by the Energy Information Agency.

to building insulation and radiative load management in these spaces will be critical for reducing the thermal load on building envelopes. The pertinent types of thermal loads on building are identified and discussed in relation to mass insulation materials and reflective materials that maybe used to reduce the amount of heat transferred through building envelopes. This reduction directly corresponds to the amount of heat needing to be displaced by cooling units to achieve both comfortable and save dwelling conditions.

Specifically, the dominant and most relevant forms of heat transferred into these spaces occur through conductive and radiative pathways.[25, 26] In a typical American residential building heat is primarily conducted through walls, attics, floors and window frames.[27-30] Meanwhile, radiative thermal loads on building envelopes predominately result from reemission of solar radiation through the roof and transmission through transparent medias such as windows and skylights. Additional radiative contributions to the thermal load on buildings come from the effective radiation contribution from other solid structures such as window frames and door fixtures.[31-34] This effective radiative contribution to the thermal conductivity of the insulation materials is critical to address. Moreover, this body of work addresses the dominant forms of thermal loads on building envelopes by assessing conventional and state-of-the-art conductive and radiative building insulation to elicit key characteristics for next generation materials. Brief cost analysis reports are also presented in this work but it is important to note that they only encompass the marterial cost and not the full cost of integration, i.e., analysis of the supply chain and labor will not be discussed in this dissertation. Specifically, this thesis will provide information that may lead to the use of alternative building insulation materials that can be used to curtail the growing energy demand needed for space cooling.

1.1.2 Insulation building materials

Altering conventional thermal insulation materials currently used in building envelopes is a simple yet highly effective way to reduce heat transfer between the environment and building structures. Common materials used as thermal insulation are cellulose, material wool, glass fibers, extruded polystyrene and polyurethane foams.[35] These traditional thermal building insulation materials are produced as matts and boards

and are inserted as fitted panels, loose foam fillers, batts or blankets into cavities between walls, underneath floors, and in attics.[36] All building insulation materials are classified by their R-value, a measure of thermal resistance, which is inversely related to the thermal conductivity of the insulating material (Eq. 1).

$$R = \frac{l}{\kappa} \tag{1}$$

Conventional materials currently used in a majority of building insulation application have thermal conductivities that typically range from 0.026 to 0.04 $Wm^{-1}k^{-1}$.[35] Reducing heat loss through conventional insulation materials in building envelops can significantly reduce the total thermal energy lost through the structure by 35%, meaning engineering and implementing new materials with even lower thermal conductivities can further drive energy saving.[37] A table of conventional thermal insulation materials and their corresponding conductivities is provide in section 1.2.1.

1.1.3 Reflective building materials

Unlike conductive heat transfer through walls, floors and ceilings, radiative heat transfer in building envelopes occur through reemission of thermal energy into the structure resulting from temperature differences caused by direct exposure to solar radiation. Solar radiation through roofs and windows make up the primary areas for radiative transport in building structure.[38] Specifically, dark colored roofs heated by the sun absorb thermal radiation and a temperature gradient is created between the outside rooftop and the attic of the building envelop causing heat to flow into the dwelling. This effect has been shown to be directly correlated to the roofing material and its color.[39] On a fundamental level

radiative absorption in building materials can be modulated by simply changing the pigment of the materials. In a study by Li, Xiangyu, et al. it was reported that the passive technique of radiative cooling using ultrawhite BaSO4 paints reflect up to 97.6% of all incoming solar radiation resulting in a net cooling effect of up to 4.5°C compared to ambient conditions. Figure 2 shows the scanning electron microscope image of BaSO4 films and paints along with a schematic representation and spectral emissivity/absorptivity data of the material against solar irradiance from 0.25 to 20 µm.[40]. It is clear in the spectral image that both the paint and thin film material do not absorb or emit along most of the wavelengths associated with thermal heat gain from the sun but instead reflects this

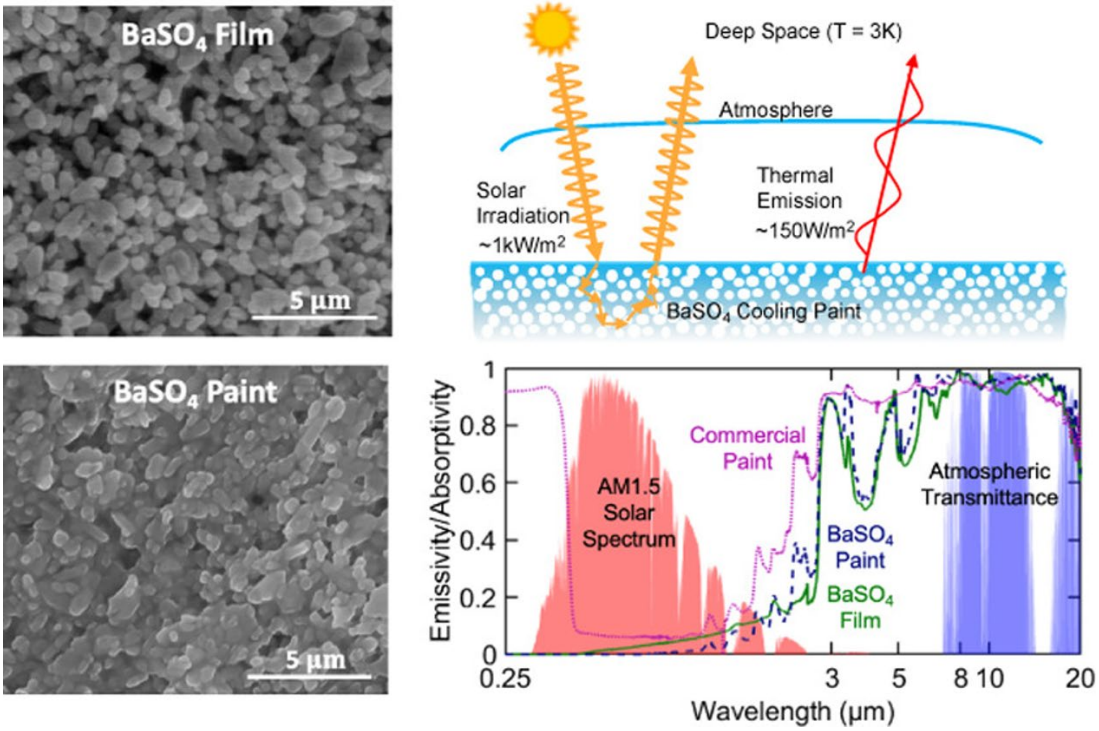

Figure 2 Scanning electron microscope image of $BaSO_4$ films (top left) and $BaSO_4$ paint (bottom left). Schematic representation of the reflection of incoming solar irradiance a thermal Emission of the $BaSO_4$ paint (top right). UV-Vis -Near IR emissivity/absorptivity spectral data of the $BaSO_4$ film (green), $BaSO_4$ paint (purple) and solar spectrum (pink) from 0.25 to 20 µm. [39]

thermal radiation back into deep space as shown in the cartoon schematic in the upper right-hand corner.

In contrast, thermal radiation transmission through clear mediums such as glass windows or skylights also serve as significant radiative thermal loading sites and represents 20 – 40% of total radiative thermal loads transferred through building structures.[41] This occurs because conventional glass can transmit up to 92% of visible and IR radiation. The transmitted radiation is then directed, absorbed, collected, and re-emitted by the window and its fixtures, while the transmitted radiation passes through and is absorbed by materials inside the building before being re-emitted. In contrast, low-emissivity (low-e) windows, first engineered at the Lawrence Berkeley National Laboratory in the mid-1970s, reflect large, fixed portions of non-visible thermal radiation, resulting in a reduction of thermal energy loads that need to be dissipated. These low-e windows are currently used globally in modern energy efficient buildings but possess several shortcomings that remain the focal point of current research. The new developments and shortcomings of state-of-the-art low emissivity reflective shields and window coatings will be discussed in section 1.2.2.

1.2 Previous Research

1.2.1 State-of-the-art insulation materials

Except for vacuum sealed panels, all thermal insulation materials contain large quantities of stationary trapped air, which makes heat transfer through convection negligible and significantly impedes the transfer of thermal energy through conduction. Among this class of materials exist super-insulating materials with thermal conductivity below that of ambient air. Low-density silica aerogels have emerged as a promising super-

Table 1 Conventional building material compared to state-of-the-art insulation material used in buildings. The thermal conductivity is given in milli Watts per meter Kelvin and is shown along with the mechanical performance, elemental resistance, qualitative cost, environmental impact, and inference of future use as thermal insulation materials.

Material	Thermal Conductivity (mWm^{-1K-1})	Cutting to adapt for construction (Performance if perforated)	Resistance to fire, water, and chemicals	Cost per thermal resistance	Environmental impact of production and use	A thermal insulation materials and solution of tomorrow
Conventional Insulation materials						
Mineral Wool	30-40	Yes (Same)	Low	Low	Low	No
Expanded Polystyrene	30-40	Yes (Same)	Low	Low	High	No
Extruded Polystyrene	30-35	Yes (Same)	Moderate	High	High	No
Cellulose	40-50	Yes (Same)	Low	Low	Low	No
Polyurethane	20-30	Yes (Same)	Moderate	High	High	No
State-of-the-art-insulation materials						
Vacuum Insulation panels (VIP)	4-8	No (Worse)	Low	High	Moderate	Near future
Gas- Filled panels	10-40	No (Worse)	Low	High	Moderate	No
Aerogels	10-20	Yes (Same)	Moderate	High	Moderate	Possible
Nano insulation materials (NIMS)	<4	Yes (Same)	Moderate	High	Moderate	Yes

insulation material due to their low thermal conductivity (0.014 Wm^{-1}-K^{-1}), making them nearly 3 times more insulating in comparison to conventional building insulation materials such as fiberglass and expanded polystyrene (Table 1).[36] This super-insulation material exploits nanoscale features that maximize trapped air volumes in their structure and compartmentalizes these air pockets to leverage the Knudsen effect. Explicitly, the Knudsen effect describes the reduction of the thermal conductivity of gas in a composite matrix that is trapped it in features less than or within the same order of magnitude of the mean-free-path of the gas.

Equations 2 describes the reduced thermal conductivity of the gas as a function of the free volume thermal conductivity of the gas $k_{gas,0}$, the energy transfer parameter β and the Knudsen number K_n.[42]

$$k_{gas} = \frac{k_{gas,0}}{1 + 2\beta Kn} \tag{2}$$

The energy transfer term parameterizes the gases interaction with the solid microstructure. Equation 3 describes the Knudsen number and is expressed to be a function of the mean-

$$K_n = \frac{l_{gas}}{d_j} \tag{3}$$

free-path l_{gas} of the gas and the inner and intra pore lengths d_j of the hollow silica nanoparticles system. Figure 3 shows the pore size effect on the effective thermal

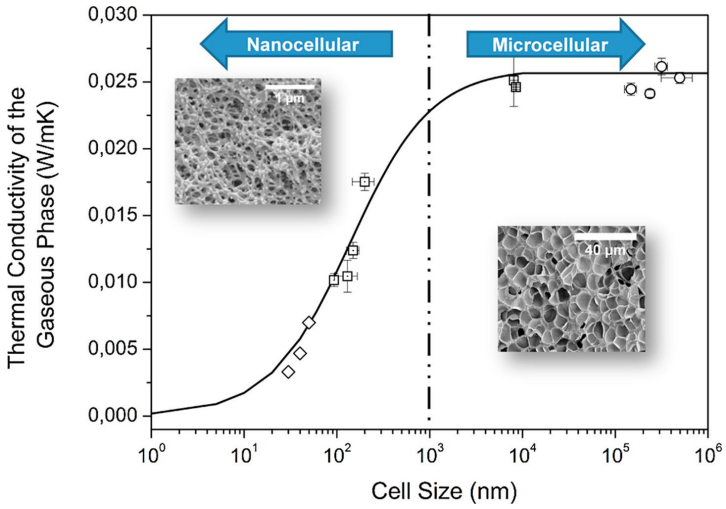

Figure 3 Effect of the cell size on the gas thermal conductivity in open cell polymeric foams together with the theoretical predictions obtained from the Knudsen equation, and some of the previous results in aerogels [42]

conductivity of gas that is entrapped in micro and nanocellular pores. [42] It is clear from this figure that a reduced thermal conductivity of the gaseous phase first starts to appear when the cells size is reduced below 1000 nm. [43]

However, silica aerogels are also 10 times more expensive to fabricate than commonly used thermal insulation materials which are currently used to insulate 85% of building structures globally.[44] The high cost associated with fabricating silica aerogels stems from the need for expensive precursor materials and an energy intensive supercritical drying step needed to remove the organic scaffold holding up the material. Therefore, applying this insulation material to new or existing building envelopes to reduce energy consumption is economically unfeasible.

By utilizing relative aerogel characteristics which give the material its unique properties, nano insulation materials can be formed using hollow silica nanoparticle. Nanoscale materials have previously been associated with a high cost per thermal resistance units, but other work (detailed in section 1.2.3) has demonstrated fabrication techniques to make these materials economically feasible. Hollow silica nanoparticles have shown promising characteristics which support their usage as super-insulators such as mechanical robustness and economically feasible fabrication. Hollow silica nanoparticles materials possess high surface areas, high system porosity and low densities making them ideal for thermal insulation.[45] Thermal conductivity values as low as 0.014 $Wm^{-1}K^{-1}$ have been reported in these systems, however, a critical analyses of detailed geometrical parameters which align with current effective thermal conductivity models are missing from the literature. Additionally, the incorporation of materials used to slow the transport

of radiation through low density silica composite systems has yet to be fully explored and is critical to better understand the insulative capabilities of these material systems. [46]

1.2.2 State-of-the-art reflective materials

Current research conducted on reflective insulation for buildings focuses on materials with low emissivity commonly made from aluminium foils, reflective ceramics paints, reflective shingles, and metal oxide thin films.[47] These materials are used to create radiant barriers capable of reflecting large amounts of thermal radiation back into space as seen in the top right illustration of Figure 2. Heat gain and loss through roofs account for 25% of the radiative load on the structure.[48] Roof applications such as aluminium laminated panels that entrap air to reduce convective and conductive heat transfer have long been used to reduce heat flux by up to 88% in tropical climates.[49] Polished aluminium has low emissivity ranging between 0.03 and 0.05 and reflects over 95% of solar radiation along a broad spectrum, making metal foil based technology a cheap and effective way to reflect thermal radiation in building components that are not transparent.

More recent research on reflective coatings used in building technologies have focused on the implementation of dynamically tuneable semi-transparent and transparent materials. These materials are more applicable in managing the radiative heat loads through transparent media in building structures. Common examples of these materials consist of metal oxide low emissivity coatings, hydrogels and ceramic thin films. Kevin Shopsowitz reported on the capability of free-standing mesoporous silica films to serve as dynamic reflective materials for smart window applications. These materials are capable of

changing microstructure by absorbing isotropic liquids that change their chirality to become completely colourless and transparent.[50] Other prominent research on dynamic reflective coatings have been used with polymer based thermochromic materials to create smart windows and have been shown to reduce the annual HVAC energy consumption by up to 37.4% compared to traditional low-E glass savings of 11%.[51] Figure 3a shows the ability of these materials to transmit reduced amounts of solar radiation over the visible and near IR wavelengths as the temperature is changed to 40 °C. The image clearly illustrates that responsive thermochromics are capable of regulating cooling requirements by modulating solar radiation transmission through window structures.[51] Further evaluation of these materials can be seen in Figure 3b as the luminance transmittance and change in solar transmittance of the thermochromic materials are compared to the properties of low-E windows and regular glass. Low-E windows and clear glass lack thermochromic response, so they are unable to modulate the degree of thermal radiations. The chromatic switchablity of these materials can be seen in Figure 3c. Standard images show that as the temperature of increases the transparency of the polymer decreases. This occurs due to changes in the microstructure of these materials as shown in the SEM images and shows the material thickening at higher temperatures and results in larger degrees of light scattering. Finally, the absorptivity/emissivity spectra for these materials were compared to that of normal glass, low-E coating, and high-E HPC hydrogel (at 20 °C and

40 °C) along with IR images for the low-E side (left) and high-E side (right) of TET smart window at 40 °C, 35 °C and 28 °C, respectively.

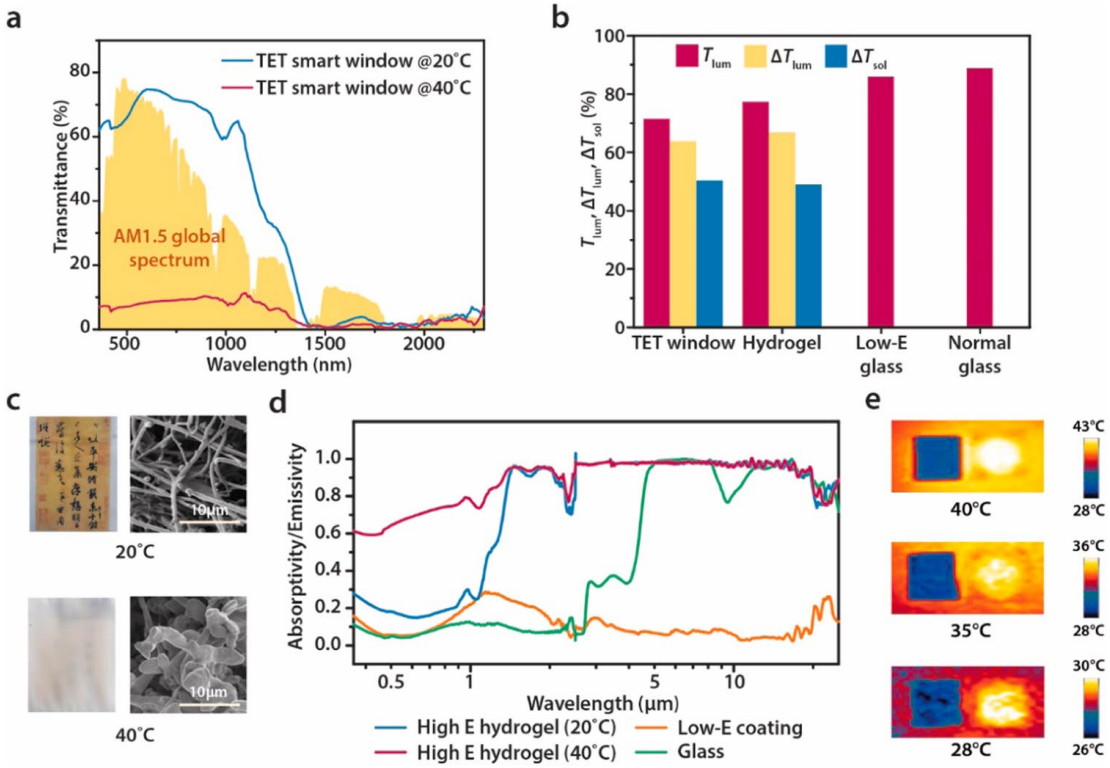

Figure 4 (a) UV-Vis-NIR spectra for the TET smart window at 20 °C and 40 °C, respectively. The yellow shade in the figure represents the normalized AM 1.5 global solar spectrum. (b) Comparison of optical properties (T_{lum}, ΔT_{lum}, and ΔT_{sol}) for the TET smart window panel, pure hydrogel, low-E glass, and normal glass. It should be noted that ΔT_{lum} and ΔT_{sol} for low-E glass and normal glass are 0% as they do not have thermochromic properties. (c) Photo of TET smart window (left) and SEM image for the hydrogel (right) at 20 °C and 40 °C, respectively. (d) Absorptivity/emissivity spectra for the low-E coating, high-E HPC hydrogel (at 20 °C and 40 °C), and normal glass. (e) IR images for the low-E side (left) and high-E side (right) of TET smart window at 40 °C, 35 °C and 28 °C, respectively.[51]

1.3 Thesis Questions

The thesis experimentally identifies the degree to which spherical shell to core ratios of hollow silica nanoparticles align with effective thermal conductivity models of hollow particles to better demonstrate and inform practical applications. Additionally, it characterizes the thermal properties of ternary phase composites to evaluate the effects of solid material additives in hollow silica nanoparticle matrices. This thesis also explores the switching mechanism of polymer-based dielectric mirrors, referred to as distributed Bragg Reflectors, to experimentally resolve the entropic balance between the free energy of mixing and elastic stresses, which govern dynamic film properties. Lastly, this thesis investigates changes to the films microstructure and chemical state and discusses its effect the thermal conductivity of the material. This thesis will herein conclude answers to the scientific questions below:

I) Which spherical shell to pore ratio optimizes the effective thermal conductivity of hollow silica nanoparticles?

Effective medium theory provides a first approximation of composite material properties. It is a weighted average of material property values of each component in the composite system. Composites with nanosized features have lower effective thermal conductivity values compared baseline predictions because of interfacial thermal resistance between particles and nanoscale confinement of the gaseous species. This thesis work demonstrates the effective thermal conductivity of synthesized hollow silica nanoparticles using parametric studies and experimentally investigates material properties as a function of fabrication parameters to better inform practical hollow silica nanoparticles design.

II) To what degree does the addition of carbon black affect the thermal transport in a hollow silica nanoparticle matrix when dispersed in interstitial sites?

Air is the largest constituent in these semi-transparent hollow silica nanoparticle systems. Low density carbon black fillers were added to the matrix and its impact on the effective thermal conductivity were measured. Changes to the thermal characteristics are attributed to manipulating the Knudsen effect and changing the amount of interfacial scattering sites. The filler material also has radiative properties which impede the transport of radiative heat through the matrix, however the filler material has a greater thermal conductivity than the gas it is replacing. As the loading fraction of filler material increased, the volume fraction of the solid materials in the matrix eventually dominates the effective thermal conductivity. This thesis identifies the key composite parameters and explain the thermal transport mechanisms in ternary systems.

III) To what degree can the crosslink density, determined by the Flory Rehner model for polymer swelling, and humidity levels be used to tune the dynamic optical behavior in dielectric mirrors?

Hydrophilic polymers used to construct photonic mirrors swell in the presence of non-orthogonal solvents until the entropy of mixing balances with elastic stresses. The Flory-Rehner relationship evaluates the degree of swelling in discrete ratios between a dry and swollen film. Swelling ratios depend on intrinsic material properties such as the crosslink density and the concentration of solvent molecules surrounding the matrix. Experiments in this thesis characterize the degree of tunability over optical constants that determine the

reflective band's location and magnitude. This work can be used to inform dielectric mirror configurations to maximize energy savings in different climates.

IV) To what extent can the effective thermal conductivity of dielectric mirror layers be altered as a function of crosslink density and exposed to humidity?

The effective thermal conductivity of dielectric mirrors is hypothesized to increase as a function of solvent uptake resulting from polymer swelling. Swelling characteristics derived from the previous question provide dynamic film thickness and refractive index changes of the material as it is exposed to various solvent concentrations. This thesis identifies the degree of mass uptake, changes to the microstructure, and corresponding changes in the chemical state of the film in relation to its effective thermal conductivity

CHAPTER 2. HOLLOW SILICA NANOPARTICLES

Hollow silica nanoparticles are explored as alternatives to aerogels. Hollow silica particles with a thermal conductivity of ≈0.02–0.03 $Wm^{-1}K^{-1}$ have been reported [52] These particles can be used as standalone thermal insulation materials, or they can be mixed with other materials to form composite thermal insulation materials.[53-55] Note that other microstructures (*e.g.,* fibers, foams) will not lower the thermal conductivity of another materials when mixed to form composites, rather they can increase the thermal conductivity of the composite system.[56, 57] Therefore, hollow silica particles are a universal thermal insulation material that can be used alone or in combination with other materials. The governing principle used to predict the effective thermal conductivity in these systems is given by Equation 4 which shows that the effective thermal conductivity (k_{eff}) is a function of the gaseous thermal conductivity (k_{gas}) and the thermal conductivity of the solid (k_{sol}). The modification of these two parameters as they relate to the geometrical parameters of the system will be discussed in section 2.2.1.

$$k_{eff=}k_{sol+}k_{gas} \tag{4}$$

2.1 Material Cost Reduction

Unlike silica aerogels, sacrificial organic scaffolds used to form the hollow nanoparticle structures can be tuned within tens of nanometers and permit controlled analysis of the material's thermal properties as a function of geometrical parameters. The effects of altering these geometrical parameters are discussed in detail in section 2.4. Prior to optimizing the synthesis and physical characteristics of the hollow particles, a thorough

study was completed to assess the material cost of hollow silica nanoparticles as insulation materials. [52]

Specifically, processing hollow silica particles does not require the use of supercritical drying to remove the organic scaffold which supports the structure. This is the most energy intensive portion of creating aerogels, therefore, hollow silica nanoparticles were demonstrated to be fundamentally more economical than silica aerogels. Instead, polymer cores can be removed using recycled thermal energy or solvents. [53] Furthermore, the chemical solutions needed to fabricate hollow silica nanoparticles can be purified, recycled, and readjusted to reduce the cost of fabricating the insulation material as seen in Figure 4. In detail after the shell formation, the core-shell particles settled down at the bottom of the reaction mixture container and could be easily separated from the supernatant reaction mixture either by decantation or centrifugation. After the core-shell particles were collected through centrifugation, the supernatant was used again to synthesize the next batch of core-shell particles by bringing the pH back to 11 (any value >10.5 gives similar results). It was observed that the pH had dropped from 11 to ≈9.0 by the end of the synthesis cycle, thus, the pH of the supernatant after a synthesis cycle was lower than that of the initial reaction mixture. The reduction in the pH resulted from (1) evaporation and (2) consumption of ammonia as the reaction proceeded. About 85% of the solution was retrieved at each step via centrifugation, although it was noted that up to ≈95% of the solution could be retrieved. The centrifugation and supernatant use cycle were repeated three times. In each step, the amounts of PS particles and TEOS were varied to make the proportional amounts the same as in the original reaction mixture. SEM imaging showed that the quality of the particles synthesized remained the same in all iterations.

Therefore, the entire process was highly useful for increasing the number of hollow particles obtained without wasting solvent and, thus, for lowering the process cost.

Using the same 100 mL solvent (isopropanol), approximately 75 cm3 of hollow silica particles were obtained, and the supernatant could still be used to synthesize the next batch of particles. Note that previously reported methods provide less than 3 cm3 of hollow silica particles/100 mL of solvent. [54, 55] Therefore, our approach provided ≈25 times more hollow silica particles for the same amount of solvent if the solvent was recycled three times. However, it was calculated that, assuming 85% reaction solution recovery after each iteration (a conservative estimate, as 95% of the solution can be recovered) and extrapolating the number of iterations to six (after which the amount of reaction solution drops to about 50 mL), about 125 cm3 (40 times more than the previously reported methods) of particles can be obtained from the same reaction mixture (100 mL isopropanol + 30 mL water) just by adjusting the pH and adding additional TEOS. Figure 5a shows the schematic of reaction solution recycling, and Figure 5b–d are SEM images of hollow particles obtained from the original synthesis cycle, the first iteration, and the second iteration respectively.

To estimate synthesis costs, costs and quantities of the different chemicals used in this work were compared with the extrapolated amounts of chemicals that will be used in the reported works to obtain the 0.093 m2 × 1 cm of particles.[52] Table 2 illustrates an estimated cost analysis of hollow particle synthesis. Cost estimates show that 0.093 m2 × 1 cm particles can be obtained at a cost of $1.30 by using ORNL strategy of processing solution recycling while other reported methods provide the same number of particles at a cost of approximately$15. For cost analysis purposes, 130 g of polystyrene particles can

be added to 2860 mL of solution (2000 mL isopropanol or ethanol + 860 mL water), followed by the addition of ammonium hydroxide and 110 mL of TEOS. After silica shell formation, ~2450 mL of solution (~1700 mL of isopropanol or ethanol) can be retrieved. Therefore, only 300 mL of isopropanol or ethanol will be lost by using ORNL processing

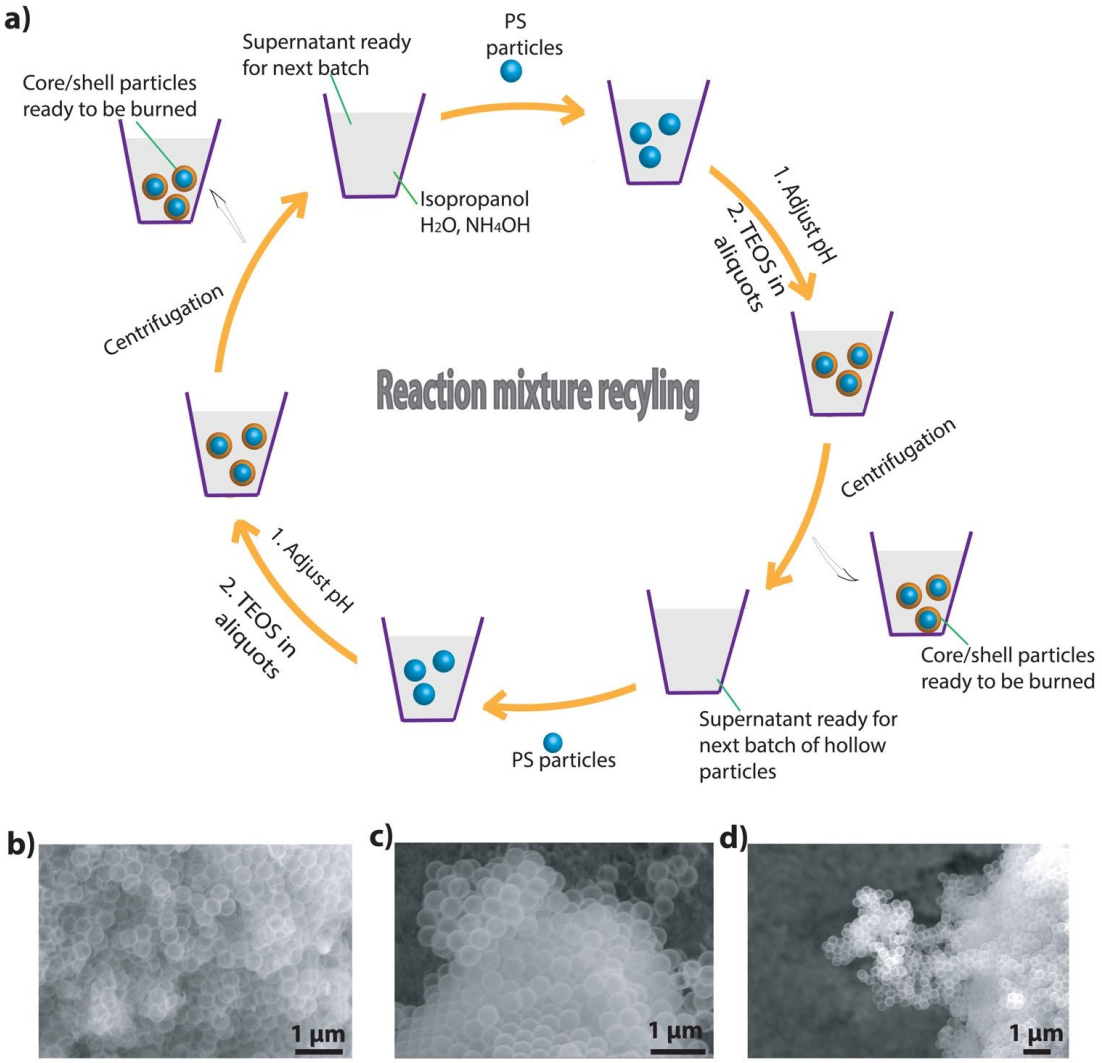

Figure 5 Recycling of the reaction solution. (a) Schematic showing the recycling steps. SEM images of the particles synthesized by (b) the original reaction mixture, (c) the first reiteration, and (d) the second reiteration. Note: The process was repeated only three times in this work, but the retrieved solution can be used for several more reiterations if the pH is maintained.

Table 2 Cost analysis of ORNL hollow silica particle manufacturing process compared with the currently reported processes.

Item	Unit Price (USD)	Required Amount [a]		Cost (USD) [a]	
		ORNL	Reported [b] [54,55,56,57]	ORNL	Reported
Styrene	1.5/1.1 L	200 mL	200 mL	0.3	0.3
Catalyst	5/kg	5 g	5 g	0.03	0.03
Alcohol (ethanol/isopropanol)	0.9/L	300 mL	15 L	0.27	13.5
Ammonium hydroxide	0.50/L	25 mL	1.25 L	0.0125	0.625
Tetraethyl orthosilicate	1.9/L	100 mL	100 mL	0.20	0.19
Electricity	0.10/kWh	5 kWh	5 kWh	0.50 [d]	0.50
Total manufacturing cost [c]				1.31	15.14

[a] Values are based on a sample volume equivalent to 1 ft^2 × 1 cm, [b] Reported amounts of chemicals ae estimated by extrapolating the amounts of different chemicals to get 1 ft^2 × 1 cm from references [54,55,56,57], [c] Does not include labor, [d] Electricity consumption will be lower in ORNL strategy because of high initial yield, however we included similar costs for both manufacturing processes.

solution recycling strategy. Because the reported synthesis strategies provide a very small amount (≈3 cm3) of particles for 100 mL of alcohol, approximately 15 L of alcohol will be used for obtaining the same number of particles. By looking at the cost analysis table it is clear the costs of all other chemicals except the solvent are almost the same in both strategies, and the cost of the solvent is the main contributing factor in the final cost of hollow particles. Recycling the processing solution reduced the amount of solvent used during fabrication and, thus, lowers the manufacturing cost of hollow particles and making them economically feasible for immediate use in building envelopes. Section 2.2.1 will discuss the physical characteristics of these materials and their insulation capabilities.

2.2 **Hollow Silica Nanoparticle Characteristics**

2.2.1 Geometrical parameters

Hollow silica nanoparticles are highly tuneable NIMs that possess unique characteristics that derive from their geometrical properties. These properties are defined the inner core diameter of the hollow particle and the thickness of the shell.[53, 58] The physical parameters of the system constitute the solid contribution (k_{sol}) to the effective thermal conductivity of the system. A derivation and comprehensive study investigating these geometrical parameters was completed by Jia et al. to more accurately predict the effective thermal conductivity of these systems and the model is presented in Equation 5.[59]

$$\frac{k_p^{ITR}}{k_m} = \frac{3 + (\frac{k_c}{k_s} - 1)(1 + 2v)}{\frac{k_m}{k_s}[3 + \left(\frac{k_c}{k_s} - 1\right)(1 - v) + \alpha[3 + \left(\frac{k_c}{k_s} - 1\right)(1 + 2v)]} \quad (5)$$

Here k_p^{ITR} represents the thermal conductivity of the hollow particle that is in contact with adjacent particles and experiences interfacial thermal resistance, captured by the α term. Interfacial thermal resistance will be discussed in further detail in the following section. To evaluate the geometrical contribution the thermal conductivity, k_p^{ITR} was normalized by the thermal conductivity of the matrix k_m which under applicable conditions is likely to be same gas which fills the core and possesses the same thermal conductivity k_c (*i.e.*). The

$$v = \frac{r^3}{(r + t)^3} \quad (6)$$

thermal conductivity of the shell k_s is the final thermal parameter that is considered in this model and is a fixed value based on the thermal conductivity of the shell. In summary the

effective thermal conductivity of hollow particles systems is foundationally affected by the thermal properties of the shell material, gas filling the matrix and the gas filling the core. Although the thermal conductivity of the shell material is fixed, its contribution as the solid material contribution depends on its volume fraction compared to the gas in system. Additionally, the conductivity of the gas can be modified by the size of the practical systems geometrical features. The geometrical parameters capable of tuning the effects of the solid shell content and thermal conductivity of the gas is presented in Equation 6. Here v is a dimensionless ratio that relates the radius, r, of the particle and the shell thickness t. It is clear that the geometrical parameter plays a key role in modifying the effective thermal conductivity of the hollow silica nanoparticle system.[60] Explicitly the thermal conductivity of the shell material is fixed but its ratio to the gas content in the system is a function of the shell thickness and inner core diameter and determines the solid contribution to the thermal conductivity.[61] Therefore, this thesis experimentally demonstrates the effects of tuning these geometrical parameters in order to elicit optimal performance in these systems. Prior to synthesising hollow particles possessing different inner core diameters and shell thicknesses the effects of interfacial resistance and effective radiative thermal transport are discussed in the following sections.

2.2.2 Interfacial thermal resistance

Interfacial thermal resistance, also known as Kapitza resistance is characterized by a temperature discontinuity at the interface of two or more materials in physical contact with each other.[62, 63] This type of resistance occurs due to differences in the phonon and electronic transport properties.[64] In adjacent materials composed of the same or different structures are misoriented at the atomic scale energy carriers such as electrons or phonons

are scattering and have been found to be the source of significant heat loss in certain systems.[65] This thesis will not discuss the prominent acoustic or diffuse mismatch models that are currently used to understand this phenomenon, but instead will present an overview of its use in the current equivalent model and provide experimental data for use in evaluating comprehensive models.

In the current equivalent model previously discussed in the last section, Jia et al took the interfacial thermal resistance in consideration to account for the temperature discontinuity at the particle to particle interface.[59] In summary the equation which described this discontinuity is given by Equation 7,

$$k_{ITR} = \frac{k_c}{1 + \alpha k_c / k_m} \tag{7}$$

where the thermal conductivity of particles with interfacial thermal resistances k_{ITR} is defined by the thermal conductivity of the core, the thermal conductivity of the matrix and most importantly the α-parameter and is described in Equation 8.

$$\alpha = \frac{R_{Bd} k_m}{r} \tag{8}$$

This α-parameter is a function of the R_{Bd} that captures the heat transport through thin shells, the thermal conductivity of the matrix and the radius of the particle. It is important to note that as the particle radius decreases, the inner core diameter decreases thus increasing the Knudsen effect in these systems, which is reported to lower the thermal conductivity of the gas in the core.[66, 67] Additionally, as the radius decreases the alpha

term will increase and as result effective thermal conductivity of the particle experiencing interfacial thermal resistance decreases. This thesis considers the size contribution of the particles on the effective thermal conductivity by experimentally demonstrating and discussing the effect of interfacial thermal resistance on the effective thermal conductivity.

2.2.3 Radiative characteristics of silica insulation

Low density silica aerogels are highly transparent to electromagnetic radiation below 8 μm.[68] Although literature discusses characteristics of silica aerogels that are exposed to thermal radiation, studies done on hollow silica nanoparticle systems are limited. These materials have been shown to exhibit similar transparency to thermal radiation over a wide range of wavelengths.[69] To further improve the effective radiative insulating properties of these materials carbon fillers of various sizes are introduced into the hollow silica nanoparticle matrix to experimentally investigate effects on both the interfacial thermal resistance and the effective radiative contribution in the system. The size of the carbon black present in the system variably introduces additional thermal interfaces where temperature discontinuities may occur. Relative to the thermal radiative characteristics of these materials, Figure 6 shows an adapted graph of the transmittance of both carbon black additives and silica aerogels.[70, 71] It is clear from this image that the silica aerogel transmits a large present of both visible and infrared radiation while the carbon black is shown to transmit less than 10% of then that of the aerogel. By incorporating this same concept in the evaluation of our hollow silica nanoparticle systems, this thesis describes the use of carbon black opacifiers to limit the radiative transport in these systems and

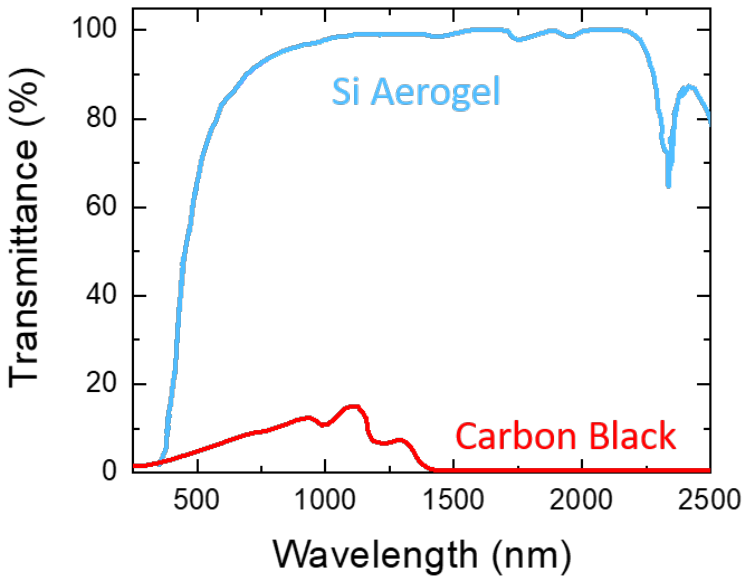

Figure 6 UV-Vis-near IR spectra transmittance spectra of silica aerogels and carbon black filler materials.

considers their effect to create additional interfaces where thermal resistance may occur.

2.3 Synthesis

A detailed synthesis is presented in this section to outline modified fabrication parameters for both the polymer sacrificial template and the Stober method. The adaptations from synthesis recipes are explicitly highlighted to provide the scientific community with a clear guild to reproducing the work that was completed.

2.3.1 Sacrificial polymer template

Hollow silica nanoparticles can be made using a number of templating such as micelles, inorganic particles, bacteria and viruses and polymer particles.[72] In this body of work polystyrene (PS) particles were used as a sacrificial polymer templates and were

synthesized by modifying the reported method by Nandiyant. [53] In this modified synthesis 250 mL of water was heated at 70 °C for 1 hour in a 500 m: round bottom flask. Next 25 mL of styrene was added to the heated water and stirred at 600 rpm for 10 minutes before adding 2 mL of 160 mg per 1 mL of 2,20 -Azobis(2-methylpropionamidine) dihydrochloride (AIBA). After stirring for 12 hours, synthesized particles are dried using a VWR convection oven. Figure 7 shows the photographic image of dried polystyrene particles and SEM image of individual nanoparticles forming monolithic colloidal structures. These structures can be dismantled by grinding the flakes using mechanical force to produce a fine white powder consisting of individual or small clusters of the polymer template. Loose packed hollow silica nanoparticles are needed to enhance the effects of interfacial thermal resistance. Therefor the sacrificial polymer particles used in this study are grinded mechanically then sonicated in the processing fluid used to create

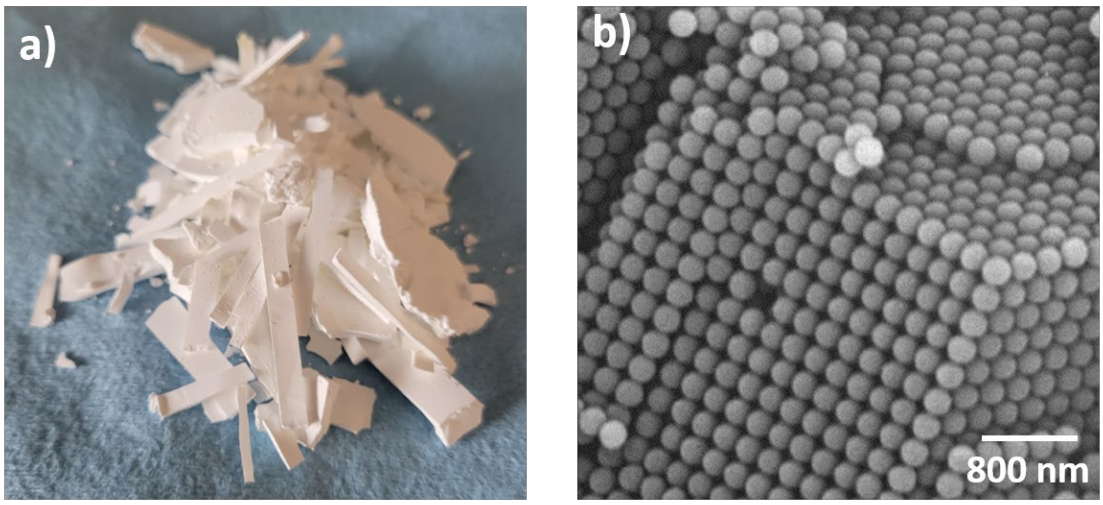

Figure 7 Photographic image of polystyrene monolithic slabs after the fabrication process. b) Scanning electron image of monodispersed polystyrene particles that make up the slaps.

the silica shell. A detailed description of the shell synthesis and removal is given in the following section.

2.3.2 Stöber method

The hollow silica nanoparticles being analysed for use as super-insulating thermal management materials are fabricated using the Stöber method to deposit uniform solid silica nanoparticles on sacrificial polystyrene templates as outlined in Figure 8.[73] Specifically, hollow silica nanoparticles were made by adding 5.0 g of PS particles into a solution consisting of 100 mL isopropanol, 30 mL of water, and ammonium hydroxide (28–30% to make solution pH ≈ 11). The reaction mixture was sonicated for an hour then stirred for 10 minutes. Next 4.5 mL of tetraethyl orthosilicate (TEOS) was added in 4 aliquots of 1.5 mL separated by 4-hour intervals. Note to increase the thickness of the shell more TEOS can be added to the solution. The silica coated polystyrene particles were removed from the supernatant by decanting and then dried in the convention oven for 2

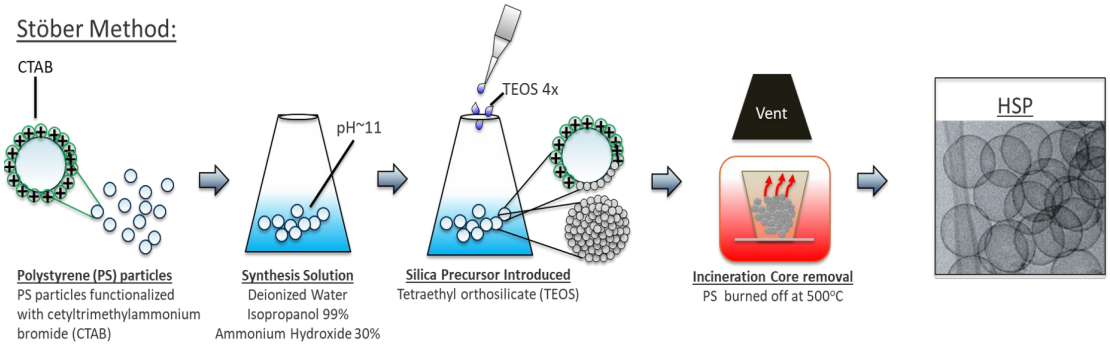

Figure 8 Stöber method diagram of monodispersed polystyrene particles processed with cetyltrimethylammonium bromide placed in the reaction solution containing water and isopropanol. The pH of the solution set to approximately 11 with the use of ammonium hydroxide. Tetraethyl orthosilicate is added and forms silica shells on the polystyrene particles. High temperatures remove the polymer core resulting in hollow particle formation.

hours. The silica coated PS particle are poured into an alumina crucible and place inside an MTI KSL-1100x furnace at 650 °C for four hours to burn off and remove the polystyrene core. After the furnace reached room temperature the pure hollow silica particles were collected and characterized using electron microscopy. The optical characterization of the nanoparticles is essential for verifying the particles inner core diameter and shell thicknesses.

2.4 Instruments and Experimental

2.4.1 Microscopy techniques

Several microscopy techniques were used to characterize the geometrical properties of the HNSP used in our experimental investigation. A Hitachi SU8230 Scanning electron microscope (SEM) available in the Shared User Management System facility at Georgia Institute of Technology was used for this characterization. Polystyrene particle and hollow silica nanoparticles were dispersed in isopropanol and placed on silicon wafer purchased from University Wafers then attached to the SEM mounting stubs. Transmission electron microscope (TEM) imaging was also performed using a Hitachi HF3300 TEM/STEM (Hitachi Global, Chiyoda, Tokyo, Japan). Figure 9 shows SEM and TEM images taken on hollow silica nanoparticles. Samples were prepared by placing a small number of dried particles in a via filled with ethanol then dropping solution containing hollow particles on

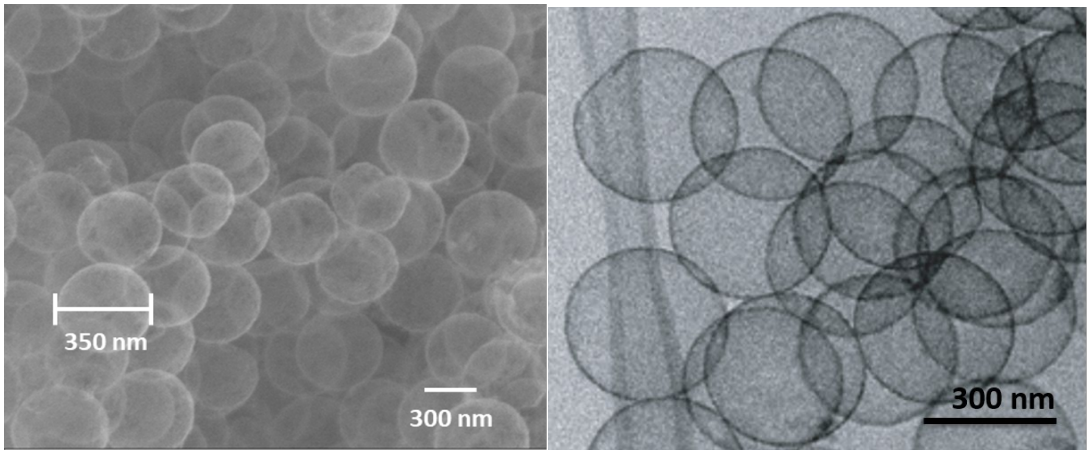

Figure 9 Scanning electron microscope images of used to identify uniformity of hollow particle clusters. b) Transmission electron microscope image used to verify shell thickness

lacey carbon coated copper TEM grids. These microscopy techniques were utilized to measure the geometrical parameters of the hollow silica nanoparticles systems.

2.4.2 Thermal measurements

Thermal conductivity measurements were performed using a transient plane source and modified transient plane source instrument from C-Therm. Figure 10 shows the physical sensor and sample placement convention for both methods. These methods utilize an integrated sensor and electrically conducting heat source elements in the shape of a bifilar spiral.[74] This allows the sensor material to simultaneously increase the temperature of the sample and also serves as a resistance temperature probe capable of measuring the temperature increase of the sample over time. This recorded change in the samples temperature over time is them used to calculate the thermal conductivity and thermal diffusivity of the sample.[74] Although the two techniques utilize the similar principles the transient plane source technique requires two samples of the same material

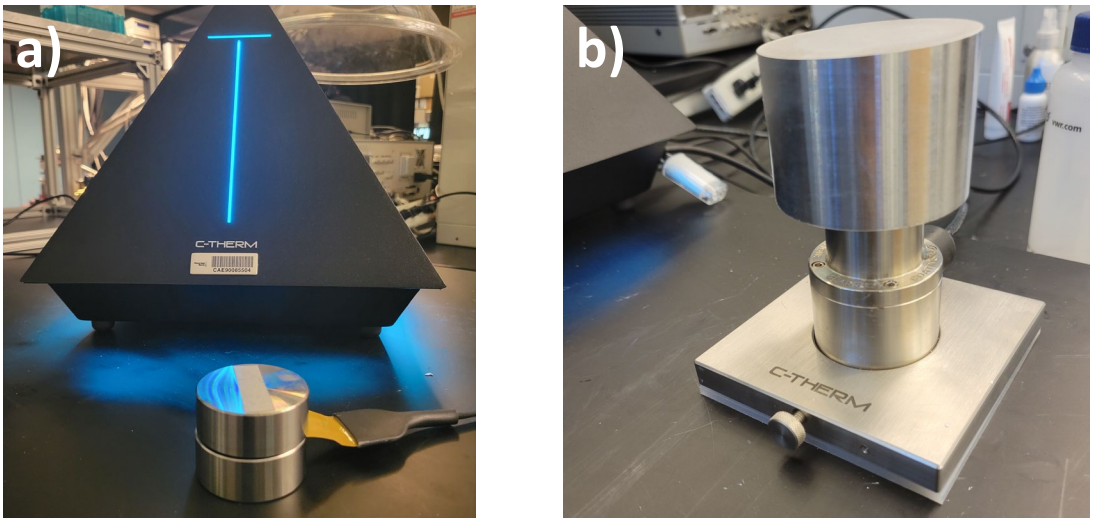

Figure 10 Transient plane source and modified transient plane source thermal conductivity device being calibrated with steel and aluminum blocks respectively.

and geometrical shape to create a smooth contact with the flat sensor on both sides, while the modified version of this technique only requires single samples. The modified transient plane source instrument came equipped with a manufacturer provided powder sample holder and was primarily used to characterize the various particle systems. All thermal conductivity measurements were performed on loose packed particles using the insulation measurement pre-setting on the tool.

2.5 Results

2.5.1 Inner core diameter and effective thermal conductivity

The effects of the inner core diameter and shell thickness of hollow silica nanoparticles have been identified as the key geometrical parameters that influence the effective thermal conductivity of these systems. Explicitly, as the inner particle diameters

of the hollow silica nanoparticles increases the volume fraction of the solid material decreases, however, increasing the size of inner particle diameters in nanosized cavities will inherently decrease the Knudsen number and thus increase the thermal conductivity of the gas in the system to that of its free volume value.[59] Figure 11 shows the effective thermal conductivity of hollow silica nanoparticles with fixed shell thickness (approximately 10nm ± 3nm) and various inner core diameters. Note this graph depicts the nonlinear relationship between the inner core diameter and the effective thermal conductivity of the system. It is obvious that hollow silica nanoparticles with 250 nm and 425 nm inner core diameters were consistently measured to have higher effective thermal conductivity than particles with inner core diameters of 350 nm. This effect can be explained by considering the specific contributions to the effective thermal conductivity in these systems. hollow silica nanoparticles systems with 250 nm inner particle core

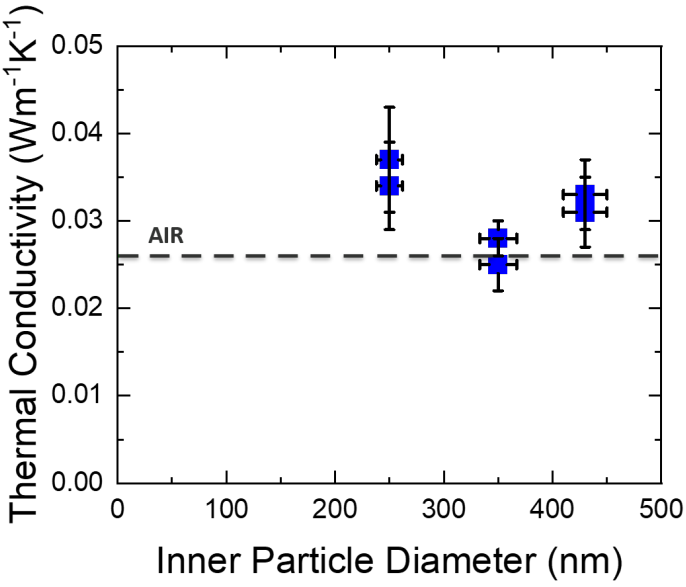

Figure 11 Effective thermal conductivity values of hollow silica nanoparticles with fixed shell thicknesses of approximately 10nm and inner core particle diameters of 250, 350, and 425 nm.

diameters contain 12.2% solid material and 87.8% gas. They were measured to have an effective thermal conductivity of 0.035 +/-0.005 $Wm^{-1}K^{-1}$ which is on par with current conventional materials.[75] The thermal conductivity of the silica shell is assumed to be fixed at a value of 1 $Wm^{-1}K^{-1}$ and its solid state contribution is directly linked to its volume fraction in the composite. Larger volume fraction of solid content will significantly impact the effective thermal conductivity system because its thermal conductivity is two orders of magnitude higher than of the free volume of the gas. The thermal conductivity of the gas is believed to be reduced by up to 20% due to nanoscale confinement previously discussed in section 1.1.3.[42] In contrast, hollow silica nanoparticles systems containing nanoparticles with larger 425 nm inner core diameters are comprised of 6.8% solid material and 93.2% gas. These systems were measured to have a slightly lower thermal conductivity of 0.032 +/-0.003 $Wm^{-1}K^{-1}$. This small decrease indicates that the gas filling the matrix dominates the effective thermal conductivity as the solid material is reduced from increasing the inner pore diameter.[76] Although systems made with 425 nm cores contain the least amount of solid material, increasing the inner pore diameter also increases the thermal conductivity of the gas by reducing the Knudsen effect. The thermal conductivity of the gaseous state in particles of this size is believed to only be reduced by 5%. hollow silica nanoparticles systems containing materials with 350 nm cores were measured to have the lowest thermal conductivity. At a value of 0.025 +/- 0.003 $Wm^{-1}K^{-1}$ these particles exhibit the beneficial tradeoff between maintaining a low solid to gas ratio while still maintaining a reduced gaseous thermal conductivity from the Knudsen effect. Explicitly, the volume fraction of solid in these systems is 8.8% which leaves the volume fraction of the gas at 91.2% and the thermal conductivity of the gas is believed to be reduced by 12%.

The optimum performance of particles with inner core diameters of 350 nm informed there used in evaluating the effective thermal conductivity of hollow silica nanoparticles with various shell thickness and is presented in the following section.

2.5.2 Shell thickness and effective thermal conductivity

Increasing the shell thickness is hypothesized to directly add to the amount of solid content and raise the effective thermal conductivity of the system.[61] It is known that super-insulation materials rely on leveraging minimal amounts of solid content while simultaneously maintaining nanoscale features in order to take advantage of reductions in the gaseous thermal conductivity caused by nanoscale confinement.[42, 46, 77] Figure 12 shows the effects of increasing the shell thickness of hollow silica nanoparticles with 350 nm inner core diameters. Interestingly TEOS concentrations used to achieve shells thicknesses below 6 nm resulted both the formation hollow silica nanoparticles systems with thermal conductivities ranging between 0.024 $Wm^{-1}K^{-1}$ and 0.043 $Wm^{-1}K^{-1}$. The large variation in the measured thermal conductivity values in these systems is largely due to batch specific formations of highly porous and incomplete shells. The presents of fragmented shells raise the effective thermal conductivity of the hollow silica nanoparticles insulation by increasing the loose packed particle density and by forming conductive

pathways larger than the mean-free-path of the gas entrapped in the particle and surrounding matrix.[67] As expected, increasing the shell thickness also increases the effective thermal conductivity of the system by increasing the volume fraction of solid material relative to the gas entrapped in the system. As discussed in the previous sections the thermal conductivity of the silica is two orders of magnitude larger than the gas entrapped in the matrix.[78] hollow silica nanoparticles with 350 nm cores with 15 nm and 25 nm shells have thermal conductivity values as low as 0.028 $Wm^{-1}K^{-1}$ and 0.033 $Wm^{-1}K^{-1}$, respectively. These values are similar to conventional glass wool and polymer-based building insulation materials.[79] To minimize the adverse effects of having incomplete shells or shells with excess thickness, the TEOS concentration in the synthesis solution was fixed to produce complete shells ranging between 8 to 10 nm. As seen in the previous

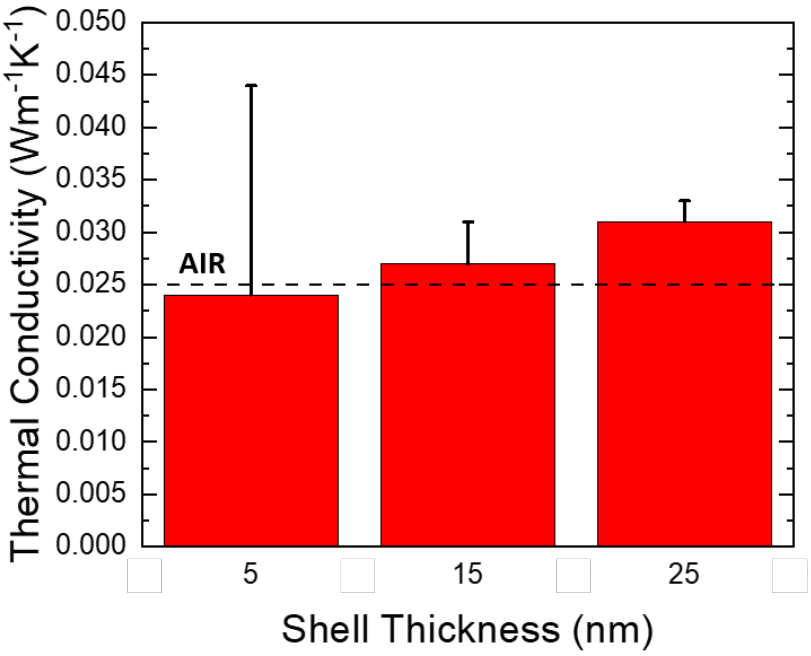

Figure 12 Shell thickness variations of hollow silica nanoparticles with 350 nm inner core diameters on the effective thermal conductivity of the material.

section hollow silica nanoparticles systems with 350 nm cores and shell thicknesses near 10 nm have thermal conductivity values that are equivalent to ambient air. Therefore, fixing the core size and shell thickness in this range produced complete shells with minimized the solid contribution to the effective thermal conductivity of the hollow silica nanoparticles systems.

2.5.3 Carbon black additives

Carbon black has a much higher absorption coefficient than silica over the visible and infrared regimes. Doping carbon in silica aerogel has been shown to significantly reduce radiative transport through the structure.[30] Additionally, incorporating carbon black into the physical structure of the aerogel was reported to appreciably strengthen the material.[80] These advantages are translated to hollow silica nanoparticle composites in order to reduce its transparency to thermal radiation. However, replacing an air-filled matrix with solid material has drawbacks. Although the presence of carbon black further limits space in between particles, which in turn further reduces the gasses thermal conductivity through the Knudsen effect, it also increases the thermal conductivity after a specific volume fraction is reached. It is important to mention carbon black has thermal conductivity (0.3 Wm^{-1} K^{-1}) an order of magnitude higher than air (0.026 Wm^{-1} K^{-1}).[81] As a result, determining the percentage carbon black loading into the composite matrix is crucial in designing optimized ternary composites.

2.5.4 Size effect of carbon black additives

Low density silica structures including hollow silica nanoparticles are highly transparent to a broadband of thermal radiation.[82, 83] To further improve the insulating

properties of these materials carbon fillers of various sizes were introduced into the hollow silica nanoparticles matrix to experimentally investigate effects from interfacial thermal resistance and the effective radiative contribution in the systems effective thermal conductivity. The size of the carbon black present in the system is responsible for introducing thermal interfaces where temperature discontinuities occur at each interface. Figure 13a shows 4 μm carbon black particles surrounding hollow silica nanoparticles clusters with 350 nm cores. These large carbon black particles are unable to fit in between the interstitial sites between the nanosized hollow particles. Instead, large carbon black particles agglomerated and formed thermally conductive networks within the hollow silica nanoparticles systems. Agglomerated clusters of carbon black 100 μm in length were present in these hollow silica nanoparticles composite systems. As result the smaller hollow particles surround carbon black clusters and fill larger interstitial void space in between the filler material. In contrast, Figure 13b shows carbon black particles 10 nm in length surrounding individual hollow silica nanoparticles with the same 350 nm inner core

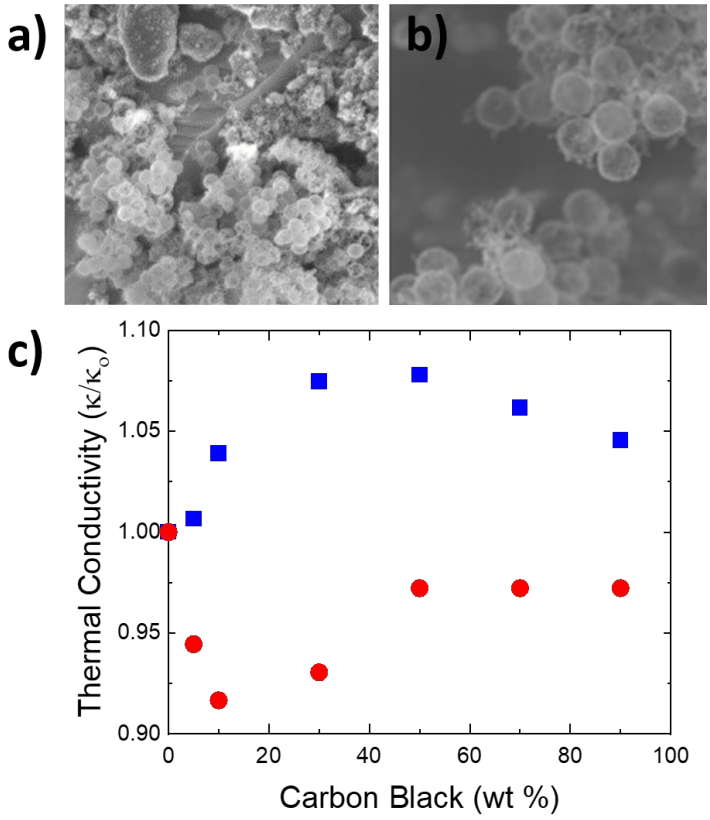

Figure 13 Carbon Black additives images and normalized thermal conductivity in a hollow silica nanoparticles system. a) Large carbon black clusters present in the microstructure of the hollow silica nanoparticles system. b) Nano sized Caron black clusters shown surrounding individual hollow silica particles. c) Normalized thermal conductivity of the hollow silica nanoparticles systems evaluated with two sized of carbon black particles.

diameter. These smaller carbon black particles can surround and fitting into interstitial sites in between individual hollow silica nanoparticles as seen in the SEM. Similar weight percent of both carbon black particles were added to the hollow silica nanoparticles systems to investigate their effect on the effective thermal conductivity of ternary systems. Figure 13c shows the normalized thermal conductivity of hollow silica nanoparticles with 350 nm shells as microscale carbon black particles (blue squares) and nanoscale carbon black particles (red circles) were incorporated into the system at different weight percent. An

immediate rise in the thermal conductivity is observed in hollow silica nanoparticles systems that contain the larger carbon black clusters until the weight percent of the carbon black in the system reaches 50%. After this benchmark a drop in the normalized thermal conductivity is observed and is credited to the increase in interfaces between the dissimilar materials leading to larger interfacial thermal resistance. Interestingly, the normalized thermal conductivity in the same hollow silica nanoparticles system decreases immediately as nanosized carbon black additives are introduced into the system. The effective thermal conductivity in these systems reached its minimum value at 10 weight percent loading before increasing. Although an increase in the effective thermal conductivity of the hollow silica nanoparticles systems with nanosized carbon black particles with weight fraction between 30% and 50% was observed a similar reduction in the thermal properties of the system were observed after this point as seen in the systems with larger carbon black fillers. This decrease is less pronounced than the decrease seen in hollow silica nanoparticle-carbon black ternary composites containing the larger filler materials. This is believed to result from the ability the smaller particles packing more densely into the matrix. The packing density of carbon black fillers will be discussed later in section *2.5.6*.

2.5.5 Shell size and carbon black additives

The effect of nanosized carbon black particles on the effective thermal conductivity in a hollow silica nanoparticles- carbon black ternary composite was further investigated by putting them in systems with different shell thicknesses. We previously observed that increasing the shell thickness increases the effective thermal conductivity of the system. However, there remains a need to investigate if nanosized carbon black reduces the thermal conductivity of systems with different geometrical features. Figure 14 shows the effective

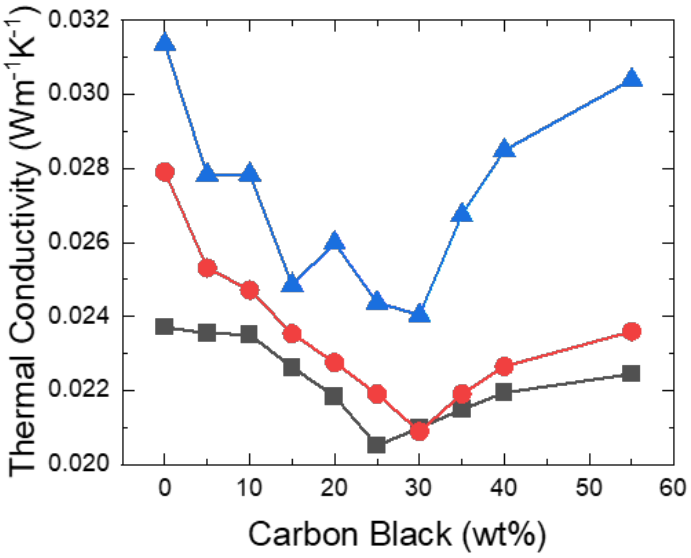

Figure 14 Carbon black added to hollow silica nanoparticles systems with 5nm (black), 15 nm(red) and 25 nm(blue) shells and350 nm inner core diameters. with different shell sizes. The blue curve represents hollow silica nanoparticles with 350 nm.

thermal conductivity of hollow silica nanoparticles with 5 nm, 15 nm, and 25 nm shells as a function of nanosized carbon black loading. The hollow particles in this figure have 350 nm inner particle cores as they have the best insulative properties. The thermal conductivity of hollow silica nanoparticles systems with 25 nm shells has the highest initial thermal conductivity followed by particles possessing 15 nm and 5 nm shells, respectively. Upon incorporating carbon black nanoparticles an immediately decreases the effective thermal conductivity in all hollow silica nanoparticles systems was observed irrespective of the shell thickness. In general, the conductivities values decreased until the weight fraction of the in each system reached 25-30 wt %. Small amounts of carbon black are able to change the transparency of the hollow silica nanoparticles system to thermal radiation significantly.[84] This change can be observed qualitatively through the darkening of the mixture corresponding to visible light absorption but is also hypothesized to be coupled

with dampening infrared transport through the system. Further studies are needed to access the radiative transport characteristics in these films.

The thermal conductivity in each system begins to increase after the carbon black added to the hollow silica nanoparticles systems exceeded 25-30 wt%. As previously mentioned, carbon black nanoparticles have a much higher thermal conductivity than the gas filling the matrix, and this leads to an increase in the effective thermal conductivity. Notice that the slope of this increase is steeper as the shell thickness is increased. This difference in slope is attributed to the nonlinear solid content contribution to the ECT. Specifically, the ratio of solid material scales exponentially as a function of shell thickness and the surface area decreases in particles with larger shells. This reduction in surface area coupled with the increased solid content explains the difference in slopes upon carbon black loading past 30%. This further confirms that the presence of nanosized carbon black can decrease the effective thermal conductivities in all systems.

2.5.6 Carbon black packing density

It has been demonstrated that nanosized carbon black particles can be used to lower the effective thermal conductivity in hollow silica nanoparticles systems. This reduction is believed to result from impeding the radiative heat flowing through the system and through the creation of thermal interfaces where heat can be scattered in a phenomenon known as Kapitza resistance. In this section, the effect of nanoscale contact contributions to the effective thermal conductivity of the system will be investigated and the role of carbon black packing in the system will be demonstrated. It was hypothesized that several factors, such as a change in the air volume of the sample and increased contact points, play an

important in determining the effective thermal conductivity in hollow silica nanoparticles systems. Figure 15 show photographic density results of mechanical mixing and acoustic mixing identical quantities of hollow silica nanoparticles with 350 nm cores and carbon black. Specifically, the experiment consisted of combining a known volume (0.16 cm^3) of carbon black to a known volume (0.8 cm^3) of hollow particles in a plastic sample holder then mixing to form a blended composite using an electronic lab mixer. The combined volume (1.2 cm^3) of carbon black and hollow particles was more than the sum of their individual volumes (0.96 cm^3). Therefore, it was clear that an increase in the total air volume of the system contributed to lowering the thermal conductivity of a hollow silica particle and carbon black mixture. It appeared that the increase in total volume resulted

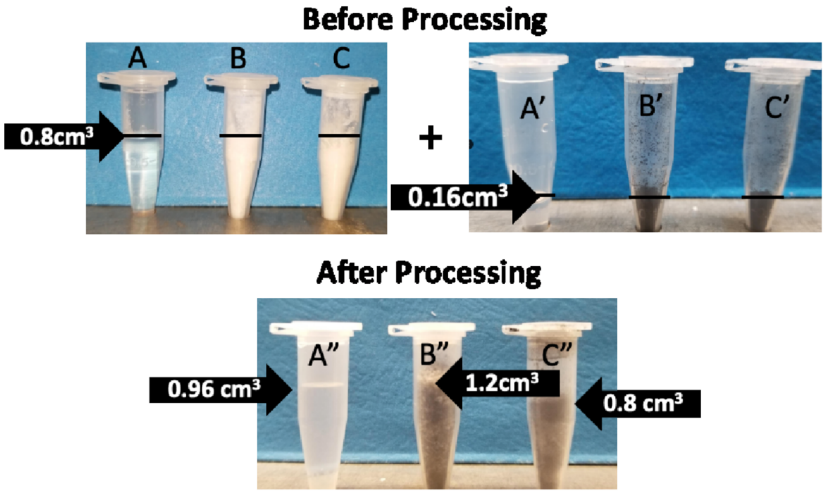

Where:
A: Water = 0.8 cm^3 + *A': water = 0.16 cm^3*
B: Hollow particles = 0.8 cm^3 + *B': CB = 0.16 cm^3*
C: Hollow particles = 0.8 cm^3 + *C': CB = 0.16 cm^3*
After mixing (processing):
A" : water = 0.96 cm^3 (A, A', & A" water samples are given only for volume comparison purposes)
B" : hollow particle + CB = 1.2 cm^3 (mechanically mixed by shaking with hand)
C" : hollow particle + CB = 0.8 cm^3 (mixed by sonicating in water bath for 1-2 min)

Figure 15 Digital photographs of different samples (hollow particles and carbon black) used in the carbon black effect on hollow particle thermal conductivity studies. Additionally, amounts of different samples are given in the lower part of the figure.

from the intercalation of carbon black nanoparticles between hollow particles and, thus resulted the increased spacing between the hollow particles. Before discussing the results from samples that were mixed using the sonication method it is worth mentioning that hollow or porous materials achieve low thermal conductivity by maintaining large volume fractions of entrapped air inside their nanocavities or pores.[85] Therefore, any increase in air volume has been shown to generally results in a corresponding decrease in the thermal conductivity of a material.[59] To study this packing phenomena thoroughly, hollow silica nanoparticles- carbon black mixtures are combined in the same quantity in an identical sample container. This container was filled with isopropanol to improve particle mobility and encourage particle ordering. The mixture was sonicated for 10 minutes then centrifuged for 10 minutes at 1000 rpm. Next the solvent was allowed to evaporate at room temperate for 24 hours before the sample holder was placed in a furnace at 30 °C. The sonicated insulation mixture was reflowed into an identical sample holder and had a volume of 0.8 cm^3, which was the original volume of the hollow silica nanoparticles prior to the addition of carbon black. This densification of the hollow silica nanoparticles- carbon black system is believed to result from the smaller carbon black packing in between and around individual silica nanoparticles and small clusters.

2.5.7 Carbon black packing and effective thermal conductivity

In aerogels, the lowest reported thermal conductivity was obtained by adding a small amount (≈10 wt%) of carbon black, whereas in hollow particles, the lowest thermal conductivity was achieved at quite a high amount (20 wt%) of carbon black. The variances result from the differences in the microstructures with aerogels being monolithic materials consisting of 2–5 nm nanopores and hollow particles being particulates with larger inner

pores and interstitial cavities. Radiative absorption plays the main role in reducing the thermal conductivity of aerogels, whereas in hollow silica nanoparticle systems, radiative absorption, increased air volume, and contact resistance between the carbon black fillers have all been demonstrated to aid in lowering the effective thermal conductivity of carbon black-hollow silica nanoparticle systems.

To understand how carbon black dispersion affects the thermal conductivity of a carbon black –hollow particle mixture, transient plane source measurements were conducted. This technique required larger batches of pure hollow silica nanoparticles, mechanically mixed and sonicated hollow silica nanoparticles- carbon black samples to be placed on both sides of the TPS sensor as described earlier in this chapter. Figure 16 bar chart shows the effect of the carbon black dispersion method on the thermal conductivity of hollow particle carbon black sample. Notice that the carbon black lowers the effective thermal conductivity in both dispersions. Interesting the denser sonicated mixtures thermal conductivity values were consistently measured to by 19.5 $Wm^{-1}K^{-1}$, lower than the 20.5 $Wm^{-1}\cdot K^{-1}$ conductivity mixtures that were dispersed by mechanical mixing. Descriptive SEM images of the hollow particles alone, mechanically mixed samples, samples mixed by sonication are presented as insets i–iii of Figure 16. Colloidal crystal formations are commonly observed in the pure hollow silica nanoparticles microstructure and thus they have a larger packing factor. In contrast the SEM image representing mechanically mixed samples show large domains of white and black areas corresponding to chunks of carbon black with the smaller hollow silica nanoparticles around them. Mixtures prepared through sonication appeared to be completely dark suggesting that the carbon black was well

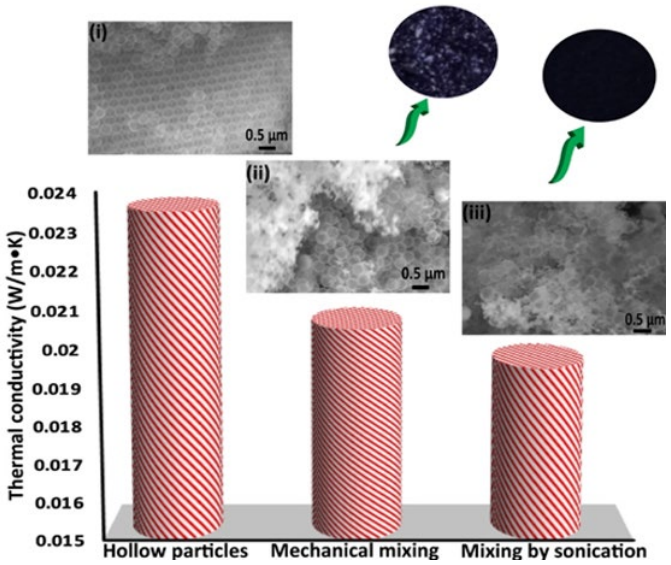

Figure 16 A plot showing the effect of carbon black dispersion on the thermal conductivity of a hollow particle–carbon black mixture. Insets (i), (ii), and (iii) are SEM images of hollow particles alone, a mechanically mixed hollow particle–carbon black mixture, and an ultrasonically mixed hollow particle– carbon black mixture, respectively. Sub-insets: Photos of mechanically and ultrasonically mixed carbon black and hollow particles.

dispersed throughout the hollow silica nanoparticles matrix. The SEM images seen in the third inset confirmed the hypothesis as carbon black clusters can be seen in the interstitial sites of the hollow silica nanoparticles matrix. This qualitatively confirms that the better performing sonicated mixtures were denser than mechanically mixed samples.

The lower thermal conductivity in these dense systems may be counterintuitive because a substantial volume fraction of gas residing in between particles is being displaced by solid filler material. Additionally, the thermal conductivity of the carbon black is one orders of magnitude larger than the gas and nearly 5 times lower than the solid silica shell. A reasonable explanation for this repeatable phenomenon is offered in the findings and core principles discussed in this chapter. Specifically, as carbon black nanoparticles settle between the hollow silica nanoparticles, they reduce the outer pore size. The reduction of

the outer pore size strengthens the Knudsen effect which reduced the thermal conductivity of the gas still trapped in the system even further. Additionally, the densification of the hollow silica nanoparticles- carbon black system created more contacts between the solid materials throughout the composite and these contacts are likely leading to an increase in interfacial thermal resistance.

2.6 Summary

In this chapter the optimal shell to pore size ratio needed to achieve the lowest effective thermal conductivity in hollow silica nanoparticles systems was identified and is consistent with the current equivalence model presented by Jia. et. al. Specifically, hollow silica nanoparticle systems with 350 nm cores have the lowest thermal conductivity in comparison to systems with 250 nm and 425 nm cores. This is explained by the two major competing effects associated with changing the inner particle diameter. As the core shrinks in size the Knudsen effect lowers the thermal conductivity of the gas, however, shrinking the size of the particle also increases the volume fraction of solid material which has a much higher thermal conductivity than the gas in the system. In the case of increasing the core of the hollow particle to 425 nm the silica shell accounted for only 6.6% of the system, however, the Knudsen effect is less pronounced, and the thermal conductivity of the gas rises towards the bulk value. As the core size for the hollow silica particles increases the gaseous contribution will begin to dominate the effective thermal conductivity. Systems with 350 nm cores achieved the lowest thermal conductivities by leveraging minimal solid content and by containing features small enough to leverage the Knudsen effect. Limiting the size of the shell was also shown to impact the effective thermal conductivity. Shells that are 5 nm or smaller are susceptible to breaking. Broken shell fragments can increase the effective thermal conductivity by increasing the density of silica inside the system. 15 nm and 25 nm shells create robust hollow particles and produce limited amounts of silica

debris. As expected, this increase in shell size also increases the thermal conductivity of the system. Therefore, hollow silica nanoparticles with 350 nm cores and shells ranging between 8-13 nm have been identified as optimal for insulation building applications.

The thermal conductivity in systems with optimized geometrical parameters was lowered even further by introducing carbon black into the matrix. Specifically, the degree in which these carbon black additions affected the thermal transport in hollow silica nanoparticles systems was identified. First an investigation which analyzed incorporating carbon black particles of different sizes was completed. Large polydisperse carbon black particles ranging from 4-100 μm in length formed thermally conductive pathways and the smaller hollow particles existed in clusters surrounding the opacifier material. These large particles raise the effective thermal conductivity once included into the hollow silica nanoparticle matrix, and are, therefore, not ideal for reducing thermal transport in these systems. In contrast carbon black nanoparticles averaging 10 nm in size immediately reduced the effective thermal conductivity of hollow silica nanoparticle systems. These carbon black nanoparticles surround individual hollow particles and hollow particle clusters. They also fit in interstitial sights and decrease the outer pore diameters. It was found that carbon black can reduce the effective thermal conductivity of a hollow silica nanoparticles systems by over 20% with just a 20 wt% addition into the matrix. After this point the thermal conductivity begins to increase with the addition of more carbon black. The lowest value achieved (0.019 $Wm^{-1}K^{-1}$) was in a system using optimal geometrical parameters that were previously discussed and 20 wt% carbon black nanoparticles.

CHAPTER 3. THEORY OF POLYMERIC PHOTONIC MIRRORS

3.1 Polymeric Dielectric Mirror Properties

Solar irradiance is modeled by a black body emitter operating at 5800 K, where 99% of the radiation intensity occurs over the ultra-violet, visible, and near infrared wavelengths.[86, 87] This thermal radiation can be transmitted through windows and add to heat loads in buildings that must be removed using space cooling.[88] Dielectric mirrors in the form of low emissivity windows, discussed in section 1.4, are in current use and offer a solution to reduce the amount of radiation transmitted into building spaces; however, they are fabricated using costly metallic or metal oxide thin films.[89] Dielectric mirrors made with polymers have generated considerable interest over translucent metallic mirrors because they exhibit lower optical losses over visible wavelengths and do not require energy intensive processing techniques such as sputtering.[90, 91] Although metallic mirror reflects over a wider bandwidth, enhancements to the optical constants can be made to increase the performance range of polymeric dielectric mirrors.[92] As seen in Figure 17 (b), dielectric mirrors leverage constructive interference conditions to reflect electromagnetic radiation as light propagates through high and low index bilayers in the dielectric stack. The resulting reflectance performance can be seen in Figure 17 (a) and is characterized by operational wavelength denoted by λ_0, the band edges which defines the reflected bandwidth and the intensity. It is also important to note that operational wavelength in these structures changes as a function of the incident angle of the beam propagating through the structure. This effect is captured in Equation 9, which give the constructive interference conditions to reflect an operational wavelength λ.

$$2n_2 2d\cos(\theta_2) = m\lambda \quad (9)$$

where n_2 and θ_2 are the refractive index and incident beam angle of the secondary medium the light first contacts respectively. Constructive interference will occur if the optical path difference is equal to an integer multiple m of the wavelength of radiation propagating through the secondary medium. Notice in Figure 17 (a) as the incident angle of the beam varies between normal incidence and 90° the operational wavelength and corresponding reflected bandwidth shortens and experience a blue shift. This thesis work utilized a normal incident angle in the design of polymer based dielectric mirrors made using quarter wave optical thicknesses conditions. Dielectric mirrors are typically designed using these quarter wave conditions, detailed in Figure 17, to achieve constructive interface. Theses governing principles that determine properties of reflective polymer thin film devices and the dynamic properties of the polymer constituents they are made off are presented in this chapter.

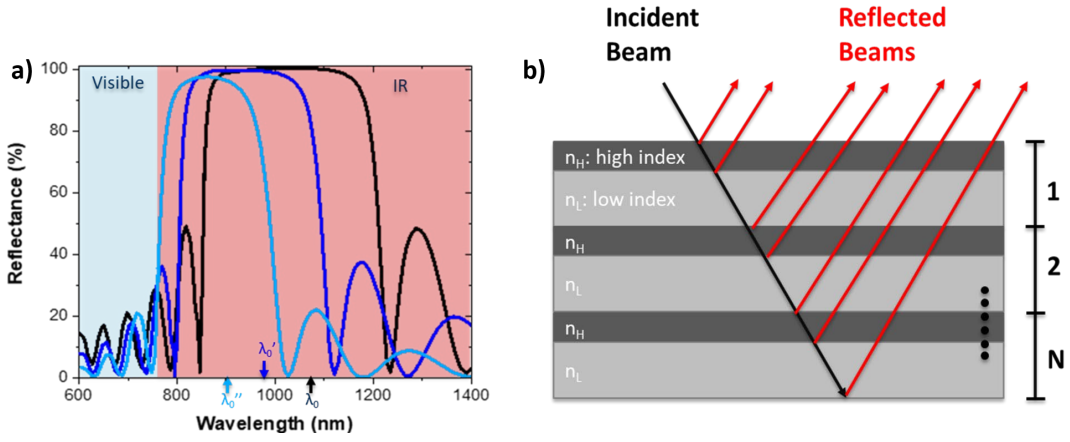

Figure 17 Illustrates the reflective properties of dielectric mirrors. (a) Incident beam of light of wavelength λ_0 propagating through a generic dielectric mirror stack with optical thicknesses that are integer multiples of its wavelength causing the beam to be reflected. (b) Modeled dielectric mirror with λ_0, λ_0', λ_0'', corresponding to decreasing the incident beam angle.

3.1.1 Quarter wave conditions

Controlled responses in polymeric DBR's can be understood by considering the rational design of the device for any application (including thermal management) and is governed by three equations. [93] Equation 2 establishes the operational wavelength, $\boldsymbol{\lambda_0}$ and is the central wavelength with the highest degree of reflection in the device.

$$\boldsymbol{\lambda_0 = 4(n_{L,H})d_{L,H}} \tag{10}$$

The quarter wavelength condition is a term that is derived by dividing the operational wavelength by four in the equation This leaves the optical constants of the material on one side of the equation. The quarter wave conditions also lead to the highest level of reflection; therefore, it is utilized to achieve maximum performance over a given spectral bandwidth. Figure 18 is an adapted illustrating constructive interference is achieved at λ_0 when the multiple of the refractive index ($n_{\mathrm{L,H}}$) and corresponding layer thickness ($d_{\mathrm{L,H}}$) of the low (L) and high (H) index material are tuned to both equal a fourth of the operational

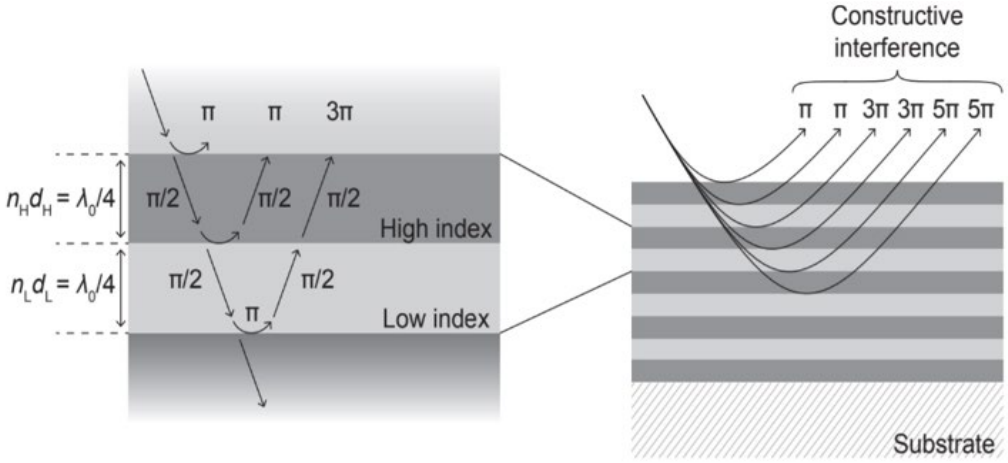

Figure 18 Quarter wave stack conditions used to produce integer multiples of the reflected operational wavelength. Illustration of constructive interference as the light propagates through the structure and its wavelength is shifted by 180º.[94]

wavelength.[94] First, the light enters the high index material and the portion of light experiences a 180° phase shift and is reflected, thus, the phase of the reflected wave at this interface is $\lambda_0 + \pi$. The transmitted light then propagated through the structure, which is set to be a quarter of the operational wavelength being reflected, resulting in a phase with a value of $\lambda_0 + {}^{\pi}/_{2}$ at the next boundary interface with the low index material. Again, part of this wave reflects through the body of the high index layer resulting in another ${}^{\pi}/_{2}$ addition to the initial λ_0. The wavelength exiting the structure is now at a value $\lambda_0 + \pi$ which results in the constructive interference of the reflected operational wavelength.[94] To ensure the quarter wavelength criteria is met Equation 10 was used to for both theoretical modeling and experimental fabrication parameter specification. Deviation from these conditions result in dampening and peak shifts of the reflective band.

3.1.2 Reflection magnitude

The percent of radiation reflected by the polymeric distributed Bragg reflectors is given in Equation 11.

$$\Gamma = \frac{1 - (\frac{n_H}{n_L})^{2N} \frac{n_H^2}{n_a n_b}}{1 + (\frac{n_H}{n_L}) \frac{n_H^2}{n_a n_b}} \tag{11}$$

Where N is the number of bilayers in the dielectric stack and n_a and n_b correspond to the refractive index of the mediums in the front and back of the film. It is evident that the total reflectance is a function of the magnitude contrast between the high and low index materials that make up the stack, however, increasing the number of bilayers N can also be used to achieve nearly 100% reflectance.

3.1.3 Reflection bandwidth

The reflection bandwidth, denoted by $\Delta\lambda$, is defined as the wave range in which clear band edges are observed. These band edges are on opposite sides of the operating wavelength λ_0 and are denoted as λ_1 and λ_2. The difference in the values of these band edges that make up the total reflected bandwidth are given in Equation 13**.**

$$\Delta\lambda = \lambda_1 - \lambda_2 \tag{12}$$

$$\lambda_1 = \frac{\pi(n_H d_H + n_L d_L)}{acos(\tau)}, \lambda_2 = \frac{\pi(n_H d_H + n_L d_L)}{acos(\tau)} \tag{13}$$

$$\tau = \frac{n_H - n_L}{n_H + n_L} \tag{14}$$

Like the reflection magnitude in these structures, the total bandwidth of the reflected wave range is strongly related to the refractive index magnitude contrast between the high and low index layers.

Dielectric mirrors that were evaluated in this thesis were fabricated using transparent polymers with relatively low refractive index contrasts. Increasing the refractive index of the high index layer is essential to both decreasing the number of layers needed for maximum reflection but also to increase the reflected bandwidth of the mirror.

3.2 Polymer Swelling Theory

3.2.1 Swelling in polymer systems

Another advantage of using polymers to fabricate dielectric mirrors is that their physical structures can be changed post processing to alter the optical thicknesses which modulates the mirror's degree of reflection.This is possible because polymers are "soft materials" with a low elastic modulus and free volume, and polymers have a variety of chemistries.[95] This combination of properties enables polymers to be dynamically responsive to external chemical or physical stimuli (*e.g.* solvent vapours, heat, light).[96] Therefore, as a function of the bilayer chemistries and stimuli, polymeric distributed Bragg reflectors can be deployed with dynamically responsive conductive and photonic properties.[97]

This thesis work leveraged the phenomenon known as polymer swelling to change the thickness of the hydrophilic DBR layers. Figure 19 illustrates the polymer swelling process and is characterized by the penetration of solvent molecules into a polymer matrix causes an immediate increase in volume microstructure.[98] Specifically, the distributed Bragg reflectors used to complete this research were made of hydrophobic polymethylmethacrylate and a hydrophilic polyvinyl alcohol. Water vapor was used as the

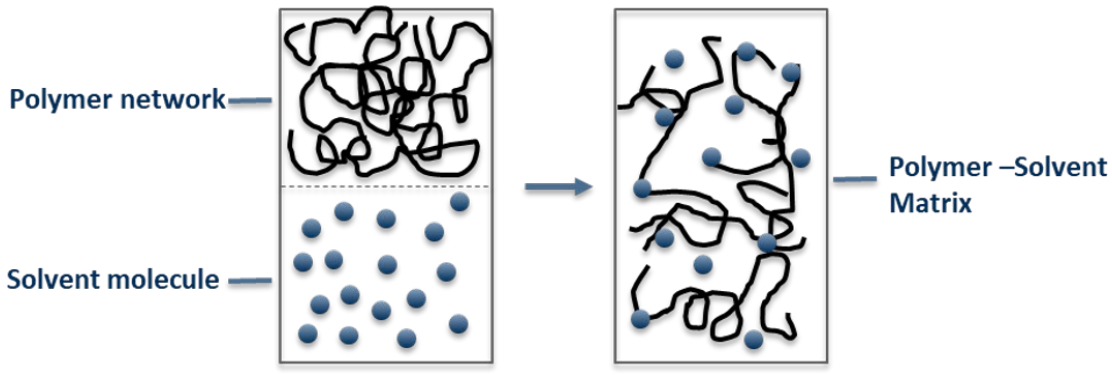

Figure 19 Diagram of polymer network and water molecules combining to form a polymer solvent matrix.

solvent to induce swelling, therefore the polymethylmethacrylate layer is assumed not to swell during this process.

3.2.2 Flory-Rehner equation

The swelling characteristic in polymers is theorized to be a controllable thermodynamic process. The degree of swelling was first proposed in the Flory-Rehner theory of polymer swelling. This theory is given by Equation 15 and16 and detail the competing thermodynamic parameters which govern the equilibrium of solvent uptake.[99]

$$\Delta G = \Delta G_{mixing} + \Delta G_{elastic} \tag{15}$$

$$-[\ln(1 - v_2) + v_2 + \chi_1 v_2^2] = \frac{V_1}{\overline{v}M_c}(1 - \frac{2M_c}{M})(v_2^{\frac{1}{3}} - \frac{v_2}{2}) \tag{16}$$

Based on this theory, swelling occurs until the free energy associated with the solvent mixing with the polymer (ΔG_{mixing}), seen on the left side of Equation 16, is in equilibrium with the free energy of the elastic forces ($\Delta G_{elastic}$) felt by the polymer as it expands to incorporate additional solvent molecules. The specific parameters that govern the degree of polymer swelling are the volume fraction of polymer in the swollen state v_2, the Flory solvent polymer interaction term X_1, the molar volume of the solvent V_1, the molar mass of the polymer M and the average mass between crosslinks M_c.[100] The chi factor and volume of the solvent molecule in the equation can be found in literature while the molar mass of the polymer can be determined through common Size Exclusion Chromatography measurements. This leaves the average molecular mass between crosslinks (*i.e.*, the crosslink density) and volume fraction of the swollen polymer. There is no direct way of

measuring the crosslink density, but it can be estimated by experimentally determining the associated swelling ratio to elicit the volume fraction in the swollen state.

Determining the swelling ratio to elicit the volume fraction of the swollen polymer was done using non-destructive optical measurements. Physical means of measuring thickness of the thin film such as profilometry could not be used because the films immediately began shrink and equilibrate with the environment after being removed from the humidified test chamber. Explicitly the sample thickness was measured in-situ and used a proxy to calculate the change in volume.

3.3 Transmissivity and Reflectivity Modeling

3.3.1 Swanepoel method

Extracting the thickness of a dynamically changing polymer networks was a critical aspect of this thesis. To resolve this problem, a combination of the Swanepoel method and transfer matrix method modeling were employed and their results were compared. As the concentration of the solvent molecules changes as a function of relative humidity, the film thickness was hypothesized to increase resulting in the alteration of interference fringes seen in the transmittance data. Figure 20 shows the UV-Vis-NIR transmittance spectra of chalcogenide thin films and the fringes that form from the material light interaction.[101]

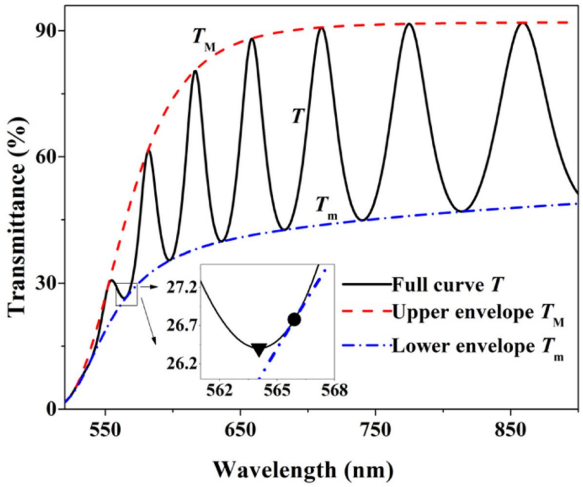

Figure 20 Fitted data using Swanepoel first method approximations. Values being fit are unfixed and allowed to be fit and adjusted. This process is iterated as all the Cauchy parameters are fit and adjusted. [105]

The Swanepoel method analyzes the size and location of these interference fringe peaks to derive the wavelength dependent refractive index. Specifically, this method works by using least squared regressions to create data envelopes comprised of the maximum transmittance curve (T_{max}) and the minimum transmittance curve T_{min} to compute optical constants of a film. Calculating approximations of the film's optical constants in the mid-weak "absorbance" regimes then becomes possible by using the equations below,

$$n(\lambda) = [M + (M^2 - s^2)]^{\frac{1}{2}}]^{\frac{1}{2}} \tag{17}$$

$$M = \frac{2s(T_{max}(\lambda) - T_{min}(\lambda))}{T_{max}(\lambda)T_{min}(\lambda)} - \frac{s^2 + 1}{2} \tag{18}$$

$$d_f = \frac{(\lambda_1)(\lambda_2)}{2(\lambda_1 n(\lambda_2)) - \lambda_2 n(\lambda_1)} \tag{19}$$

where n is the wavelength dependent value of the complex refractive index, s is the refractive index of the glass and d_f is the film thickness.

3.3.2 Transfer matrix method

Although, the Swanepoel method yields good first approximations, it is highly sensitive to non-ideal spectral data that is commonly present in experimental data due to poor sample quality and equipment error. For better accuracy and a higher degree of confidence in the derived film thickness and refractive index, the experimental data is fit to a custom transfer matrix method model developed by Alex Balzer using MATLAB. The right side of Figure 21 show the experimental UV-Vis-NIR data of a poly vinyl alcohol film that had been crosslinked with 30% titanium tetrachloride in a hydrate form and deposited on a sapphire substrate. Notice in the figure on the left that the interference fringes increase in both magnitude and in frequency as the film is humidified from 55% to 95% relative humidity and both oscillations are in good contact with the substrate. This suggest that there is

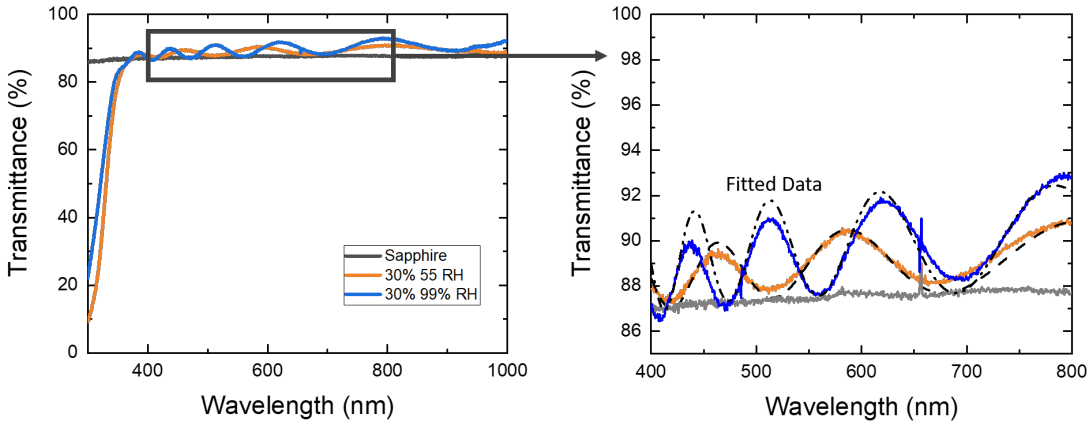

Figure 21 Fitted UV-Vis-NIR data using Swanepoel first method approximations. values being fit are unfixed and allowed to be fit and adjusted. This process is iterated as all the Cauchy parameters are fit and adjusted.

minimal scattering. The interfere patters were then used for the transfer matrix method fits seen in the figure on the right. To perform these fits, approximate values for the optical constants gathered from the Swanepoel method were primarily used as initial Cauchy values. The model was set to fit one parameter at a time resulting in adjustments to each initial assumption. The refractive index was the first parameter that was fitting because its value for the materials being used fall between 1.6 to 1.9. After the value of the refractive index is fixed, the wavelength dependent portion of the refractive index and thickness are isolated then fitted for by iterating the same process. This process is continued on each data set until the best fitting curve fits the experimental data.

Using the transfer matrix method proved to be a more robust method of fitting for the films thickness and refractive index because adjustments to the code can be made to account for scattering phenomena. Scattering in these samples made using the Swanepoel method non-ideal in identifying the initial optical parameters of the hydrophobic samples that often-displayed disordered fringe patterns. Therefore the transfer matrix method was used with estimated first approximations of the polymer thin films refractive index during the evaluation of swelling phenomena in polyvinyl alcohol films that contain various amounts of crosslink material. [101]

CHAPTER 4. POLYMERIC DISTRIBUTED BRAGG REFLECTORS FABRICATION AND PROPERTIES

4.1 Background of Polymeric

Polymeric distributed Bragg reflectors have received increasing attention due to their simple planar structure, which consists of alternating layers of dielectric materials, and because of their well understood governing physics. To this end, distributed Bragg reflectors are currently used to enhance photon absorption, anti-reflective coatings, lasing, and vapor sensing.[94, 102, 103] However, distributed Bragg reflectors have not been extensively investigated for their thermal conductivity and optical reflectivity switching capabilities which could to potentially improved conduction and radiative management of buildings. Moisture uptake through polymer swelling can alter both the thermal conductivity and radiative reflectivity by altering the microstructure of the material and changing its refractive index. Controlled responses in polymeric DBR's can be understood by considering the rational design of the device, previous covered in Chapter 3, and through manipulating polymer film characteristics used to create the dynamic properties in organic distributed Bragg reflectors.

4.2 Polymeric DBR Materials

Distributed Brag reflectors were constructed using commodity polymers dissolved in orthogonal solvents. Specifically, polyvinyl alcohol (60.1 g/L) dissolved in water and polymethylmethacrylate (41 g/L) dissolved in dichloromethene were purchased from Sigma Aldridge. Nominally, PMMA and PVA have refractive indexes of 1.50 and 1.48 respectively.[104, 105] Recall from Chapter 3 that low contrast between the refractive

indexes of the layers which make distributed Bragg reflectors result in poor reflective properties, therefore, to increase the refractive index contrast PVA was crosslinked with titanium tetrachloride hydrate. Figure 22 shows a representative chemical scheme of PVA crosslinking with titania species and yielding TiO_x moieties. These two solutions were deposited on glass, sapphire, and silicon wafers to characterize their optical and thermal properties.

4.3 Thin film processing techniques

4.3.1 Spin coating

Spin coating was used to fabricate single layers of PMMA and PVA to characterize the thermal conductivity and optical properties of the individual layers that make up the polymeric DBR stack. Specifically, films were casted on both transparent substrates such as glass or sapphire, and on intrinsic silicon wafers using a Laurell WS spin coater. A dynamic spinning process consisting of an initial 300-rpm spin cycle for 45 seconds and a secondary spinning cycle of 1000 rmp for 15 seconds was used to make the single layer

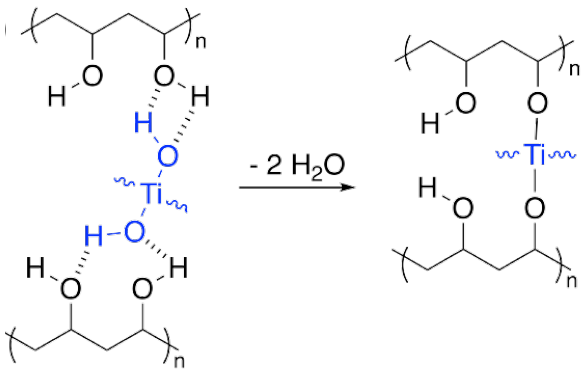

Figure 22 Chemical scheme showing the formation of the PVA-TiOx hybrid layers.

films. The films were then annealed at 50 °C°C and 100 °C°C then dried in a dissector for 5 days.

4.3.2 Sequential dip coating

Full DBR devices were fabricated using a fully automated sequential dip coating process with 20-minute drying steps in between dips. Figure 23a shows the specialized vials containing the either polymer solution placed at programmed coordinates for the automated control arm used to control the movement of the deposition substrate. Equation

$$d_{L,H} = h_{0(L,H)} = c\frac{\eta U_0}{\gamma^{\frac{1}{6}}(\rho g)^{\frac{1}{2}}} \tag{20}$$

20 describes the parameters of the Landue-Levich formulism that was used to estimate the thickness ($h_{0(L,H)} = d_{L,H}$) of each layer to achieve the necessary quarter wave conditions for reflection.[106]

It is clear from this formula that the thickness ($h_{0(L,H)}$) is a function of the solution viscosity (η), surface tension between the liquid and gas phase (γ), density of the liquid (ρ), constant (c) related to the curvature of the dynamic meniscus, the gravitational constant (g), and withdraw speed (U_0).[107-109] The viscosity, density, and surface tension of the solution are believed to change slightly due solvent evaporation over the course of the fabrication process. This change was observed to have a negligible effect on the mirrors performance once it was mitigated using slit parafilm covers to reduce the surface area of the opening. The gravitational and dynamic meniscus constants do not

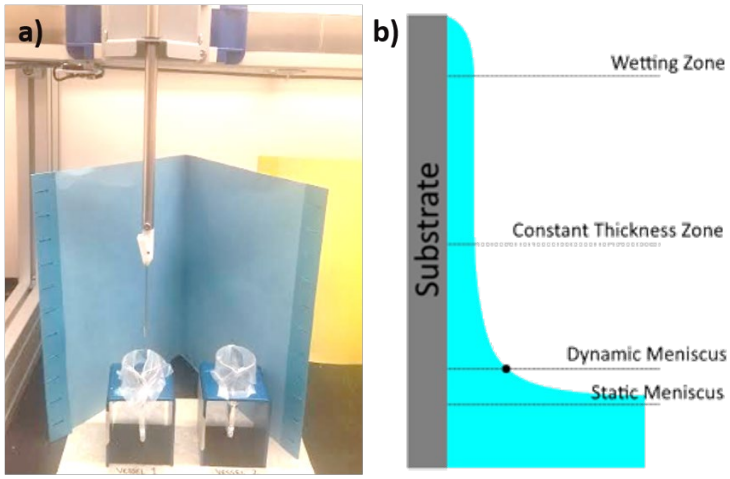

Figure 23 a) Photograph of the automated dip coating and a cartoon of the various regions on a substrate being dip coated. b) Illustrates the various zones on present during the dip coating process.

change during the dipping process. Therefore, the withdrawal speed was used to control the thickness of the PMMA and PVA-TiO_x layers within nanometers of the targeted values. Once full DBR stacks were completed they were desiccated for 5 days before being diced in halves and annealed at 50 °C°C and 100 °C.

4.4 Instruments and Experimental Set-up

4.4.1 Optical measurements

Optical measurements were completed on as fabricated and thermally treated samples using a Cary 5000 UV-Vis-NIR spectrometer. This technique is non-destructive and is ideal for assessing material responses to thermal radiation across the 200nm to 1300nm wavelengths. Specifically, this UV-Vis-NIR instrument utilizes dual beams of light to characterize the transmittance, absorbance, and or reflectivity properties of samples

by comparing them against a fully transparent or reflective references as a function of wavelength. It is important to note that the polymeric distributed Bragg reflectors used in this study are highly transparent structures and are believed to exhibit negligible light absorption. Therefore, the sum of the materials transmissive and reflective response equals unity, a value that corresponds to the full intensity of reference beam.[110] Equation 21 show the relationship between this material's optical properties,

$$1 = T + R \tag{21}$$

where T and R are the transmissive and reflective responses of the material respectively. Although the polymeric distributed brag reflectors were assessed for their potential as radiative reflectors, transmittance data was used in our studies and converted into reflectance using Equation 21. As discussed in the Chapter 3, modeling transparent thin films is done through fitting experimental transmittance data using the transfer matrix method.

To study the in-situ swelling behavior of responsive polymer hybrids additional transmittance measurements were carried out on the films while they were placed in an Espec humidity chamber. The in-situ optical data gathered was a function of relative humidity cycles and corresponded to the material's thermodynamic properties. The Espec chamber allowed for humidity ranges, ramp times, and temperature to be controlled for fully automated material characterization. More importantly the chamber housed an Avantes ULS4096CL spectrometer capable of taking continuous transmittance measurements. Measuring samples every one or two minutes was found to be ideal in analyzing the different polymer composites responsiveness to humidity cycling. Figure 24

Figure 24 Photograph of the experimental setup for in-situ transmission measurements as humidity in the chamber was cycled between 55 and 95% RH

show a photographic image of the experimental setup for in-situ transmission measurements as humidity in the chamber was cycled between 55 and 95% relative humidity. The Avantes software also allowed the collected data to be consolidated and transferred for ease of analysis.

4.4.2 Differential 3-omega measurements on polymer layers

The differential 3-Omega technique is a method that leverages an analytical heat transfer model to solve for the thermal conductivity of thin films. The technique requires a metal heater lines to be deposited on the surface of a sample.[111] These conductive lines experience joule heating as a sinusoidal current is applied over different frequencies to produce periodic temperature oscillations that are then measured and used to calculate the

thermal conductivity of the film. Equation 22 give the general solution of for the change in temperature,

$$\Delta T_{s+f} - \Delta T_s = \frac{P d_f}{2bLk_f} \tag{22}$$

where ΔT_{s+f} and ΔT_s are the measurable changes in temperatures of the film coated substrate and the bare substrate respectively. The power term (P) is determined by the input current and the resistance of the heater line, while the film thickness (d_f) of the sample was measured using profilometry. The nominal values of the half width of the heater line (b) and the length of the heater line (L) are determined by the template used during the deposition. Therefore, by measuring the temperature responses of both the film covered substrate and the substrate itself the thermal conductivity of the film (k_f) can be determined. [112-114] This technique was employed to measure the thermal conductivity of the individual thin film layers used to construct distributed Bragg reflectors which in turn could be used to approximate the thermal conductivity of full DBR stacks. Figure 25a shows a photograph of 3-Omega probes attached to a thin film sample to measure its thermal conductivity in the dry state. In this image the outer black and red probe tips are

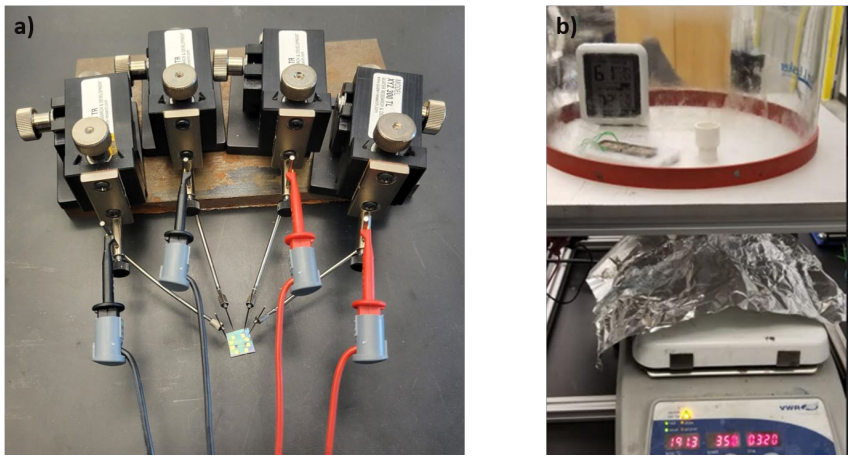

Figure 25 Photographs of the 3 Omega setup used to collect the thermal conductivity data on the DBR films. a) Polymer films measured in the dry state. b) Thermal conductivity set up for films measured under humid conditions.

connected to the sinusoidal current source and sends modulated signals across the gold heater line. This causes joule heating to occur and raises the resistance of the conductive material. The raise in resistance alters the voltage across the heater line.[115] This change in voltage is measured by the inner black and red probe tips then the measured data is used in an analytical model to calculate the corresponding change in temperature.

The thermal conductivity of humidified films was also measured to study the thermal switching capacity of hydrophilic PVA-based films containing different amounts of crosslinking TiO_x material. To achieve the proper measurement environment, a custom apparatus was built. Figure 25b is a photograph of this custom setup used to take thermal conductivity measurements while films were subjected to a 95% relative humidity environment. The set up consist of a lab made rectangular prism made from aluminum with a solid aluminum block at the top of the structure containing three lead holes. These holes were used to introduce water vapor into the dome, transfer electrical wires for

measurements, and as outlets to adjust the humidity levels which were constantly monitored using a hygrometer. Several sets of wires corresponding to different samples were fed through the electrical wiring outlet which make measurements on multiple samples possible without obstructing the humid levels in the chamber.

4.5 Results

4.5.1 Optical properties of hybrid layers

Maximizing the reflecting capabilities in these devices was achieved by modifying the refractive index contrast between the PMMA and PVA bilayers. Low contrast in refractive indexes result in dismal reflective properties, therefore, to increase the refractive index contrast PVA was crosslinked with variable amounts of titanium tetrachloride suspended water. Figure 26 shows the refractive index as a function of the fabrication volume fraction of TiO_x in the as cast and thermally annealing PVA-TiO_x composites. These index values were measured using UV–VIS–NIR spectroscopy. The dashed line shows that the index of refraction of a pristine PVA film is 1.48 at 550 nm. Additionally, adding TiO_x increases the index of refraction as expected, and is attributed to the incorporation of the higher dielectric ceramic material into the polymer matrix.[116-118] As the higher dielectric material was incorporated into the matrix in greater quantities the refractive index of both the as-cast- and thermally-annealed-films increased, however, this increase plateaued in as-cast-films after loading fractions exceeded 80 percent. After this point the refractive index remains constant in as-cast-films and slightly decreases in thermally-annealed-films. The decrease in the refractive index after this benchmark is hypothesized to result from

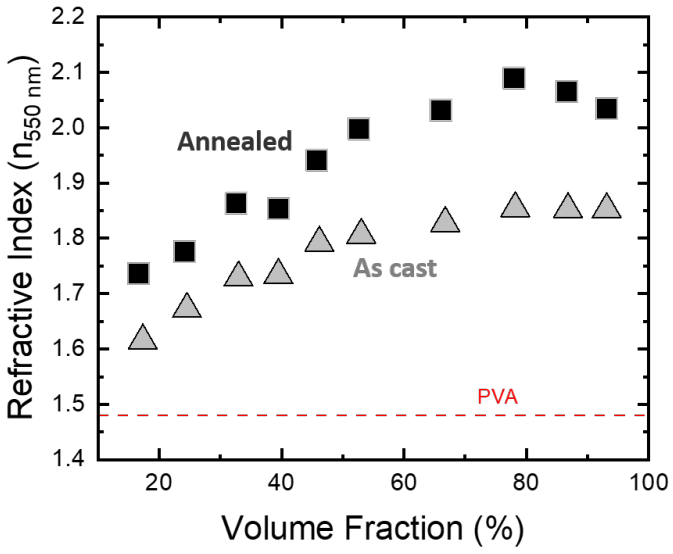

Figure 26 Change in PVA hybrid layer index of refraction as a function of annealing and TiO_x volume fraction.

scattering caused by the formation of polynuclear TiO_x structures between polymer chains. As seen in Figure 22, PVA contains single chemically active hydroxyl sites bonded to a carbon in between methylene like structures. The titania species introduced in the polymer solution is theorized to displace hydroxyl bonds to form a crosslinked network with water and chlorine as its by-product. As available hydroxyl sites on the polymer backbone become increasingly occupied with more inorganic material the optical thickness, a term used to couple the refractive index and physical layer thickness, of the hybrid layer eventually exhibiting reduced effectiveness.[119] It was hypothesized and later confirmed using Grazing Incident Wide Angle X-Ray Spectroscopy (GIWAXS) that the titania species forms clusters by bonding with itself and "undensifying" the polymer matrix by spacing out the polymer chains.

To quantify the films dynamic response to the water vapor analytes, as-cast- and thermally-annealed-films were dried in a dissector for five days then exposed to 95% relative humidity at 22 °C in a humidity chamber. Figure 28 shows representative effects of humidity exposure on the thickness and the refractive index of an as-cast-film fabricated with 30% TiO_x as a function of time. Notably, the film thicknesses increase is sigmoidal with respect to time, which is not consistent with Fickian-like diffusion kinetics ($t^{\frac{1}{2}}$ dependency). [120, 121] This indicates that the water vapor incorporation could be a convolution of both diffusion and reaction kinetics. [122] In contrast the refractive index of the film experiences an immediate and sharp decline during initial exposure to the humified environment. After this time, the refractive index was observed to gradually increase. The immediate decline in the refractive index and gradual increase in thickness agrees with literature findings on hysteresis effects that are characteristic in polymer gel systems. [123] The swelling phenomena in single hybrid layers is believed to follow the

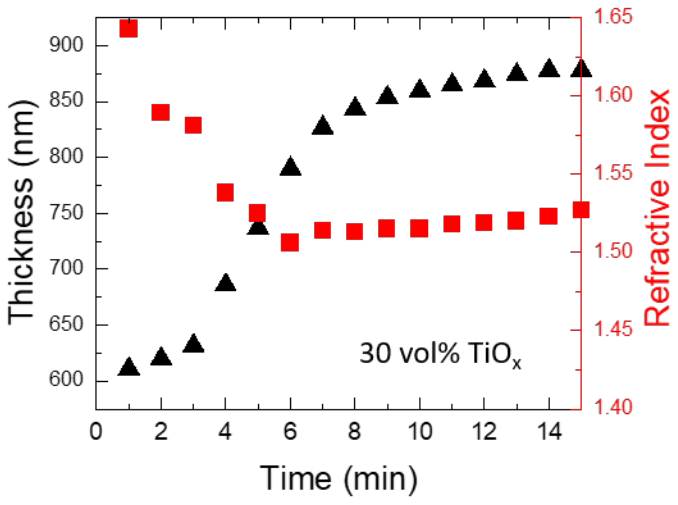

Figure 27 Representative change in the PVA-TiO_x hybrid layer's thickness and refractive index as a function of time exposed to 95% relative humidity.

thermodynamic principles of polymer swelling first presented through the Flory-Rehner polymer swelling theory. In detail solvent entering the structure must provide enough energy to overcome the configurational entropic forces that cause the polymer to coil into low energy states. Once the driving force that promotes mixing between the solvent and polymer matrix exceeds the free energy associated with elastic deformation the film begins to swell.[124] The rate of swelling increases until the free energy associated with the elongated polymer equilibrates with the free energy of mixing. [28, 125] This trend confirms that the effects seen on the refractive index decreases upon the onset of humidification as low index water molecules immediately enter into the polymer matrix. Afterwards, chemical and/or density changes to the microstructure occur and mitigate additional decreases in the refractive index despite the continued increase in thickness.[126] Polymer swelling characteristics are theorized to depend on the crosslink density of the inorganic TiO_x species in between PVA chains. Figure 28 shows the swelling ratio in films as a function of inorganic crosslink volume fractions in the hydrophobic hybrid material. As the concentration of the titanium hydrate used in the initial fabrication of the film is increased, the swelling response in the presence of water vapor decreases. Specifically, a moderate degree of swelling occurred in PVA-TiO_x films with a 30% loading fraction. As the volume fraction of TiO_x increases to 60%, swelling is observed to be less than 10% on average. It is important to note that the hypothesized crosslink saturation point occurs after the TiO_x volume fraction reaches 56%. At this point all available hydroxyl sites on the PVA structures are theoretically being used as crosslinking sites; meaning there exist a one-to-two pairing between the inorganic crosslinker and the available bonding sites on the PVA. Swelling is believed to still occur in the film fabricated

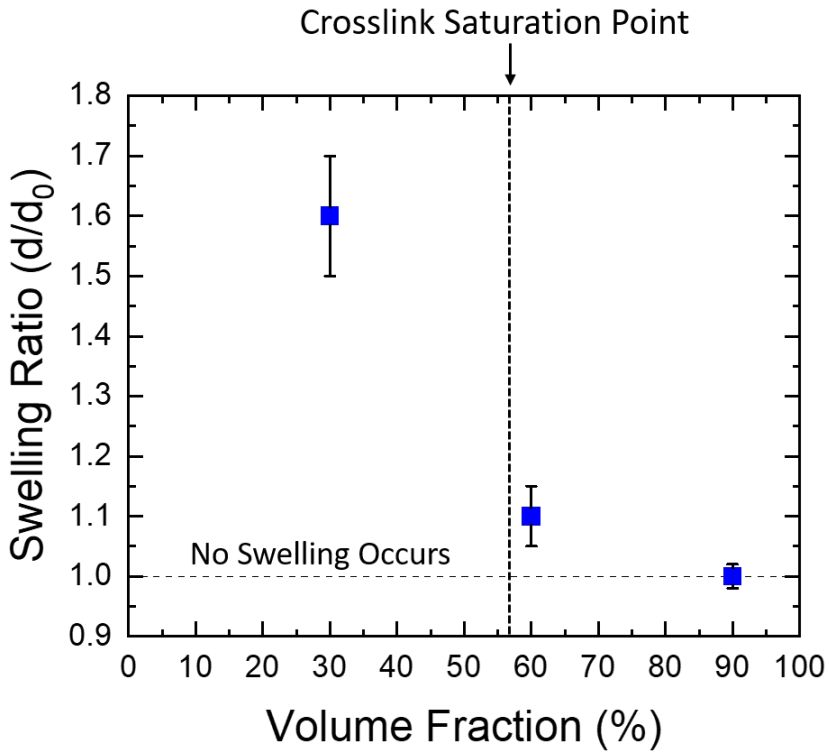

Figure 28 Change in PVA hybrid layer index swelling ratio as a function of TiO_x volume fraction.

with 60% TiO_x due to the formation of polynuclear clusters which allow available hydroxyl sites on the polymer to remain active for solvation. Assessing the humidity response of the film as the volume fraction as is pushed to 90% further supports this claim. No swelling occurs, and it is believed that excess crosslinking material increases the likelihood of satisfying all available hydroxyl sites on the PVA. Understanding the precise physical and chemical mechanisms in each regime is an area of future investigation, however, this characteristic was exploited to investigate the dynamic behaviour of polymeric distributed Bragg reflectors fabricated with hybrid films with specified concentrations of the hybrid material.

4.5.2 Thermal conductivity of hybrid films

As water is incorporated into the polymer hybrid matrix, one can expect the thermal conductance of the film to change as a function of moisture uptake.[127-129] To investigate this material property the thermal conductivity of hybrid films made with various TiO_x-PVA concentrations was measured using the differential 3-Omega technique. Figure 29 shows the thermal conductivity of the films as a function of TiO_x volume fraction in both the dry and humidified state. The thermal conductivity of dry films increases as the TiO_x volume fraction increases. This increase is because TiO_x has a greater thermal conductivity which ranges from 0.7 to 0.9 $Wm^{-1}K^{-1}$ and its addition is in qualitative agreement with the effective medium approximations.[78] Upon humidification, note that thermal conductivity increases as a function of the TiO_x volume fraction. Hybrid films

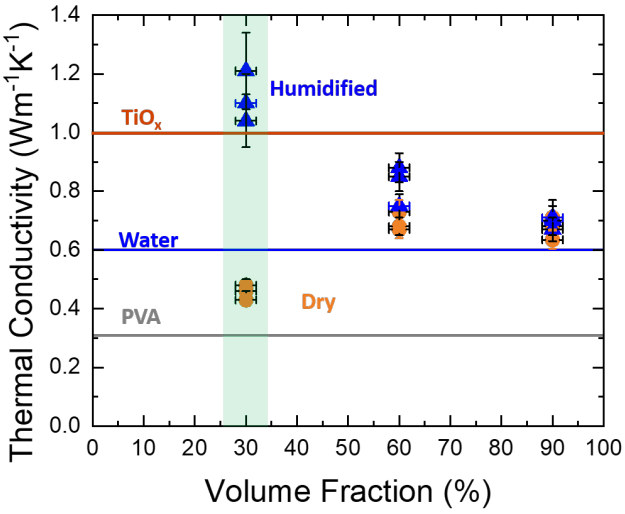

Figure 29 Thermal conductivity values of dried films seen in orange circles and humidified films seen in blue triangles as a function of TiO_x loading. Thermal conductivity switching ratio at 30% TiOx loading is denoted by the grey arrow. The solid blue line denotes thermal represents thermal conductivity of water and the grey represents the thermal conductivity of the PVA without any TiO_x loading.

fabricated with 30% TiO_x hydrate to PVA exhibit a 3-fold increase in thermal conductivity. Astonishingly, this large increase in thermal conductivity exceeds values predicted by the rule-of-mixture suggesting that there is an additional contribution to the thermal conductivity resulting from polymer ordering.[130] The thermal switching ratio observed in in hydrophobic PVA-hybrid films make these materials viable to be used as standalone devices for heat management applications that require materials to possess variable thermal conductivities such as chip cooling and integrated shape stabilized phase change materials for buildings. In contrast films with 60% TiO_x only exhibit an average thermal conductivity increase of 8%, while films made with 90% TiO_x show no change in thermal conductivity while being exposed to water vapor. It is known that increasing the volume fraction of stiff crosslinkers in polymer systems increases the rigidity of the microstructure.[131] Additionally, the presents of the TiO_x species prohibit water molecules from binding to hydroxyl sites on the polymer. As result films made with lower volume fractions of the TiO_x species are capable of changing confirmations to incorporate larger quantities of water molecules and thus are capable of larger degrees of swelling and thermal switching.[132, 133]

4.5.3 Dynamic optical properties of distributed Bragg reflectors

Polymer based reflective materials have been identified as a promising low-cost device that can be readily applied to new and existing building envelops. A thorough investigation was completed to understand polymeric DBR responses to thermal radiation to elicit their ability to reflect variable amounts of solar radiation away from building envelops. In this study UV-Vis-NIR spectroscopy was used to measure the radiative responses for distributed Bragg reflectors fabricated to reflect near infrared radiation. The

measurements were taken between 400 and 1400 nm wavelengths. Figure 30 shows the reflectance of an as-cast and thermally annealed 16.5 bilayer distributed Bragg reflectors that were made using alternate layers of polymethylmethacrylate and titiana modified polyvinyl alcohol. The as cast polymeric material seen in black has a strong reflectance around 1340 nm. This location is known as the operation wavelength and can be tuned by manipulating the physical parameters of the polymer stack. Additionally, this wavelength defines the primary region being reflected and this mirror has an as cast maximum reflectance of 78% and a total bandwidth (the total width of the reflectance band) spanning

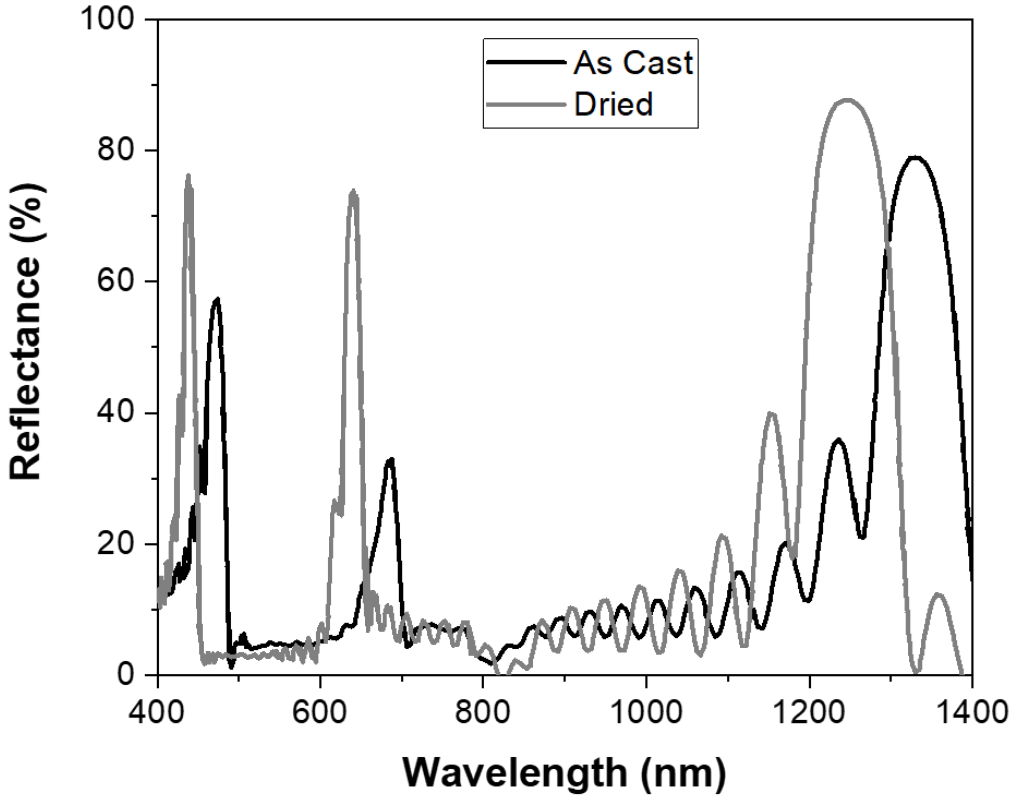

Figure 30 Reflectance UV-Vis-NIR spectroscopy of 16.5 bilayer DBRs for the as-cast (grey) and thermally annealed (black) films. Inset photograph on the left illustrates transmission in the visible spectrum. Inset photograph on the right illustrates reflection in the NIR.

150 nm. Secondary and ternary peaks at 670 nm and 460 result from higher order constructive interference conditions being stratified at smaller wavelengths within the structure.[134-136] In contrast, the same DBR was thermally treated at 100 °C for 20 minutes and is shown in gray as the dried film. Here, the first experimentally validated inference of dynamic radiative switching in polymeric distributed Bragg reflectors was observed. This can be seen in the operating wavelength shift to 1250 nm. The peak reflectance associated with this thermally treated device also increased to 86% at this wavelength and the bandwidth is widened to 200 nm. Specifically, a 90 nm blue shift in the operation wavelength occurred after the as cast device was thermally treated. The secondary and ternary peaks of thermally treated devices also shifted and intensified. This improvement to the devices reflective capability occurs because the periodicity in between bilayers became more uniform. As discussed in detail in section 3.1.1 the quarter wave specific conditions needed to maximize constructive interference rely on the film's bilayer thickness. As the film water content decreases the hydrophilic PVA-TiO_x layer converges closer to the quarter wave conditions needed for constructive interference. Thus, achieving higher uniformity directly correlates to quarter wave conditions being satisfied in each layer and maximizes total reflectance. Thermal treatment contracts the hybrid layer and the decrease in the film thickness blue shifts the photonic bang gap lower operation wavelengths. The secondary and ternary peaks of the thermally treated films also exhibit higher reflectance magnitudes which further confirms that the bilayers are becoming more uniform and are trending towards satisfying the quarter wavelength conditions. Now that the steady-state properties of DBR devices are better understood and individual thin films, this work transition to assessing their dynamic response. Dynamic properties in polymeric

distributed Bragg reflectors were first demonstrated by thermally annealing the device and observing the increase in the total reflectance and blue shift of the operation wavelength. It was hypothesized that the heating step drives off excess moisture which bolsters the devices refractive index and decreases the PVA-TiO_x layer thickness. To study the full thermal switching capability of the material, the DBR stacks were placed in an Espec humidity chamber and the relative humidity was cycled between 55% and 95% relative humidity. Note polymeric distributed Bragg reflectors with operation wavelengths closer to the visible/NIR wavelengths was used to avoid red shifts outside the operation limit of the spectrometer. Figure 31 shows the total reflectance of the device over UV-VIS-NIR wavelength as the humidity in sample chamber is cycled between the dry state (65%) seen in red and the humidified state (95%) seen in purple. A maximum reflectance of 96% is achieved at 680 nm and has a bandwidth of 200 nm. Upon raising the humidity in the chamber to 95% relative humidity the total reflectance of the operation wavelength is

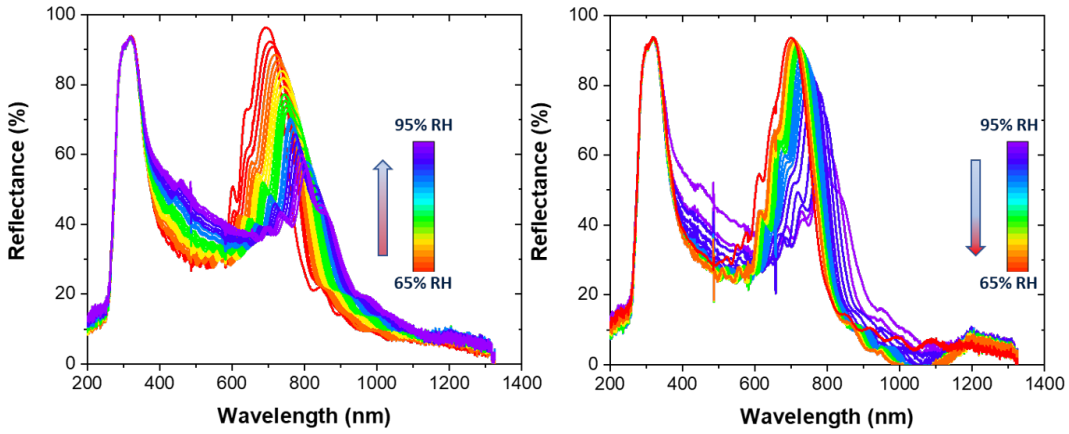

Figure 31 In-situ reflectance UV-Vis-NIR spectroscopy of 16.5 bilayer DBR as a function of humidity cycling. Film characteristics while in the dry conditions at 65% relative humidity are denoted by the red line. Film characteristics while in the humidified state at 95% relative humidity are denoted by the purple line.

reduced by 45% and had a peak transmittance value of 53% and the bandwidth of the photonic band gap in the humidified state decreases to 170 nm. The location of the operation wavelength was also redshifted and recentered at 820 nm. Consistent with the governing equations 10-13 the reduction in the reflective properties of the film and new position of the photonic band gap are attributed to layer-to-layer deviation from quarter wave condition and reduction of the refractive index contrast between the two dielectric materials. As water vapor penetrates the DBR stack and swells the hydrophilic layers the increase in thickness, term $d_{(H)}$ in Equation 10, shifts the operational wavelengths to larger values. The decrease in the reflectance magnitude and shortening of the bandwidth occurs because the incoming water vapor has a lower index of refraction than the hybrid matrix. Figure 31b shows the reflectance of the same 16.5 bilayer DBR as a function of dehumidification from 95% relative humidity back to 65% relative humidity. As the device is placed in the dry state the original operating wavelength and magnitude of reflectance is restored to 680 nm and 96% reflectivity, respectively. These results suggest that water vapor which entered the polymer hybrid at high relative humidity was dispelled from the structure until equilibrium conditions with the environment were achieved. Interestingly, reflective peaks in 16.5 bilayer DBR stacks made with PVA-TiO_x films consisting of 60% inorganic material by volume fraction do not completely vanish due to the small degree of swelling. The degree of swelling directly alters the coherent interference needed to alter the reflectivity of the device and the limited swelling in DBR containing hybrid layers with 60% TiO_x content are unable to swell to a degree that is large enough to completely obstruct the photonic stop band.

In contrast, Figure 32 shows a 16.5 bilayer DBR made with PMMA as the standard low index layers but has high index layers made from PVA-TiO_x films containing 30% inorganic material by volume. This device was fabricated to have an operation wavelength which reflects around 1000 nm. In its dry state the max reflection occurred at an operation wavelength of 980 nm and had a total reflectance of 65% with a 220 nm bandwidth. The smaller reflection peak is due to the lower refractive index contrast between the polymer layers. Additionally, the accuracy of the operating wavelength location is due to thicker hybrid layers needed to achieve the quarter wave conditions as outlined in Equation 10. Unlike the DBR stack made with higher volume fraction of the titania species, this DBR's reflective band completely vanishes as the structure was exposed to 95% relative humidity. This result indicates that the layer thicknesses needed to achieve constructive interference had completely been obstructed. Upon dehumidification the thickness of the hybrid layers decreases which indicted that water was diffusing out of the polymer matrix. This is

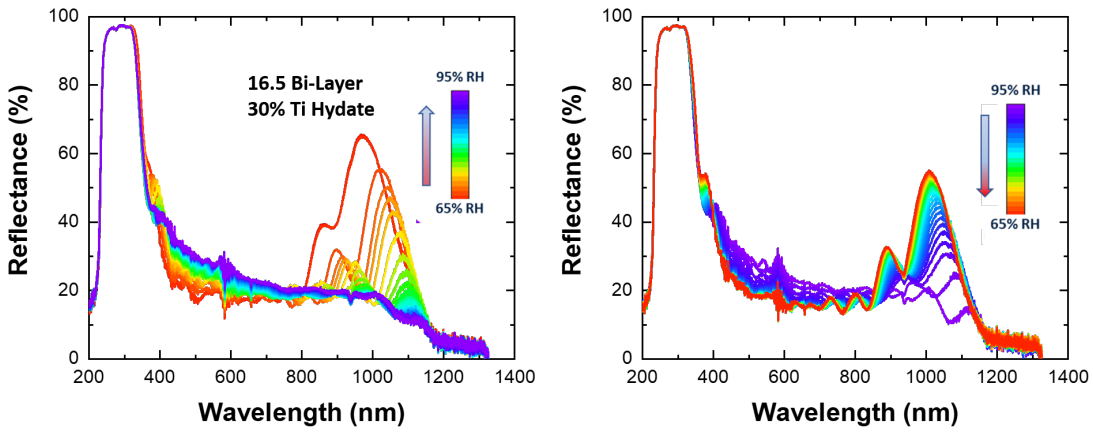

Figure 32 In-situ reflectance UV-Vis-NIR spectroscopy of 16.5 bilayer DBR as a function of humidity cycling. Film characteristics while in the dry conditions at 65% relative humidity are denoted by the red line. Film characteristics while in the humidified state at 95% relative humidity are denoted by the purple line.

indicated by the immediate return of the small photonic band gap structure that begins to form around 1120 nm. As the testing environment returns to the lower humidity value the total reflection of the photonic band gap of the device continued to increase, however, once the chamber reached its equilibrium of 65% relative humidity, the maximum peak value did not return. Instead, the maximum reflection peak and the operating wavelength experienced a 10% reduction and the new location of the operating wavelength shifted 1000 nm. It is hypothesized that the increased number of available hydroxyl sites make solvent diffusion out of the structure energetically unfavourable at lower relative humidity values (*i.e.*, the solvent molecule interacts with more hydroxyl bonds as it diffuses out of the structure). After this initial reduction in the reflective properties the material were capable of being cycled as a function of water vapor concentration in the system.

Notably, the distributed Bragg reflectors operating wavelength location returned to 680 nm and 820 nm upon cycling the humidity in the chamber between 65 and 95% relative humidity in devices. The peak reflectance values corresponding to low and high relative humidity condition also was shown to cycle between their original values of 96% and 53% reflectivity, respectively. The switching capabilities of this DBR structure lasted for 15 humidity cycles before the reflective properties became fixed. Figure 33 shows the reflectance of the 16.5-layer DBR stack upon additional cycling. The position of the operating wavelength is fixed at 650 nm irrespective relative humidity in the chamber. Ten additional cycles confirm the fixed radiative properties and microstructure. It is hypothesized that the free bonds believed to be present on the TiO_x species can interact with other inorganic materials and bond to each other between crosslinks on the PVA to lock the structure once allowed to flow during humidity exposures. Further investigation

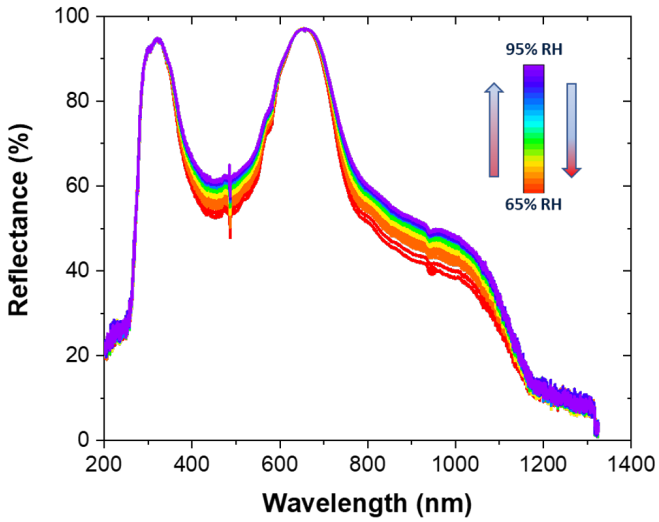

Figure 33 In-situ reflectance UV-Vis-NIR spectroscopy of 16.5 bilayer DBR as a function of humidity levels after 15 cycles.

of the crosslinking nature of these ceramic fillers is critical to fully characterise and control the dynamic behaviour of films used to fabricate polymeric distributed Bragg reflectors for use as radiative shields and thermal switches.

4.5.4 Analysis using Flory Rehner polymer swelling theory

To understand the extent in which the Flory-Rehner theory for polymer swelling can be used to engineer dynamic layers used to make distributed Bragg reflectors the swelling data from the samples were used in the model. The PMMA layer used as the low index layer has been reported to swell less than 3% in the presence of water, therefore its effect on altering the reflective properties of the mirror were not considered in this evaluation.[137, 138] Instead the role of the high index PVA-TiO_x hybrid layers are discussed. The volume fraction of the swollen polymer (v_2) was determined by dividing the thickness of the dry film by the thickness of the swollen film using the measured values

acquired through the UV-Vis-NIR spectrometry. Equation 23 gives the relationship between the measurable film volume and its volume fraction in the swollen state. To evaluate our specific system using the Flory-Rehner model:

$$\frac{V_{Swollen}}{V_{dry}} = \frac{1}{v_2} \tag{23}$$

a molecular weight (M) of 120,000 provided by the manufacturer was used along with the density (ρ) of the polymer and the Flory-Huggins interaction constant (X) values of 1.19 and 0.494 that were found in literature.[139, 140] To determine the molecular weight of the polymer between crosslinks the aforementioned data was used in the full model. As expected, the Flory-Rehner model showed highly crosslinked films to have swollen polymer volume fraction (v_2) near unity. Meaning the solvent does not interact with the polymer structure enough to induce swelling and that the molecular weight of the polymer between crosslinks (M_c) is small. As the crosslink density was decreased larger volume fractions of the swollen polymer were observed. In films crosslinked with 30% volume fraction of inorganic material, the volume fraction of the swollen polymer (v_2) was measured to be 0.59 and the average weight between crosslinks was found to be 70 grams per mole. In all it was found that the Flory-Rehner model for polymer swelling is more suitable for determining the crosslink density of the film. This material characteristic was calculated by dividing the average molecular weight (M) of the polymer by the molecular weight of the polymer between crosslinks (M_c).

Determining the crosslink density is of interest to better understand the interactions between the polymer and inorganic material. It was believed that the TiO_x species contains

dangling bonds capable of forming polynuclear clusters in between crosslinks. By observing similar the crosslink densities in films processed with large amounts of TiO_x, one could infer that the excess inorganic material must either be physically incorporated or chemically bonded in the polymer matrix. To investigate this polymer films were rinsed in water to drive off any loose material that was not physically in the polymer matrix. Figure 34 shows the GIWAXS data for PVA, ALD TiO_2, and the hybrid materials with various loading fractions of the titania species. Notice that PVA has a strong peak around 1.4 inverse angstroms that begins to decrease as the content of the TiO_x increases. This peak becomes completely flattens after the volume fraction of the TiO_x exceeds 50%. In contrast, the peak associated with the ALD TiO_2 is located around 2.1 inverse Å. Interestingly, peak formations associated amorphous titania can be seen in hybrid films processed with 60 and 80% inorganic material, serving as further evidence that the TiO_x content forms clusters with specific interatomic spacing which branch out from crosslink sites.

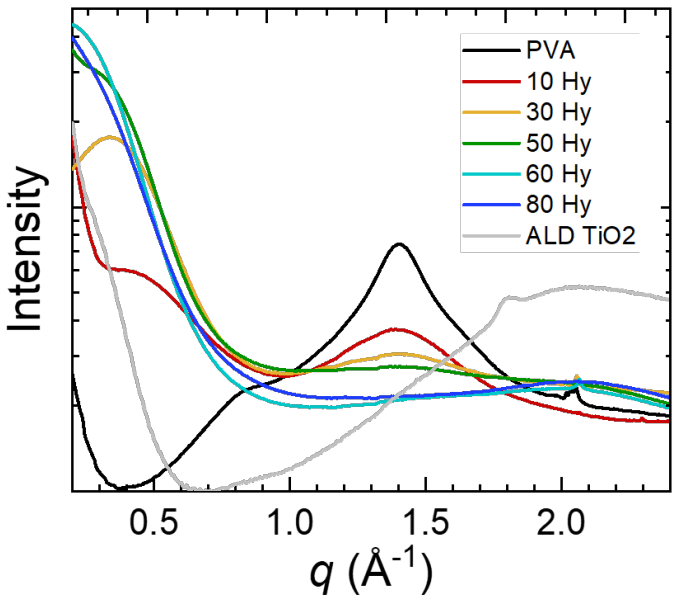

Figure 34 GIWAXS on PVA, ALD TiO_2, and the hybrid materials.

4.6 Summary

Polymeric distributed Bragg reflectors were fabricated using a sequential dip coating process with layer thicknesses that were determined based on the quarter wave conditions needed to create reflection around a specified wavelength. To boost the refractive index, contrast various amounts of inorganic fillers were used to crosslink the hydrophilic PVA. To this end it was found that the swelling capabilities of the PVA-TiOx decreased as the volume fraction of the inorganic filler increased. No swelling was observed in films that were processed with 90% volume fraction of the organic material, meaning that full DBR stacks made from these films do not exhibit dynamic reflective behavior. The Flory-Rehner model for polymer swelling was found to be better suited for understanding the behavior of the inorganic crosslinker rather than being used as a predictive model for tuning the reflective band. The model was key in determining the crosslink densities of the films. This information was coupled with GIWAXS data to further understand the role of the inorganic filler.

Interestingly, in hybrid films made with 30% and 60% volume fractions of the organic species 70% and 10% swelling was observed respectfully. The swelling in these films was associated water uptake by the polymer. This uptake in water, a material which has a thermal conductivity (0.6 $Wm^{-1}K^{-1}$) nearly two-fold larger than the polymer, resulted the thermal conductivity increase in the hybrid films. Specifically, films made with 60% TiO_x content showed a 10% increase in thermal conductivity upon humidification. Astonishingly, films made with 30% TiO_x consistently showed a thermal conductivity increase of over 300 %. This large increase in thermal conductivity is well outside of the predicted values given by the rule of mixture and suggest that the swelling phenomena in

films with lower crosslink densities introduces polymer ordering. This ordering is hypothesized to occur as the polymer expanded to incorporate more solvent molecules. Improved thermal properties in polymers as result of polymer ordering has been observed in literature.[141-143]

CHAPTER 5. THERMAL CONDUCTIVITY AND ENTHALPY OF PHASE CHANGE MATERIALS USED FOR ENERGY STORAGE

5.1 Background on phase change materials

Shape-stabilized phase change materials made with polymer-based constituents have generated interest in the scientific community for their ability to be used as thermal batteries.[144-146] In this chapter phase change materials s were fabricated, engineered, and evaluated to investigate their potential for use as thermal management materials in buildings. Specifically, these materials have the ability to absorb and release stored thermal energy by undergoing phase transitions.[147, 148] These materials liquify once the temperature exceeds their inherent melting temperature and this phase change consumes thermal energy to break bond configurations in the material. This heat absorbed in this transition is stored and used to reduce the thermal load transferred on building. Storing thermal energy in this manner reduces the amount of heat and lowers the amount of energy needed to operate air-conditioning units. Similarly, these materials can recrystallize and releases heat into the environment as the materials molecules configure or freeze into higher energetic states. This release of latent heat from crystallization can offsets the energy needed for space heating.[149] Practical application of these class of materials have been limited by performance deficiencies, which including polymer leakage, extreme moisture uptake from ambient humidity, excessive undercooling to initiate crystallization, and low thermal conductivities. Specifically, polymer leakage is problematic because it causes the “shape stabilized” material to deform. This results from moisture uptake which is the primary source of reflow in these materials. Moisture uptake also alters the

polymer's mechanical properties.[150-152] The needed for large undercooling, which is defined as cooling below the melting point of the material without crystallization, is another issue hindering the use of phase change materials s. Fundamentally, this effect increases the operating temperature range and directly lowers the coefficient of performance in these systems.[153] Lastly phase change materials with low thermal conductivities experience slow heat transfer characteristics which remains a major hinderance in the application of these systems. [154]

5.2 Phase Change Materials

5.2.1 Polyethylene glycol (poly (ethylene glycol))

Poly(ethylene glycol) is a polymer with a low melting temperature that ranges from 30-45 °C° and is known for being a nontoxic, non-corrosive material but more importantly for possessing a high latent heat of fusion.[155, 156] This polymer is soluble in water and is inherently hydrophilic in nature. As a solid-liquid phase change material it is prone to polymer leakage; therefore, the deformation issues associated with moisture uptake were addressed.[157] These materials were shape stabilized with the use of tetraethyl orthosilicate to form entangled polymer networks, however, silica-based derivatives were altered with hydrophobic hydrocarbon units in an attempt to reduce the water uptake in these systems. Additionally, the hydrocarbon chain length was varied between the methyl and octyl configurations along with the introduction of both aromatic and bulky branched alkyl units to reduce moisture uptake. Josh Rinehart synthesized the two options, illustrated in the panels of Figure 35, as paths to reduce moisture absorption and retain desired PCM properties.

5.2.2 Hydrophobic coating

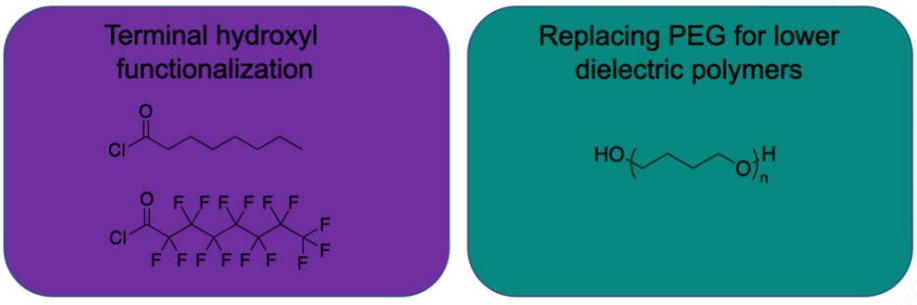

Figure 35 Schematic summary of the routes explored to increase hydrophobicity of poly (ethylene glycol) -based ssPCMs. This image on the left illustrates the configuration of the hydrophobic coatings and the right an alternative hydrophobic polymer.

Hydrophobic coatings were used to investigate their ability to impede the rate of moisture absorption in shape stabilized phase change materials. Specifically, the polar surface of the shape stabilized poly (ethylene glycol) was functionalized using alkyl chains due to their ability to denature hydroxyl groups and hydrophobic nature. Surface functionalization was accomplished by submerging the as fabricated phase change material samples into a solution of acid chloride to react with any exposed hydroxyl groups. Next, different polymer configurations with fewer polar group than poly (ethylene glycol) was assessed.

5.2.3 Boron nitride and poly (ethylene glycol) composites

Boron nitride is a structured element that has been noted to possess a high degree of chemical and thermal stability. With a melting point over 2,970 °C, boron nitride has been shown to be stable in ambient air even as temperatures exceed 1000 °C.[158-160] Although these properties are astonishing this materials value comes from its high thermal

conductivity and ease of processing.[161] Specifically, boron nitride has been modeled to have in plane thermal conductivity values ranging from 1700 to 2000 $Wm^{-1}K^{-1}$ making the material comparable to other hexagonal-lattice based materials like graphene.[162] This material was added to phase change materials in quantities of up to 25 wt% to investigate its effect on the thermal conductivity of the composite. This thesis discusses the effect of boron nitride inclusion on the moisture resistance of poly (ethylene glycol) 1000-based phase change materials. Relative mass changes were measured for each sample during long-term humidity exposure and continuous thermal conductivity measurements were also completed.

5.2.4 Polytetrahydrofuran

Commonly used to make elastic fibers, Polytetrahydrofuran is a chemical compound with a melting temperature that ranges between 20 – 30 °C.[163] Joshua Rinehart produced polytetrahydrofuran pucks that were 1 cm by 1 cm with an average molecular weight of 2000 kg/mol as a hydrophobic alternative to poly(ethylene glycol) -based phase change materials. Water mass uptake and thermal conductivity were measured continuously during long-term exposure to humidity, using the measurement setup described in the instrumentation and experimental set-up section.

5.3 Instrumentation and Experimental Set-up

5.3.1 Thermal conductivity and Mass Uptake Setup

A multifunctional lab made set-up was created to study the dynamic hydrothermal properties of the phase change materials evaluated in this study. In-situ measurements were conducted over the period of 24-96 hours to fully observe the thermal conductivity and mass uptake limits of these materials as a function of humidity. Figure 36 is a photograph of the experimental setup used to collect in-situ relative humidity, temperature, mass uptake, and thermal conductivity data. The specific components of the system consist of a 2-channel hygrometer and temperature probe purchased from Thor Labs, modified transient plane source instrument purchased from C-Therm (previously discussed in Chapter 2), and an Ohaus balance used to measure the mass uptake simultaneously. Notice a fitted extension was used to isolate the sample in the humidity chamber while protecting the electrical components of scale from being damaged. Humidity was generated by heating a large beaker of water using a hot plate and feeding a tube from that beaker to the

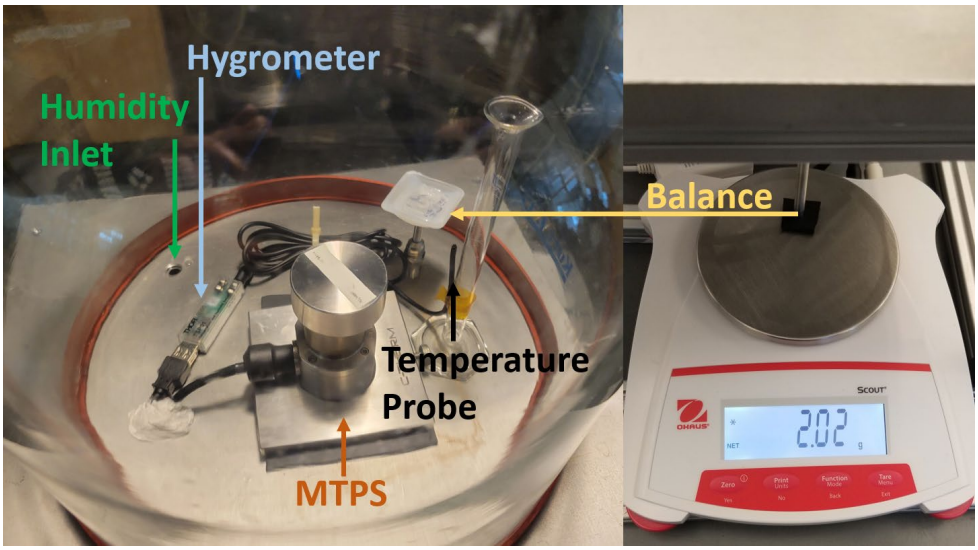

Figure 36 Photograph of the chamber and measurement systems used to collect data on the sample's relative humidity, temperature, mass uptake, thermal conductivity, and regulate humidity levels.

inlet. An outlet hole was used to control the humidity levels in the dome but typically remained plugged because the humidity in the chamber seldomly reached it saturation point. A custom python script written by Dr. Michael Adams was used to automate and integrate the data collected on these samples. The program was able to control three different software simultaneously to collected data on the dynamic environment and sample characteristics every two minutes.

5.3.2 Differential Scanning Calorimetry

To further quantify the thermal storage properties of the phase change materials Differential Scanning Calorimetry (DSC) was used to examine the enthalpy of melting for different derivatives of these materials. Specifically, DSC is a thermo analytical technique used to quantify the amount of heat needed to raise the temperate of a sample in comparison to a standard reference with a well-known heat capacity.[164] As the samples temperature is cycled between high and low temperatures it goes through a phase transformations which manifests as endothermic or exothermic peaks. The peak value location of these endotherms or exotherms describe the materials first-order-phase transition that occur at the materials melting and freezing temperature. The area underneath these curves correspond to the enthalpy values of the material and were used to assess the ability of the material to store and release heat while transitioning from a specific phase. The gathered enthalpy and thermal conductivity data were used conduct the thermal dynamic analysis for these material systems. Figure 37 shows representative DSC data from the poly

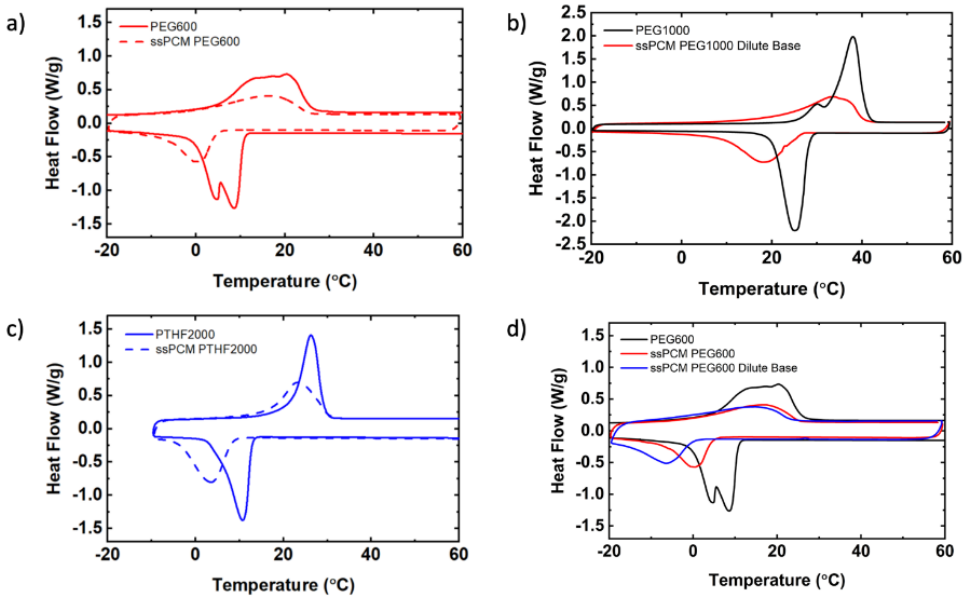

Figure 37 DSC Traces for poly (ethylene glycol) and PTHF polymers and respective ssPCMs. ssPCMs tend to have smaller latent heat peaks shifted to lower temperatures. Specific enthalpy of melting calculated as the integral of endothermal peaks

(ethylene glycol) series investigated in this study. Notice the exothermic peak (pointing upwards) and the endothermic peaks associated with the phase transitions of the material have different magnitudes and widths, which directly corresponds their enthalpy values.

5.4 Material Synthesis

5.4.1 Shape stabilized poly (ethylene glycol) synthesis

The Poly(ethylene glycol) used in this study was synthesized by Joshua Rinehart using the methods outlined in literature.[165] In detail poly(ethylene glycol) with different molecular weights were purchased and melted at a temperature of 50 °C° then various quantities water, sulfuric acid, ethanol, and TEOS were added to polymer solution. To maintain a stable reaction temperature during the reaction container was submerged in a

temperature bath at 50 °C. The solution was allowed to stir for 30 minutes before sodium hydroxide was added. The addition of the sodium hydroxide served as a second catalysis to induced condensation at a faster rate. After the samples were cast in molds to obtain geometries that were suitable for the thermal characterization techniques used in this study. The samples were allowed to gelate before being partitioned into uniform pieces then they were allowed to dry. It is important to note that the samples experienced non-uniform losses in volume during the drying step which caused surface roughness. Dried samples were directly stored in airtight jars to mitigate exposure to ambient humidity. Ramekins coated with a thin layer of Teflon grease produce samples with a large surface, as shown in Figure 38, which was required for modified transient plane source thermal conductivity measurements. Each synthesis generated enough pucks to assess the hydrothermal properties of the shape stabilized phase change material repeatably.

5.4.2 Hydrophobic Coating Synthesis

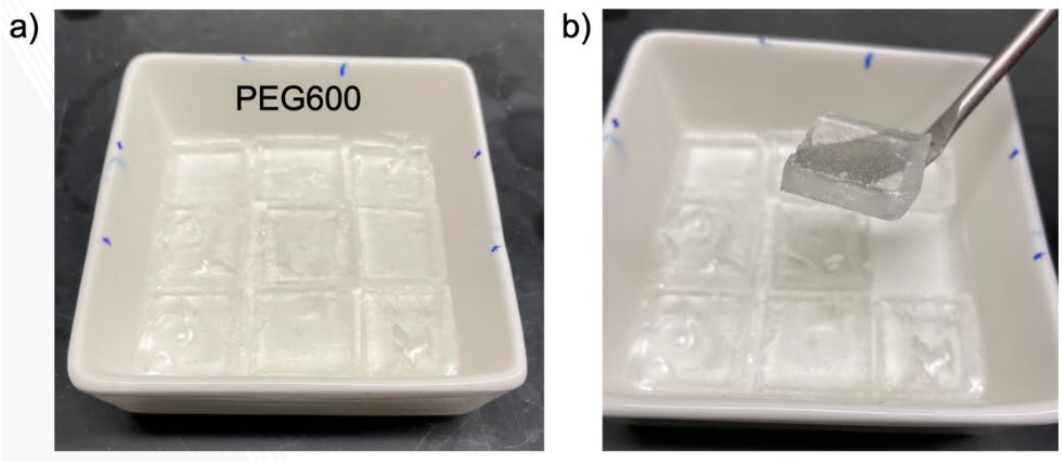

Figure 38 Photographs of poly (ethylene glycol) -600 ssPCM (a) cast into a mold and sliced cleanly (b) samples with flat, smooth surfaces lift easily after drying.

Poly (ethylene glycol) materials coated in n-octyl chains were studied to investigate their ability to functionalize terminal hydroxyl groups with hydrophobic hydrocarbons. Samples were prepared by immersing premade poly (ethylene glycol) pucks with a molecular weight of 1000 kg/mol in a solution of octanol chloride and anhydrous diethyl ether containing a surplus of triethyl amine. The excess triethyl amine served as a base to compensate for the HCl that was produced as a product of the reaction. Specifically, exposed hydroxyl units on the poly (ethylene glycol) and the shape stabilizing silicon derivative served as reaction sites. At these sites a nucleophilic reaction occurred on the acyl unit followed by the discharge of a chloride anion and deprotonation of the hydroxyl group. Then this HCL biproduct was neutralized by the excess triethyl amine in the system. The resulting structure contained ester links that attached the hydrophilic hydrocarbons to the shape stabilized poly (ethylene glycol). The acyl chloride that formed was solubilized with diether ether to removed unwanted byproducts without dissolving the polymer. After two hours of mixing on an orbital shaker white precipitate emerged in the solution. The coated shape stabilized poly (ethylene glycol) at1000 kg/mol was removed from the solution then washed with ether. Lastly the material was dried under high vacuum to remove residual solvent.

5.4.3 Exfoliated Boron Nitride Synthesis

Exfoliated boron nitride containing terminal hydroxyl groups were investigated for use as high thermal conductivity fillers and were relatively simple to synthesize. Figure 39

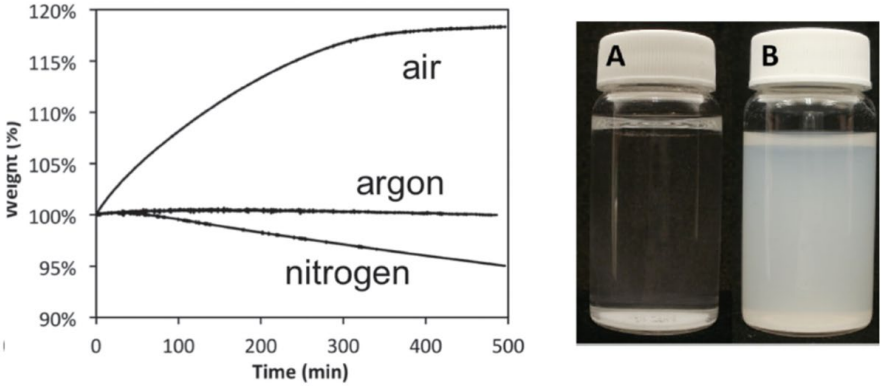

Figure 39 Literature reported mass uptake (left) of h-BN upon heating to 1000 °C in different atmospheres and (right) the change in dispersibility of h-BN before (A) and after (B) oxidation and exfoliation.

shows the heating of boron nitride in ambient air, nitrogen, and argon atmospheres. Specifically, the necessary degradation of the material was obtained by heating it in air to yield oxidized boron nitride with hydroxyl groups. This oxidized material can then be exfoliated. A Temperature of 1000 °C was used to oxidize the boron nitride in air for three hours and resulted in a mass increase of nearly 30%.[166] Afterwards the boron nitride was then sonicated in deionized water for 30 minutes in order to disperse the heat treated particles. The dispersion was dried overnight at ambient conditions before being exfoliated. The boron nitride particles were then dried under vacuum for 24 hours at 100 °C yielding functionalized of boron nitride containing hydroxyl groups throughout the nanosheets. This functionalized boron nitride derivative was hypothesized to provided better dispersions with the shape stabilized phase change materials and polar solvents used in during the fabrication process.

5.5 Results

5.5.1 Mass uptake of coated phase change materials

Moisture uptake experiments were conducted on shape stabilized poly (ethylene glycol) at1000 kg/mol pucks to investigate their ability to impede water absorption. Figure 40 shows the change in mass over time in untreated poly (ethylene glycol) and poly (ethylene glycol) coated with the hydrophobic hydrocarbon chains. To ensure an even comparison coated and uncoated samples were selected from the same batch of materials. Notice the coated samples exhibit a similar trend in water uptake for the first 24 hours compared to the uncoated sample. This suggested that most of the hydroxyl bonds remained intact within the structure and that the primary mechanism for water uptake occurred as moisture diffused into the bulk material. Additionally, it was clear that the capped polar ends of the material located mainly on the surface of the material were unable to impede the moisture uptake rates by the bulk material. It is hypothesized that the distribution of hydrocarbon chains was too large to shield the shape stabilized phase change material from incoming water vapor from entering the structure. Nevertheless, the treated

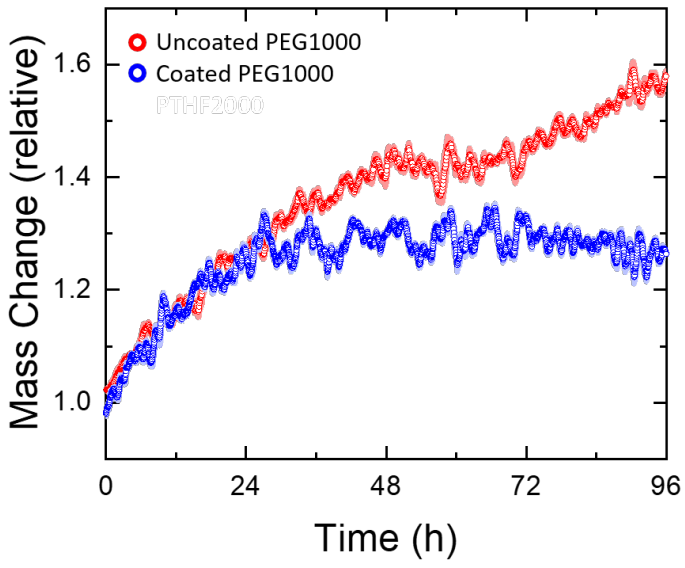

Figure 40 Moisture uptake of coated and uncoated poly (ethylene glycol) -1000-based ssPCM during long-term humidity exposure, normalized by initial mass.

surface treated polymer showed lower moisture uptake over the duration of the study and remains a topic for further research.

5.5.2 Water uptake in poly (ethylene glycol) and polytetrahydrofuran

Polytetrahydrofuran with an average molecular weight of 2000 kg/mol was investigated as a hydrophobic alternative to poly (ethylene glycol) -based phase change materials. Figure 41 shows the water mass uptake measured during continuous exposure to humidity for 4 days of poly (ethylene glycol) -based shape stabilized phase change material with various molecular weights and polytetrehydrofuran with a molecular weight of 2000 kg/mol. The poly (ethylene glycol) at 800 kg/mol and poly (ethylene glycol) at1000 kg/mol exhibited similar rates of water uptake after the data was normalized to represent the relative time-dependent mass uptake compared to the initial mass of each sample. In contrast the polytetrehydrofuran with a molecular weight of 2000 kg/mol showed no significant changes in mass throughout the course of the entire experiment. The hydrophobic nature of polytetrehydrofuran with a molecular weight of 2000 kg/mol is ideal to limit polymer degradation observed in many phase change material systems. However, this material is limited by its relatively low thermal conductivity (0.27 ± 0.06 $Wm^{-1}K^{-1}$) and enthalpy of melting, which makes it unsuitable for use in real world applications. The enthalpy characteristic of the alternative polymer material will be discussed later in this chapter.

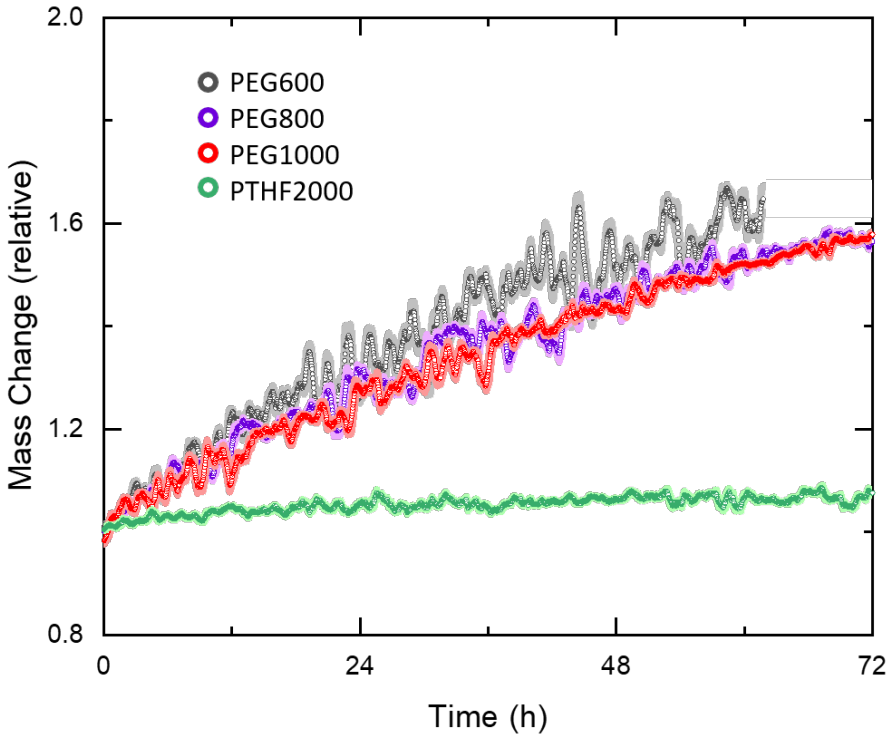

Figure 41 Moisture uptake of various ssPCM samples during long-term humidity exposure, normalized by initial mass. All poly (ethylene glycol) -based samples experience a similar rate of moisture uptake, while polytetrehydrofuran with a molecular weight of 2000 kg/mol shows none.

5.5.3 Mass uptake in poly (ethylene glycol) -boron nitride composites

Boron nitride fillers were incorporated into the poly (ethylene glycol) matrix to increase the thermal conductivity, however, water uptake in these composites was also measured to fully characterize the potential of these composites to be used as PCM materials. Figure 42 shows the relative mass change over four days of continuous humidity exposure in of pure poly (ethylene glycol) -1000 and its boron nitride composites. The poly (ethylene glycol) -1000 maintained a similar relative mass change compared to the hydroxyl functionalized boron nitride PCM composite. However, this moving line average

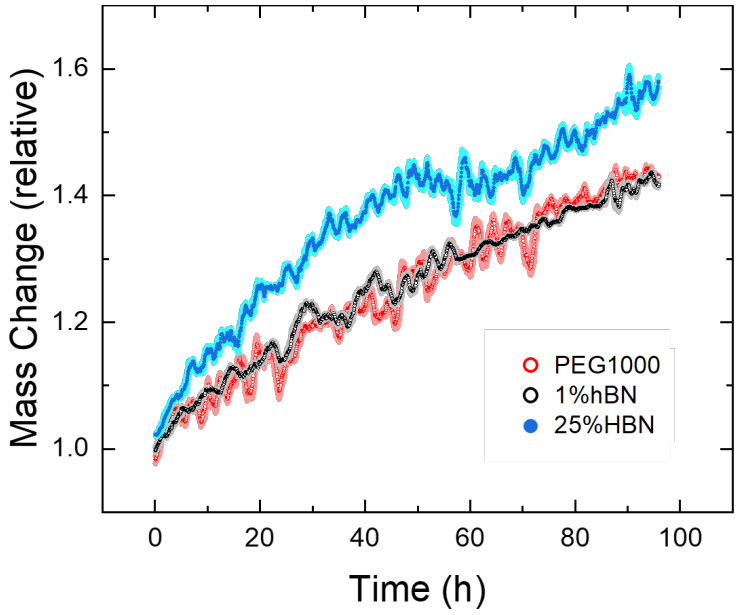

Figure 42 Moisture uptake of poly (ethylene glycol) -1000 PCMs containing boron nitride during long-term humidity exposure, normalized by initial mass. Even large substitutions have little effect on moisture resistance.

of the normalized mass suggest that the mass uptake in composites containing boron nitride exhibited a 13% increase in its relative mass change. It is hypothesized that the boron nitride particles serve points for water uptake to occur by providing micron sized pockets for water to infiltrate and better diffuse through the material.

5.5.3 Polymer Leakage

The mass change data observed in all the poly (ethylene glycol) -series of materials quantitatively demonstrated the material ability to uptake nearly 60% of its weight in water. Figure 43 shows a photograph of poly (ethylene glycol) -1000 that visually shows a pool of liquid surrounding the polymer in the weigh tray and surrounding the sample placed on the MTPS sensor (image on the left). As the liquid dried it was evident that a large amount of the poly (ethylene glycol) -1000 had leached out of the shape stabilizing matrix after the

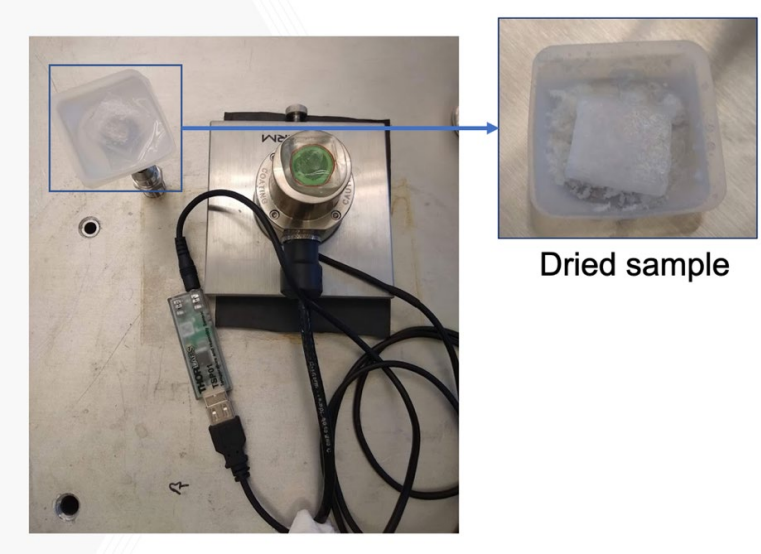

Figure 43 A pool of liquid forms around this poly (ethylene glycol) -1000 shape stabilized phase change material during long-term humidity exposure. Later drying the sample reveals that a significant amount of polymer (32 wt%) leaches from the matrix.

phase change materials was exposed to the 95% relative humidity for the duration of the study (image on the right). Specifically, the material lost nearly 32% of its initial weight after a single run which makes this material unfeasible for used in building applications which require the material to maintain its original geometrical shape. However, this effect can be mitigated by altering the neutralization level of the reaction solution prior to the onset of gelation and solidification These adjustments to the neutralization as well as the application of the hydrocarbon coating previously mentioned were both observed to reduce the amount of polymer leakage in the poly (ethylene glycol) -1000 samples. As expected, the polytetrehydrofuran with a molecular weight of 2000 kg/mol was observed to show negligible polymer leakage.

5.5.4 Enthalpy of melting in phase change materials

To determine the potential of shape stabilized phase change materials for use as thermal storage devices in buildings the amount of heat stored, dissipated, and material cost of the device must be quantified. These values were elicited using differential scanning calorimetry to measure the enthalpy of melting for poly (ethylene glycol) -based materials with respect to the amount of material being analysed. Additionally, these materials would be incorporated in the finite spaces of building cavities; therefore, the volumetric enthalpy of melting is also necessary. The enthalpy of the different poly (ethylene glycol) -based materials and polytetrehydrofuran with a molecular weight of 2000 kg/mol is presented in Table 3. As previously mentioned polytetrehydrofuran with a molecular weight of 2000 kg/mol exhibited exceptional moisture resistance but its enthalpy of melting is well below the that of all poly (ethylene glycol) -based systems. Additionally, considering this metric along with this material's low thermal conductivity and materials cost, polytetrehydrofuran with a molecular weight of 2000 kg/mol is currently unfeasible for real world applications. In contrast poly (ethylene glycol) -based PCMS exhibited the largest enthalpy of melting and thus were determined to be the most ideal material for surface functionalization with

Table 3 Summarized enthalpy of melting for select polymers and corresponding shape stabilized phase change materials (ssPCMs).

PCM	ΔH_m (J/g)	ΔH_m (kWh/m^3)
poly (ethylene glycol) 600	116.9	36.5
ssPCM poly (ethylene glycol) 600	58.9	18.4
ssPCM poly (ethylene glycol) 600 (Dilute base)	54.6	17.1
poly (ethylene glycol) 1000	140.6	46.9
ssPCM poly (ethylene glycol) 1000 (Dilute base)	92.7	30.9
PTHF2000	83.2	22.5
ssPCM PTHF2000	64.2	17.3

hydrophobic hydrocarbon groups to address water uptake and boron nitride filling to boost its thermal conductivity.

5.5.5 Thermal Conductivity of boron nitride Composites

Reducing the undercooling needed to change the phase of the materials evaluated in this thesis is necessary to increase the coefficient of performance. It was demonstrated that this can be done while simultaneously increasing the thermal conductivity of the phase change materials by incorporating particles possessing a high thermal conductivity that can also serve as nucleation sites during crystallization. The low thermal conductivities of polymers has been reported to be a primary hurdle for real world application of polymeric

phase change materials, therefore, investigating mechanisms to boost this thermal property is essential.[146] In our study poly(ethylene glycol) at1000 kg/mol was initially mixed with boron nitride to form a composite due to its high thermal conductivity and its ability to be functionalized with hydroxyl groups for improved mixing. This process was outlined previously in the synthesis section. Figure 44 shows the used exfoliated boron nitride sheets in literature and demonstrates significant increase in the thermal conductivity of PNIPAM and reduced crystallization temperature of polylactic acid. These feats were reported to be achieved at low loading fractions as the boron nitride acted as an effective conductive fillers and served as nucleation sites for crystal growth in these systems.[167, 168]

Boron nitride and boron nitride functionalized with hydroxyl groups were incorporated into poly (ethylene glycol) at 1000 kg/mol samples. In the unfunctionalized

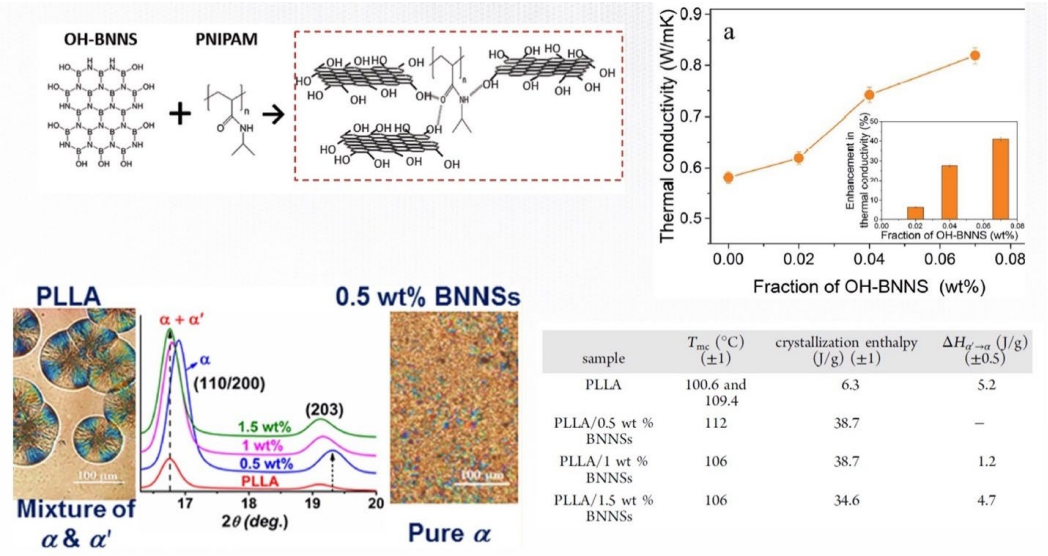

sample	T_{mc} (°C) (±1)	crystallization enthalpy (J/g) (±1)	$\Delta H_{\alpha'\to\alpha}$ (J/g) (±0.5)
PLLA	100.6 and 109.4	6.3	5.2
PLLA/0.5 wt % BNNSs	112	38.7	–
PLLA/1 wt % BNNSs	106	38.7	1.2
PLLA/1.5 wt % BNNSs	106	34.6	4.7

Figure 44 Literature reported effects of boron nitride hydroxide substitution (<1.5 wt%) in organic materials. (Top) Measured increase in thermal conductivity of PNIPAM.[167] (Bottom) Measured increase in crystallization enthalpy of PLLA [168].

state the material was simply mixed into the polymer solution in various quantities up to 25 wt%. In contrast exfoliated boron nitride incorporation into the phase change material was limited to 5 wt% because it increased the gelation rate significantly which caused the solution to solidify before casting and produced brittle samples with high surface roughness.

Although literature reports small loading of exfoliated boron nitride having large effects on the thermal properties of other polymer composite materials, it was observed to have a small effect in raising the thermal conductivity in poly (ethylene glycol) based samples. Figure 45 shows the thermal conductivity of poly (ethylene glycol) at 1000 kg/mol -boron nitride composites with different volume fractions of the inorganic filler. Notice that composites made with exfoliated boron nitride had a max loading fraction of

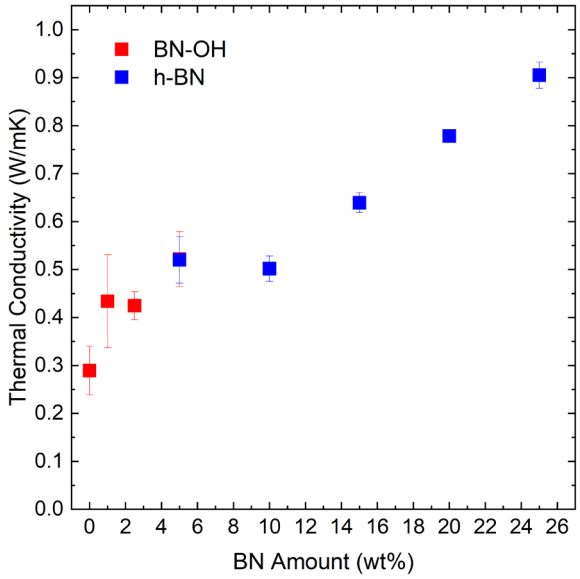

Figure 45 Thermal conductivity increases with BN loading in poly (ethylene glycol) 1000-based ssPCM. Substitution of functionalized BN-OH limited by compensating neutralization. Substitution of BN can reach 3x thermal conductivity target.

5% and at this value it was observed to increase the thermal conductivity of the phase change material from 0.29 $Wm^{-1}K^{-1}$ to 0.51 $Wm^{-1}K^{-1}$. This 79% increase is minor when considering the smaller wt% used in other polymer systems to achieve similar results. In contrast boron nitride was able to increase the thermal conductivity the composite by over 300% but a 25 wt% loading was required to achieve this feat. The incremental boost to the thermal conductivity of the material composite as function of boron nitride loading is linear after 10 wt% suggesting that this material property follows the rule of mixture.

5.5.6 Thermal conductivity of poly (ethylene glycol) series

The thermal conductivity of poly (ethylene glycol) possessing different molecular weights was investigated to elicit characteristics of increasing the length of the polymer chain. It was observed that each material absorbs water vapor at a similar rate and in relatively similar quantities. Figure 46 shows the raw and normalized time dependent thermal conductivity of poly (ethylene glycol) -with a molecular weights of 600, 800, and 1000 kg/mol as the material was exposed to 95% relative humidity. Poly (ethylene glycol) at1000 kg/mol had the second lowest thermal conductivity (0.28 $Wm^{-1}K^{-1}$) out of the evaluated series therefore as water vapor diffused into the structure the material experienced a boost in thermal conductivity. Poly (ethylene glycol) at 800 kg/mol was observed to have a slightly lower thermal conductivity (0.27 $Wm^{-1}K^{-1}$.) than the poly (ethylene glycol) at1000 kg/mol series but displayed a smooth and constant thermal

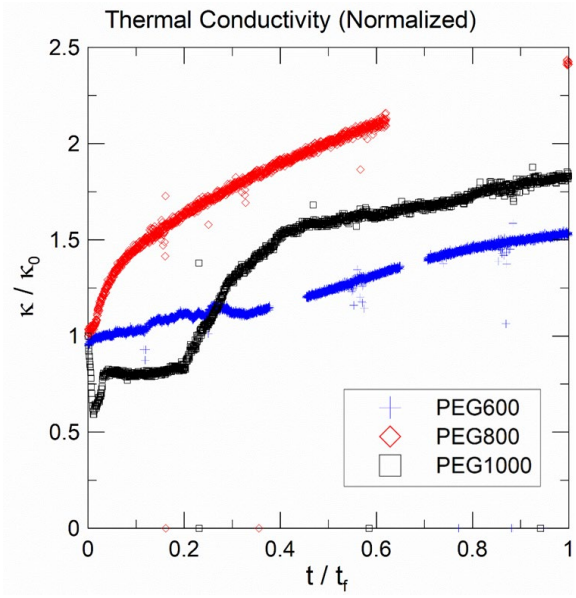

Figure 46 Normalized thermal conductivity measurements for polyethylene glycol exposed to humidity as a function of time.

conductivity increase in the presence of water vapor. Lastly poly (ethylene glycol) at 600 kg/mol possessed a thermal conductivity nearly 180% higher than the other materials measured. Its change in thermal conductivity was observed to have the flattest slope which is believed to result from the polymer having a thermal conductivity value closer to the water vapor infiltrating its structure.

5.5.7 Thermal dynamic analysis summery

A thermodynamic system analysis was completed by Dr. Mike Adams to examine the thermal storage potential of poly (ethylene glycol) at1000 kg/mol in building structures. In the analysis the specific cost per kWh as a function of the materials storage capability was presented. It is important to note that the total thermal storage capacity was previously described as the enthalpy of melting in these poly (ethylene glycol) based systems and that

the usable storage capacity of any mass is typically less than its heat capacitance. This is because the charge and discharge times in these materials maybe faster than the time it takes to fully charge or discharge the system resulting in unused heat storage or heat discharge potential. Additionally, increasing the thermal conductivity of the materials allows for greater usable storage capacity because it would increase the rate of heat flow within the material. Equation 24 shows the components of poly (ethylene glycol) at1000 kg/mol systems used as thermal battery and provide a method to analyze and optimize specific cost of the material which is defined as the total cost per kWh.

$$specific\ cost\ \left[\frac{\$}{kWh}\right] = \frac{Cost}{Usable\ Storage\ Capacity} = \frac{Cost}{\xi * V * u} \tag{24}$$

In this equation the ratio of usable phase change material volume (ξ), is multiplied by the total material volume (V) and energy density (u) of the material. A graphic of these components is provided in Figure 47 and illustrates the relationship the material's volume, usable storage ratio, and length. It is clear from the image Figure 47a that as the volume is increased (denoted by the large L_{PCM}) that the usable storage ratio is decreased as result of the material that did not undergo a phase change at the end of a melting cycle. Instead, there is a critical length, seen in Figure 47b, where the phase change material completely changes its phase at the end of a melting cycle which leaves only the sensible heat component of the system unused and results from moderate material volumes and energy density values. The last case shown in Figure 47c depicts phase change materials with small volumes. In this scenario the only amount of heat is needed to completely change the phase of the material, meaning there will be a very small amount of sensible heat remaining.

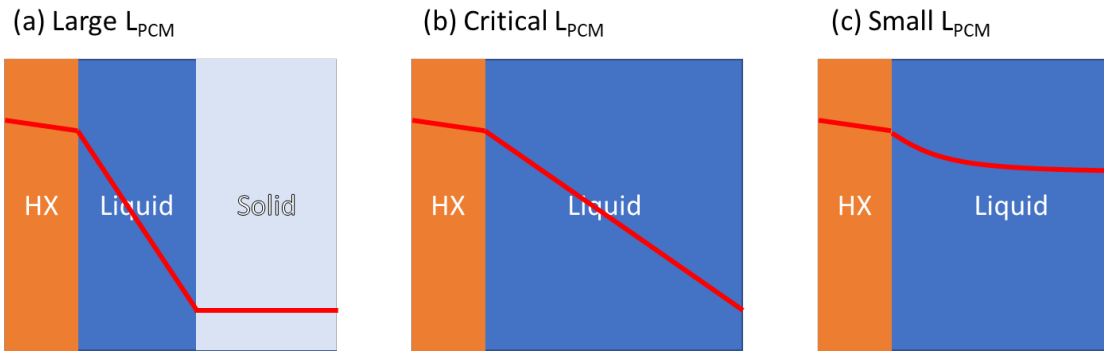

Figure 47 Qualitative depiction of temperature distribution (red line) in PCM thermal battery at end of discharge cycle. Not drawn to scale. (a) PCM length is large and phase change is incomplete. Small usable storage ratio and large PCM volume. (b) PCM length is just long enough for complete phase change, but sensible heat remains. Moderate usable storage ratio and PCM volume. (c) PCM length is short and very little sensible heat remains. Large usable storage ratio and small PCM volume.

The shape stabilized phase change material made from poly (ethylene glycol) at1000 kg/mol is limited the materials by low thermal conductivity which directly correlates to its utilization factor. By increasing the thermal conductivity of these materials, the price of the PCM can be improved by a factor of η, as more of the material would be used for heat storage and dissipation.

5.6 Summary

Shape stabilized poly (ethylene glycol) based materials were analyzed to investigate their ability to be used as thermal storage devices in buildings. These materials utilize latent heat that can be stored or released during a phase transition to offset the energy required for space heating and cooling. Specifically, the engineering hurdles of material deformation and low thermal conductivity were addressed in this chapter. Alternative chemistries which aimed to change the hydrophobicity of the poly (ethylene glycol)

material were investigated but were found to have minor effects on water uptake compared to the uncoated phase change materials. However, poly (ethylene glycol) at1000 kg/mol that was functionalized with hydrocarbon coatings were shown to maintain more of their mass after the initial humidity cycle. Polymer leakage remains a problem in these systems but can be significantly reduced by changing the neutralization of the solution towards the end of fabrication. Additionally, polytetrehydrofuran with a molecular weight of 2000 kg/mol was evaluated as a hydrophobic substitute for poly (ethylene glycol) based phase change materials. Although the material exhibited outstanding water uptake properties, polytetrahydrofuran's enthalpy of melting was well below that of poly (ethylene glycol) at1000 kg/mol, which was shown to have the highest enthalpy of melting among the poly (ethylene glycol) series. To this end poly (ethylene glycol) at 1000 kg/mol was used as the based material for addressing the low thermal conductivity of these materials.

Increasing the thermal conductivity of the shape stabilized phase change materials was demonstrated by incorporating boron nitride and exfoliated boron nitride-hydroxyl nano sheets as fillers into the polymer matrix in various quantities. In general bulk boron nitride has a high thermal conductivity (484 $Wm^{-1}K^{-1}$) making it ideal for increasing the thermal conductivity of the polymer composite. It was observed that the exfoliated boron nitride-hydroxyl caused the poly (ethylene glycol) material to gelate rapidly even in small quantities, therefore, only a 5 wt% loading could be achieved. This 5% loading increased the thermal conductivity of the system by 79%. In contrast, boron nitride particles were loaded into the poly (ethylene glycol) at 1000 kg/mol system in quantities up to 25 wt% and corresponded to a 300% increase in the thermal conductivity of the phase change material. Although this improvement is a step in the right direction for phase change

materials for used as heat storage in building envelopes, the combination of poly (ethylene glycol) based materials latent heat values, low thermal conductivity and materials cost currently make its immediate incorporation into building structures energetically unfeasible.

CHAPTER 6. FUTURE OUTLOOK

6.1 Thesis Outlook

6.1.1 Hollow silica nano particle insulation recap

In this thesis the optimal shell to pore size ratio of silica nano particles used for thermal insulation applications was identified to be 10nm and 350 nm respectively. Hollow particles with optimal geometric features were fabricated by controlling synthesis parameters such as the temperature of the solution used to make the sacrificial polymer template and by controlling the amount of silica precursor needed to modulate the thickness of the shell. Incorporating nano sized carbon black particles into the matrix of the hollow particle system was shown to reduce the effective thermal conductivity of the system by 22%. It is believed that this drop in the effective thermal conductivity results from a combination radiative absorption and an increase in interfacial thermal resistance. Although hollow silica nanoparticle systems were shown to have comparable thermal conductivities to that of super-insulating aerogels, lowering the thermal conductivity of these systems even more remains an important aspect of developing these types of nano insulation materials.

6.1.2 Polymeric distributed Bragg reflectors recap

Polymeric distributed Bragg reflectors were demonstrated to be viable candidates for use as photonic mirrors capable of selectively reflecting wavelengths of thermal radiation. Due to the dynamic properties of polymers, post processing alterations to the microstructure were leveraged to tune the reflective response of the mirror. Specifically,

the polymer's ability to swell when exposed to a good solvent was leveraged to disrupt the constructive interference needed to reflect thermal radiation over a particular band width. This swelling phenomenon occurred in the high index hybrid layers that were composed of PVA, and various amount of a titania based crosslinking species.

More interestingly, thermal switching was demonstrated in the hybrid material and elicited novel information about the role of the inorganic material. With the Flory-Rehner model for polymer swelling it was shown that increasing the content of the TiO_x crosslinker decreased the swelling capability of the film. As this loading fraction was pushed further than 50% GIWAXS data was shown confirming the presence of titania peaks suggesting that the crosslinker formed polynuclear clusters in between polymer chains.

6.1.3 Phase change materials for thermal storage recap

Phase change materials made from poly (ethylene glycol) and polytetrehydrofuran with a molecular weight of 2000 kg/mol were used to investigate the material's potential for used as shape stabilized thermal batteries. Samples of poly (ethylene glycol) were tested at various molecular weight (600, 800, and 1000 kg//mol) and were subjected to processing steps designed to reduce the hydrophobicity of the polymer. The storage capacity of the materials was determined by measuring the respective enthalpy of melting. In assessing the enthalpy values of the poly (ethylene glycol) based materials it was obvious that the poly (ethylene glycol) -at 1000 kg/mol possessed the greatest capacity to be used as a phase change material for thermal storage and therefore was used in the subsequent experiments regarding water uptake. It is important to note that these materials suffer from having low thermal conductivities, a metric which directly correlates to the phase change materials

ability to transfer or store heat efficiently. Although poly (ethylene glycol) -at 1000 kg/mol had the highest measured enthalpy it also was measured to have a thermal conductivity nearly twice as small as the poly (ethylene glycol) -600, however, poly (ethylene glycol) -600 excessive water uptake and low enthalpy made it an unviable material for use as a thermal storage material.

Poly (ethylene glycol) -at 1000 kg/mol was used to investigate processing methods hypothesized to increase the hydrophobicity of the shape stabilized phase change material. Hydrophilic hydrocarbons were chemically added to the surface of the material to reduce the terminal hydroxyl bonds. This was found to help maintain the structural integrity of the poly (ethylene glycol) -at 1000 kg/mol but ultimately it did not slow down the rate of moisture absorption until after 24 hours. The thermal conductivity of the material increased with the addition of boron nitride fillers. These fillers were incorporated in the matrix of the poly (ethylene glycol) -at 1000 kg/mol in two different forms, boron nitride and boron nitride-hydroxyl, to investigate their influence on the thermal conductivity of the composite material. Ultimately the exfoliated boron nitride-hydroxyl was found to induce gelation and only 5 wt% could be incorporated in the polymer. Next, boron nitride particles were used to increase the thermal conductivity of the film by 300%. However, it is important to note that this feat was achieved with a 25 wt% loading of boron nitride. In all poly (ethylene glycol) based phase change materials latent heat values, low thermal conductivity and materials cost require more improvement for it to become energetically feasible for use as thermal batteries in building.

6.2 Future direction for hollow silica nanoparticles

6.2.1 Shell substitution

The shell of the hollow silica nanoparticles has been identified as the primary contributor to the effective thermal conductivity in these systems and is referred to as the solid contribution. To lower the solid contribution the shells of these hollow particles could be made from polymer composites that have inherently lower thermal conductivities rather than ceramic shells. Numerous fabrication techniques to create hollow polymer particles such as soap free emulsion, dispersion, and distillation suspension have been reported in several comprehensive reviews.[169, 170] Although, these materials have been reported on since the early 1980's there are very few studies which dive into the potential of hollow polymer nanoparticles as thermal insulation materials in buildings, making this an intriguing new area of exploration.

6.2.2 Packaging and scaling research

Encapsulating loose packed silica nanoparticles will be a critical next step to bring this insulation material to market. Nanoparticles can have unforeseen impacts on human health upon exposure to large quantities over time. Silicosis is a documented ailment which stems directly from over exposure to silica and has been documented as early as the 1970's. Specifically, it is a fibrotic lung disease that is brought on through inhaling silicon dioxide. Its symptoms range from dyspnea, chromic dry cough, and in extreme causes respiratory failure.[171-173] Therefore, it is imperative that these low density hollow particles be packaged well inside panels for use as insulation. Engineering perforation resistant, low thermal conductivity encapsulation material will be the next big engineering task needed to bring these nano insulation materials to market.

Improved yield from iterative fabrication of hollow particles was demonstrated in chapter one but optimizing this process will be essential to produce hollow silica nanoparticles at market scale. Currently, the iterative method has shown that the solution needed to make hollow silica nanoparticles can be recycles by filtering out silica particulates and readjusting the chemistry of the solution. Adversely, it was observed that the shell thickness increased after every iteration, which indicated that there was residual unreacted tetraethyl orthosilicate in the reaction mixture. Future research done on the solution mixture after batch producing needs to focus on understanding synthesis chemistries and parameters that are most important for reproducing hollow silica nanoparticles with consistent geometrical properties.

6.2.3 Predictive models for hollow silica nanoparticles

The current equivalence model which considers the effects of contact resistance was observed to better predict the effective thermal conductivity of hollow nanoparticle foams. As shown in the experimental data, increasing the number of interfaces using small 10 nm carbon black particles significantly reduced the effective thermal conductivity of system by 20%. This reduction occurred as result of increased thermal interface resistance also due to the absorption of thermal radiation. Like silica aerogels hollow silica nanoparticles have been reported to be highly transparent to visible and NIR light. Therefore, predictive models which take geometrical parameters, interfacial thermal resistance, and radiative absorption into account can be used to better design ternary hollow silica nanoparticle systems for thermal insulation in building.

6.3 Future direction for polymeric distributed Bragg reflectors

6.3.1 Inorganic fillers

To discuss the future of polymeric distributed Bragg reflectors the nature of these materials must be put into context before they can be considered in real world applications. Figure 48 shows the solar irradiance distribution from 250 to 2500 nm. Notice that over 58% of the total amount of thermal energy dissipated by the sun occurs over the UV and near IR wavelength making tunable distributed Bragg reflectors ideal for reflection in these regions.[174] However, the reflective properties still require widening the refractive index contrast between bilayers using inorganic fillers. This effect is limited by the dielectric properties of the filler material and is critical to increase the bandwidth of the photonic stop band. As seen in figure 34 the highest refractive index value achieved was 2.1 with a loading volume of 80% titania hydrate and corresponds to a refractive index difference of .61 compared to the low index polymer. Furthermore, the distributed Bragg reflectors

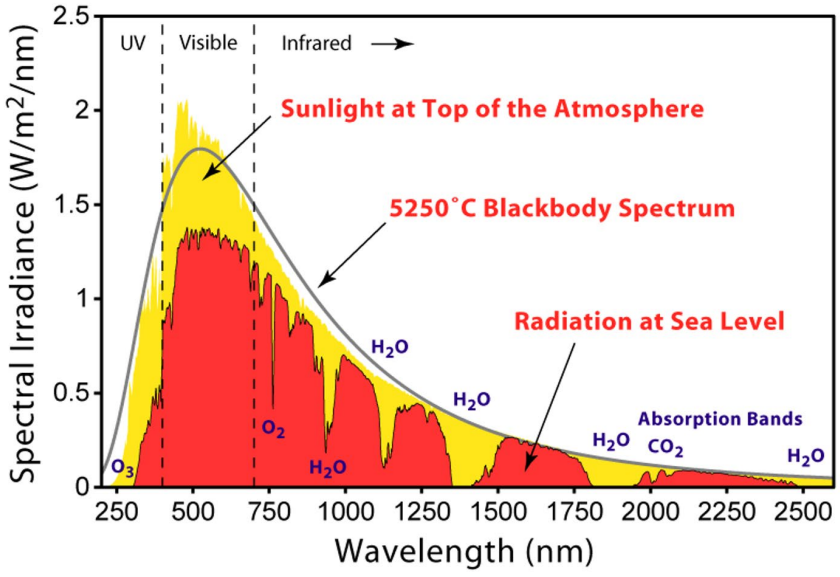

Figure 48 Solar irradiance distribution from 250 to 2500 nm wavelengths at the top of the atmosphere and at sea level. [174]

presented had a refractive index difference of 0.3-0.4, which is significantly higher than the original contrast between the PMMA and PVA (.02), but as we see in figure 34 this contrast is not enough to achieve 100% reflection. Increasing the refractive index contrast is no trivial task but is currently being done by incorporating other inorganic filler such as silicon nanoparticles which have a refractive index of 3.49.[175] This inorganic material has higher dielectric properties than the TiO_x species used to fabricate our hybrid structures and should be considered as an option to increase the contrast between bilayers in order to stretch the band width and total reflection of the photonic band gap.

6.3.2 Increasing number of layers

Another way to increase the reflective properties is by simply increasing the number of bilayers used to create the DBR stack. As shown in equation 11 increasing the number of bilayers produces well defined phonic bang gap edges and nearly 100% reflection along the designated wavelength. However, increasing the number of bilayers increases the fabrication time and introduces processing risk associated with the changes in the polymer solutions viscosity, density, and surface tension that result from solvent evaporating. This problem offers a unique opportunity for solution chemist to identify and demonstrate viable parameters to ensure the polymer solutions maintain the necessary properties needed to create uniform layers. It was shown that the more responsive 16.5 bilayer distributed Bragg reflectors made with PVA hybrids containing 30% TiO_x had a weaker reflectance than those made with 60% of the inorganic filler. Therefore, to boost the reflection in more responsive polymeric distributed Bragg reflectors, understanding how to combat the in-situ changes to the solution will be critical to apply additional uniform bilayers.

6.3.3 Chirped structures

Another area widely available for exploration is non-quarter wavelength chirped mirrors for use in thermal management applications. These types of dielectric mirrors consist of bilayer sequences with different thicknesses. Unlike distributed Bragg reflectors made using quarter wavelength conditions that only reflect one wave range, the staggered bilayer structure of chirped mirrors allow for the reflection of a variable wavelength ranges making them an attractive for reflecting over a large bandwidth. As light propagates through these structures the different sequences of bilayers reflect different wavelengths causing a larger wave range to be reflected. Figure 49 shows the reflectance spectra of 32.5 bilayers chirped mirror spanning 400 to 1400 nm. Notice the photonic stop band ranges from 800 to 1300 nm and reaches a peak reflectance of 84%. To put this in perspective this

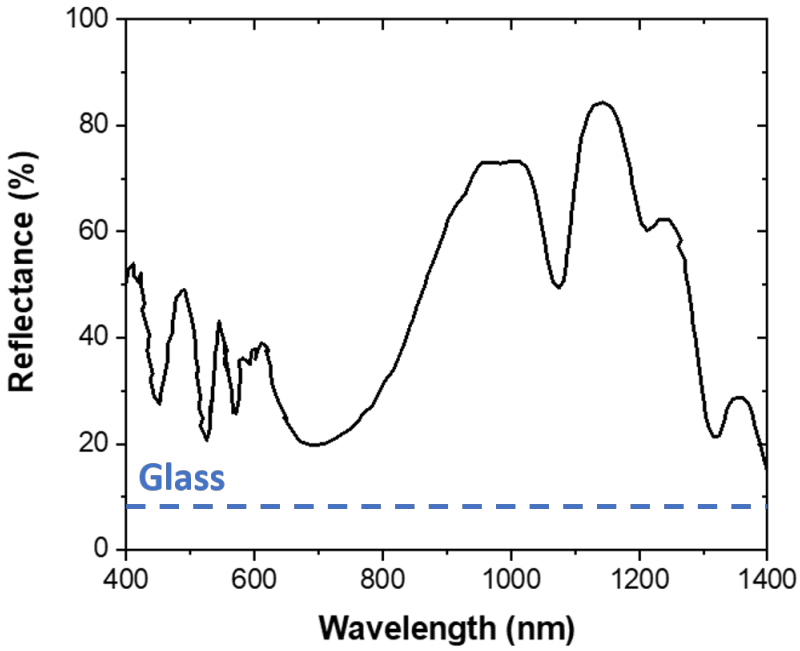

Figure 49 Reflectance spectrum of a DBR made with 32.5 bilayers of PMMA and PVA-TiO_x hybrid material with staggered pairs of layer thickness.

photonic band gap could reflect nearly 20% of all incoming solar radiation. Additionally, the secondary and ternary peaks associated with higher reflection observed at shorter wavelengths are suppressed in chirped structures. This is hypothesized to result from inherent antireflective characteristic within the material that obstruct the conditions needed to achieve higher order constructive interference. It is important to note that these materials were deposited on glass substrates that were measured to have an 8% optical loss due to absorption. This is represented by the blue dashed line in figure 49. These primary results encourage future modeling and experimental studies into the use of chirped structures to reflect wide bandwidths of thermal radiation over the UV and NIR wavelengths.

REFERENCES

1. Glenk, G., R. Meier, and S.J.A.a.S. Reichelstein, *Clean energy technologies: Dynamics of cost and price.* 2021.

2. Lindsey, R. and L.J.C.g. Dahlman, *Climate change: Global temperature.* 2020. **16**.

3. McMichael, A.J. and A.J.B. Haines, *Global climate change: the potential effects on health.* 1997. **315**(7111): p. 805-809.

4. Schneider, S.H.J.N., *What is' dangerous' climate change?* 2001. **411**(6833): p. 17-19.

5. Cheung, W.W., G. Reygondeau, and T.L.J.S. Frölicher, *Large benefits to marine fisheries of meeting the 1.5 C global warming target.* 2016. **354**(6319): p. 1591-1594.

6. Szaboova, L., *Concepts, Contexts and Categorisations of Climate Mobility.*

7. Hardowar, S.J.R.j.d.l.O.I., *Academia and Climate Justice: Opportunities and Challenges.* 2021(31).

8. McEldowney, J.F. and J.L. Drolet, *Climate change and refugees*, in *The Impacts of Climate Change*. 2021, Elsevier. p. 537-545.

9. Ali, S.S.S., et al., *Critical determinants of household electricity consumption in a rapidly growing city.* 2021. **13**(8): p. 4441.

10. Heleniak, T.J.P.G., *The future of the Arctic populations.* 2021. **44**(2): p. 136-152.

11. Anisovich, A. and P. Tsarik, *Agricultural trends of the global economy.* 2021.

12. Salhofer, S., et al., *Plastic recycling practices in vietnam and related hazards for health and the environment.* 2021. **18**(8): p. 4203.

13. Tang, Q. and M. Li. *Analysis of Cambodia's macroeconomic development*. in *E3S Web of Conferences*. 2021. EDP Sciences.

14. Islam, M.A., et al., *Fourth industrial revolution in developing countries: a case on Bangladesh.* 2018. **21**(1).

15. Cai, Y. and W.J.A.R.o.S. Feng, *The Social and Sociological Consequences of China's One-Child Policy.* 2021. **47**: p. 587-606.

16. Zhongming, Z., et al., *International Energy Outlook 2019 projects nearly 50% increase in world energy usage by 2050, led by growth in Asia.* 2019.

17. Ghazali, F., A.H. Ansari, and R.J.U.J.o.L.S. Karim, *A comparative study on legal frameworks on renewable energy in Malaysia and India: Towards the commitments under the Paris agreement.* 2021. **12**(1): p. 93-118.

18. Chen, Y. and Y.J.A.i.C.C.R. Xin, *Implications of geoengineering under the 1.5 C target: Analysis and policy suggestions.* 2017. **8**(2): p. 123-129.

19. Elkahwagy, R., V. Gyanchandani, and D. Piselli, *UNFCCC nationally determined contributions*. 2017, The Graduate Institute of International and Development Studies, Centre for ….

20. Reinman, S.L.J.R.R., *Intergovernmental panel on climate change (IPCC).* 2012.

21. Chastas, P., et al., *Normalising and assessing carbon emissions in the building sector: A review on the embodied CO2 emissions of residential buildings.* 2018. **130**: p. 212-226.

22. Eveloy, V. and D.S.J.E. Ayou, *Sustainable district cooling systems: Status, challenges, and future opportunities, with emphasis on cooling-dominated regions.* 2019. **12**(2): p. 235.

23. Dong, Y., et al., *Greenhouse Gas Emissions from Air Conditioning and Refrigeration Service Expansion in Developing Countries.* 2021. **46**: p. 59-83.

24. Ospina, C.J.C.I.N.Y., *Cooling Your Home but Warming the Planet: How We Can Stop Air Conditioning from Worsening Climate Change.* 2018: p. 9.

25. Ascione, F., et al., *Solar gain and building envelope: the surface factor.* 2010. **38**(2): p. 187-205.

26. Lam, J.C., et al., *Residential building envelope heat gain and cooling energy requirements.* 2005. **30**(7): p. 933-951.

27. Najjar, M.K., et al., *A framework to estimate heat energy loss in building operation.* 2019. **235**: p. 789-800.

28. Keener, J.P., S. Sircar, and A.L.J.P.R.E. Fogelson, *Influence of the standard free energy on swelling kinetics of gels.* 2011. **83**(4): p. 041802.

29. Kosny, J., A.J.J.o.T.I. Desjarlais, and B. Envelopes, *Influence of architectural details on the overall thermal performance of residential wall systems.* 1994. **18**(1): p. 53-69.

30. Highfield, D. and C. Gorse, *Refurbishment and upgrading of buildings*. 2009: Spon Press.

31. Al-Obaidi, K.M., M. Ismail, and A.M.A.J.F.o.A.R. Rahman, *Passive cooling techniques through reflective and radiative roofs in tropical houses in Southeast Asia: A literature review.* 2014. **3**(3): p. 283-297.

32. Tong, S., H.J.B. Li, and Environment, *An efficient model development and experimental study for the heat transfer in naturally ventilated inclined roofs.* 2014. **81**: p. 296-308.

33. Fält, M., R.J.J.o.E. Zevenhoven, and P. Engineering, *Radiative cooling in northern Europe using a skylight.* 2011. **5**(8).

34. Fält, M., R.J.J.o.E. Zevenhoven, and P. Engineering, *Combining the radiative, conductive and convective heat flows in and around a skylight.* 2012. **6**(9): p. 1423-1428.

35. Bournas, D.A.J.C.P.B.E., *Concurrent seismic and energy retrofitting of RC and masonry building envelopes using inorganic textile-based composites combined with insulation materials: A new concept.* 2018. **148**: p. 166-179.

36. Jelle, B.P.J.E. and buildings, *Traditional, state-of-the-art and future thermal building insulation materials and solutions–Properties, requirements and possibilities.* 2011. **43**(10): p. 2549-2563.

37. Sadineni, S.B., et al., *Passive building energy savings: A review of building envelope components.* 2011. **15**(8): p. 3617-3631.

38. Chen, J. and L.J.J.o.B.E. Lu, *Comprehensive evaluation of thermal and energy performance of radiative roof cooling in buildings.* 2021. **33**: p. 101631.

39. Farhan, S.A., et al., *Effect of roof tile colour on heat conduction transfer, roof-top surface temperature and cooling load in modern residential buildings under the tropical climate of Malaysia.* 2021. **13**(9): p. 4665.

40. Li, X., et al., *Ultrawhite BaSO4 paints and films for remarkable daytime subambient radiative cooling.* 2021. **13**(18): p. 21733-21739.

41. Norris, N., M. Lawton, and P. Roppel. *The concept of linear and point transmittance and its value in dealing with thermal bridges in building enclosures*. in *Building enclosure science & technology conference*. 2012.

42. Notario, B., et al., *Experimental validation of the Knudsen effect in nanocellular polymeric foams.* 2015. **56**: p. 57-67.

43. Lu, X., et al., *Correlation between structure and thermal conductivity of organic aerogels.* 1995. **188**(3): p. 226-234.

44. Aditya, L., et al., *A review on insulation materials for energy conservation in buildings.* 2017. **73**: p. 1352-1365.

45. Fuji, M. and C. Takai, *Superior thermal insulation film with transparency achieved by hollow silica nanoparticles*, in *Nanoparticle technology handbook*. 2018, Elsevier. p. 493-497.

46. Mofid, S.A., et al., *Utilization of size-tunable hollow silica nanospheres for building thermal insulation applications.* 2020. **31**: p. 101336.

47. Ashhar, M.Z.M. and L.C.J.J.o.B.E. Haw, *Recent research and development on the use of reflective technology in buildings–A review.* 2022. **45**: p. 103552.

48. *How much heat is lost through the roof?* 2021, January 21 [cited 2022 March 18]; Available from: https://www.homelogic.co.uk/how-much-heat-is-lost-through-the-roof#:~:text=Give%20or%20take%2C%20about%2025,will%20disappear%20through%20the%20floor.

49. Ferreira, M., H.J.E. Corvacho, and Buildings, *The effect of the use of radiant barriers in building roofs on summer comfort conditions–A case study.* 2018. **176**: p. 163-178.

50. Shopsowitz, K.E., et al., *Free-standing mesoporous silica films with tunable chiral nematic structures.* 2010. **468**(7322): p. 422-425.

51. Wang, S., et al., *Thermochromic smart windows with highly regulated radiative cooling and solar transmission.* 2021. **89**: p. 106440.

52. Spence, D., et al., *Hollow Silica Particles: A Novel Strategy for Cost Reduction.* 2021. **11**(6): p. 1627.

53. Nandiyanto, A.B.D., et al., *Mesopore-free hollow silica particles with controllable diameter and shell thickness via additive-free synthesis.* 2012. **28**(23): p. 8616-8624.

54. Liao, Y., et al., *Thermal conductivity of powder silica hollow spheres.* 2011. **526**(1-2): p. 178-184.

55. Wu, X., et al., *Raspberry-like silica hollow spheres: Hierarchical structures by dual latex− surfactant templating route.* 2007. **111**(27): p. 9704-9708.

56. Ernawati, L., et al., *Hollow silica as an optically transparent and thermally insulating polymer additive.* 2016. **32**(1): p. 338-345.

57. Liao, Y., et al., *Composite thin film of silica hollow spheres and waterborne polyurethane: Excellent thermal insulation and light transmission performances.* 2012. **133**(2-3): p. 642-648.

58. Sun, Q., et al., *The formation of well-defined hollow silica spheres with multilamellar shell structure.* 2003. **15**(13): p. 1097-1100.

59. Jia, Z., et al., *Prediction of the effective thermal conductivity of hollow sphere foams.* 2018. **1**(3): p. 1146-1157.

60. Ruckdeschel, P., A. Philipp, and M.J.A.F.M. Retsch, *Understanding thermal insulation in porous, particulate materials.* 2017. **27**(38): p. 1702256.

61. Sharma, J., et al., *Hybrid hollow silica particles: Synthesis and comparison of properties with pristine particles.* 2020. **10**(38): p. 22331-22334.

62. Nan, C.-W., et al., *Effective thermal conductivity of particulate composites with interfacial thermal resistance.* 1997. **81**(10): p. 6692-6699.

63. Jabbari, F., et al., *Effect of water/carbon interaction strength on interfacial thermal resistance and the surrounding molecular nanolayer of CNT and graphene flake.* 2019. **282**: p. 197-204.

64. Liu, H., et al., *Effective thermal conductivity modeling of hollow nanosphere packing structures.* 2020. **161**: p. 120298.

65. Warzoha, R.J., et al., *Engineering interfaces in carbon nanostructured mats for the creation of energy efficient thermal interface materials.* 2013. **61**: p. 441-457.

66. Ng, S., et al., *Hollow silica nanospheres as thermal insulation materials for construction: Impact of their morphologies as a function of synthesis pathways and starting materials.* 2018. **166**: p. 72-80.

67. Hu, F., S. Wu, and Y.J.A.M. Sun, *Hollow-structured materials for thermal insulation.* 2019. **31**(38): p. 1801001.

68. Zhu, C.-Y., et al., *Design and optimization of core/shell structures as highly efficient opacifiers for silica aerogels as high-temperature thermal insulation.* 2018. **133**: p. 206-215.

69. Neuhöfer, A.M., et al., *High-Temperature Thermal Transport in Porous Silica Materials: Direct Observation of a Switch from Conduction to Radiation.* 2021: p. 2108370.

70. Rao, A.V.J.J.o.S.-G.S. and Technology, *Elastic superhydrophobic and water glass-based silica aerogels and applications.* 2019. **90**(1): p. 28-54.

71. Han, D., et al., *Thermal properties of carbon black aqueous nanofluids for solar absorption.* 2011. **6**(1): p. 1-7.

72. Sharma, J. and G.J.N. Polizos, *Hollow silica particles: recent progress and future perspectives.* 2020. **10**(8): p. 1599.

73. Li, W. and D. Zhao, *Extension of the Stöber method to construct mesoporous SiO2 and TiO2 shells for uniform multifunctional core–shell structures*. 2013, Wiley Online Library.

74. Shekhawat, M., S. Tak, and R. Mangal. *The Transient Plane Source Technique to Measure Thermal Conductivity of Clays of Bikaner Region*. in *International Journal of Modern Physics: Conference Series*. 2013. World Scientific.

75. Yildiz, G. and M.E.J.T.v. Yahia, *Comparative performance evaluation of conventional and renewable thermal insulation materials used in building envelops.* 2020. **27**(1): p. 283-289.

76. Takai, C., et al., *Determine apparent shell density for evaluation of hollow silica nanoparticle.* 2012. **404**: p. 101-105.

77. Gao, T., et al., *Monodisperse hollow silica nanospheres for nano insulation materials: synthesis, characterization, and life cycle assessment.* 2013. **5**(3): p. 761-767.

78. Batmunkh, M., et al., *Thermal conductivity of TiO2 nanoparticles based aqueous nanofluids with an addition of a modified silver particle.* 2014. **53**(20): p. 8445-8451.

79. Stazi, F., et al., *Assessment of the actual hygrothermal performance of glass mineral wool insulation applied 25 years ago in masonry cavity walls.* 2014. **68**: p. 292-304.

80. Rasines, G., et al., *Mesoporous carbon black-aerogel composites with optimized properties for the electro-assisted removal of sodium chloride from brackish water.* 2015. **741**: p. 42-50.

81. Khizhnyak, P., A. Chechetkin, and A.J.J.o.e.p. Glybin, *Thermal conductivity of carbon black.* 1979. **37**(3): p. 1073-1075.

82. Reim, M., et al., *Silica-aerogel granulate–Structural, optical and thermal properties.* 2004. **350**: p. 358-363.

83. Caps, R. and J.J.S.E. Fricke, *Infrared radiative heat transfer in highly transparent silica aerogel.* 1986. **36**(4): p. 361-364.

84. Lu, X., et al., *Thermal transport in organic and opacified silica monolithic aerogels.* 1992. **145**: p. 207-210.

85. Victoria, S., *Energy Smart Housing Manual, Chapter 7: Insulation*. 2010.

86. Lean, J.J.S., *Contribution of ultraviolet irradiance variations to changes in the sun's total irradiance.* 1989. **244**(4901): p. 197-200.

87. Yang, M.Q., et al., *Disorder engineering in monolayer nanosheets enabling photothermic catalysis for full solar spectrum (250–2500 nm) harvesting.* 2019. **58**(10): p. 3077-3081.

88. Arasteh, D., J. Apte, and Y.J.A.t. Huang, *Future advanced windows for zero-energy homes.* 2003. **109**(2): p. 871-882.

89. Lin, S., et al., *Direct spray-coating of highly robust and transparent Ag nanowires for energy saving windows.* 2019. **62**: p. 111-116.

90. Bachevillier, S., *Solution-processed photonics for light and heat management*. 2018, Imperial College London.

91. Bachevillier, S., et al., *Fully Solution-Processed Photonic Structures from Inorganic/Organic Molecular Hybrid Materials and Commodity Polymers.* 2019. **29**(21): p. 1808152.

92. Wu, C.-J., et al., *Enhancement of bandwidth in a chirped quarter-wave dielectric mirror.* 2009. **23**(4): p. 437-447.

93. Orfanidis, S.J., *Electromagnetic waves and antennas.* 2002.

94. Lova, P., et al., *Polymer distributed bragg reflectors for vapor sensing.* 2015. **2**(4): p. 537-543.

95. Chen, A.X., et al., *Beyond stretchability: Strength, toughness, and elastic range in semiconducting polymers.* 2020. **32**(18): p. 7582-7601.

96. Lova, P. and D. Comoretto. *Label-free vapor selectivity by polymer-inorganic composite photonic crystals sensors*. in *AIP Conference Proceedings*. 2018. AIP Publishing LLC.

97. Ellmers, C., et al. *Ultrafast dynamic response of strain-compensated (GaIn) As/Ga (PAs) microcavity lasers*. in *Vertical-Cavity Surface-Emitting Lasers III*. 1999. International Society for Optics and Photonics.

98. Lee, C.K., et al., *Solvent swelling activation of a mechanophore in a polymer network.* 2014. **47**(8): p. 2690-2694.

99. Hertle, Y., et al., *Responsive P (NIPAM-co-NtBAM) microgels: Flory–Rehner description of the swelling behaviour.* 2010. **288**(10): p. 1047-1059.

100. Algar, M.J.P.T., *Polymer science dictionary.* 1997. **3**(16): p. 299.

101. Jin, Y., et al., *Improvement of Swanepoel method for deriving the thickness and the optical properties of chalcogenide thin films.* 2017. **25**(1): p. 440-451.

102. Xu, L., et al., *Enhanced photon collection in luminescent solar concentrators with distributed Bragg reflectors.* 2016. **3**(2): p. 278-285.

103. Bahrami, A., S. Mohammadnejad, and N.J.J.C.P.B. Abkenar, *Modified-DBR-based semi-omnidirectional multilayer anti-reflection coating for tandem solar cells.* 2013. **23**(2): p. 028803.

104. Miura, K., et al. *Fabrication of polymer optical waveguides for the 1.5-μm band using focused proton beam*. in *Key Engineering Materials*. 2012. Trans Tech Publ.

105. Miao, Y., et al., *Relative humidity sensor based on tilted fiber Bragg grating with polyvinyl alcohol coating.* 2009. **21**(7): p. 441-443.

106. Darhuber, A.A., et al., *Selective dip-coating of chemically micropatterned surfaces.* 2000. **88**(9): p. 5119-5126.

107. Zhang, Z., et al., *Dip coating of cylinders with Newtonian fluids.* 2022. **607**: p. 502-513.

108. Brinker, C., et al., *Fundamentals of sol-gel dip coating.* 1991. **201**(1): p. 97-108.

109. Puetz, J., M.J.S.-g.t.f.g.p. Aegerter, and users, *Dip coating technique.* 2004: p. 37-48.

110. Vernon, R. and S.J.P.o.t.I. Seshadri, *Reflection coefficient and reflected power on a lossy transmission line.* 1969. **57**(1): p. 101-102.

111. Coates, N.E., et al., *Effect of interfacial properties on polymer–nanocrystal thermoelectric transport.* 2013. **25**(11): p. 1629-1633.

112. Kommandur, S. and S.J.R.o.S.I. Yee, *A suspended 3-omega technique to measure the anisotropic thermal conductivity of semiconducting polymers.* 2018. **89**(11): p. 114905.

113. Tong, T. and A.J.R.o.S.I. Majumdar, *Reexamining the 3-omega technique for thin film thermal characterization.* 2006. **77**(10): p. 104902.

114. Wang, H., M.J.I.J.o.H. Sen, and M. Transfer, *Analysis of the 3-omega method for thermal conductivity measurement.* 2009. **52**(7-8): p. 2102-2109.

115. De Haas, W., J. De Boer, and G.J.P. Van den Berg, *The electrical resistance of gold, copper and lead at low temperatures.* 1934. **1**(7-12): p. 1115-1124.

116. Sun, D., et al., *Sub-mA threshold 1.5-μm VCSELs with epitaxial and dielectric DBR mirrors.* 2003. **15**(12): p. 1677-1679.

117. Qiu, P., et al., *Fabrication and characterization of low-threshold single fundamental mode VCSELs with dielectric DBR mirror.* 2021. **13**(4): p. 1-6.

118. Butt, M.A., et al., *Modelling of multilayer dielectric filters based on TiO2/SiO2 and TiO2/MgF2 for fluorescence microscopy imaging.* 2016. **40**(5): p. 674-678.

119. Muhammad Zain, N., et al. *Influence of isocyanate structures on mechanical performance of aluminum bonded with green polyurethane adhesive*. in *Advanced Materials Research*. 2014. Trans Tech Publ.

120. Ferreira, J.A., et al., *A new look to non-Fickian diffusion.* 2015. **39**(1): p. 194-204.

121. Rehage, G., O. Ernst, and J.J.D.o.t.F.S. Fuhrmann, *Fickian and non-Fickian diffusion in high polymer systems.* 1970. **49**: p. 208-221.

122. Wood, J. and L.J.C.e.s. Gladden, *Modelling diffusion and reaction accompanied by capillary condensation using three-dimensional pore networks. Part 1. Fickian diffusion and pseudo-first-order reaction kinetics.* 2002. **57**(15): p. 3033-3045.

123. Yeo, T., et al., *Characterisation of a polymer-coated fibre Bragg grating sensor for relative humidity sensing.* 2005. **110**(1): p. 148-156.

124. Xia, C., et al., *Solvent-driven polymeric micro beam device.* 2010. **20**(8): p. 085030.

125. Flory, P.J.J.T.J.o.C.P., *Statistical mechanics of swelling of network structures.* 1950. **18**(1): p. 108-111.

126. Liu, Y. and P.H.J.J.o.A.S. Daum, *Relationship of refractive index to mass density and self-consistency of mixing rules for multicomponent mixtures like ambient aerosols.* 2008. **39**(11): p. 974-986.

127. Lu, X., et al., *Moisture–absorption, dielectric relaxation, and thermal conductivity studies of polymer composites.* 1998. **36**(13): p. 2259-2265.

128. Hummel, P., et al., *Thermal transport in ampholytic polymers: the role of hydrogen bonding and water uptake.* 2020. **53**(13): p. 5528-5537.

129. Oladele, I., et al., *Thermal and water absorption properties of bio-synthetic hybrid reinforced polypropylene composites.* 2021. **38**: p. 994-998.

130. Xu, Y., et al., *Nanostructured polymer films with metal-like thermal conductivity.* 2019. **10**(1): p. 1-8.

131. Barbosa, R., A.T. Nunes, and J.D.J.M.R. Ambrósio, *Devulcanization of natural rubber in composites with distinct crosslink densities by twin-screw extruder.* 2017. **20**: p. 77-83.

132. Pacios, I.E., et al., *Correlation of swelling and crosslinking density with the composition of the reacting mixture employed in radical crosslinking copolymerization.* 2007. **103**(1): p. 263-269.

133. Zhang, B., et al., *Preparation and characterization of carboxymethyl starch microgel with different crosslinking densities.* 2015. **124**: p. 245-253.

134. Iasilli, G., et al., *Luminescent solar concentrators: Boosted optical efficiency by polymer dielectric mirrors.* 2019. **3**(3): p. 429-436.

135. Giusto, P., et al., *Colorimetric detection of perfluorinated compounds by all-polymer photonic transducers.* 2018. **3**(7): p. 7517-7522.

136. Knarr III, R.J., et al., *In-plane anisotropic photoresponse in all-polymer planar microcavities.* 2016. **84**: p. 383-390.

137. Ma, Y., et al., *Fabrication of super-hydrophobic film from PMMA with intrinsic water contact angle below 90.* 2007. **48**(26): p. 7455-7460.

138. N'diaye, M., et al., *Water absorption of poly (methyl methacrylate) measured by vertical interference microscopy.* 2012. **28**(31): p. 11609-11614.

139. El Shafee, E. and H.J.P. Naguib, *Water sorption in cross-linked poly (vinyl alcohol) networks.* 2003. **44**(5): p. 1647-1653.

140. Takizawa, A., T. Negishi, and K.J.J.o.P.S.P.A.P.C. Ishikawa, *Sorption of water vapor by poly (vinyl alcohol): Influence of polymer crystallinity.* 1968. **6**(3): p. 475-484.

141. Xu, X., et al., *Thermal conductivity of polymers and their nanocomposites.* 2018. **30**(17): p. 1705544.

142. Hu, J., et al., *Polymer composite with improved thermal conductivity by constructing a hierarchically ordered three-dimensional interconnected network of BN.* 2017. **9**(15): p. 13544-13553.

143. Liu, J. and R.J.P.R.B. Yang, *Tuning the thermal conductivity of polymers with mechanical strains.* 2010. **81**(17): p. 174122.

144. Naghavi, M., et al., *A critical assessment on synergistic improvement in PCM based thermal batteries.* 2021. **135**: p. 110259.

145. Mallow, A., O. Abdelaziz, and S.J.I.J.o.T.S. Graham, *Thermal charging performance of enhanced phase change material composites for thermal battery design.* 2018. **127**: p. 19-28.

146. Luo, J., et al., *Battery thermal management systems (BTMs) based on phase change material (PCM): A comprehensive review.* 2022. **430**: p. 132741.

147. Barz, T., et al., *Phenomenological modelling of phase transitions with hysteresis in solid/liquid PCM.* 2019. **12**(6): p. 770-788.

148. Yeon, J.H.J.C. and B. Materials, *Thermal behavior of cement mortar embedded with low-phase transition temperature PCM.* 2020. **252**: p. 119168.

149. Zhou, D., C.-Y. Zhao, and Y.J.A.e. Tian, *Review on thermal energy storage with phase change materials (PCMs) in building applications.* 2012. **92**: p. 593-605.

150. Lin, Y. and X.J.P. Chen, *Moisture sorption–desorption–resorption characteristics and its effect on the mechanical behavior of the epoxy system.* 2005. **46**(25): p. 11994-12003.

151. Ellyin, F., R.J.C.S. Maser, and Technology, *Environmental effects on the mechanical properties of glass-fiber epoxy composite tubular specimens.* 2004. **64**(12): p. 1863-1874.

152. Akay, M., et al., *Influence of moisture on the thermal and mechanical properties of autoclaved and oven-cured Kevlar-49/epoxy laminates.* 1997. **57**(5): p. 565-571.

153. Agresti, F., et al., *Nano-encapsulated PCM emulsions prepared by a solvent-assisted method for solar applications.* 2019. **194**: p. 268-275.

154. Sharifi, N., et al., *Heat pipe-assisted melting of a phase change material.* 2012. **55**(13-14): p. 3458-3469.

155. Maxa, J., A. Novikov, and M.J.M. Nowottnick, *Thermal peak management using organic phase change materials for latent heat storage in electronic applications.* 2017. **11**(1): p. 31.

156. Hallworth, M.A., H.E. Huppert, and R.S.J.J.M.G. Sparks, *Lava flows.* 1987. **11**: p. 93-107.

157. Sharma, R., et al., *Accelerated thermal cycle and chemical stability testing of polyethylene glycol (poly(ethylene glycol)) 6000 for solar thermal energy storage.* 2016. **147**: p. 235-239.

158. Cofer, C.G. and J.J.C. Economy, *Oxidative and hydrolytic stability of boron nitride—A new approach to improving the oxidation resistance of carbonaceous structures.* 1995. **33**(4): p. 389-395.

159. Kostoglou, N., K. Polychronopoulou, and C.J.V. Rebholz, *Thermal and chemical stability of hexagonal boron nitride (h-BN) nanoplatelets.* 2015. **112**: p. 42-45.

160. Zhang, K., et al., *Two dimensional hexagonal boron nitride (2D-hBN): synthesis, properties and applications.* 2017. **5**(46): p. 11992-12022.

161. Cai, Q., et al., *High thermal conductivity of high-quality monolayer boron nitride and its thermal expansion.* 2019. **5**(6): p. eaav0129.

162. Ouyang, T., et al., *Thermal transport in hexagonal boron nitride nanoribbons.* 2010. **21**(24): p. 245701.

163. Tsuchiya, M., T.J.J.o.t.a. Kojima, and calorimetry, *Melting behavior of poly (tetrahydrofuran)-S and their blends.* 2003. **72**(2): p. 651-655.

164. Gill, P., T.T. Moghadam, and B.J.J.o.b.t.J. Ranjbar, *Differential scanning calorimetry techniques: applications in biology and nanoscience.* 2010. **21**(4): p. 167.

165. Serrano, A., et al., *Influence of gelation step for preparing poly(ethylene glycol) – SiO2 shape-stabilized phase change materials by sol–gel method.* 2019. **89**(3): p. 731-742.

166. Cui, Z., et al., *Large scale thermal exfoliation and functionalization of boron nitride.* 2014. **10**(12): p. 2352-2355.

167. Xiao, F., et al., *Edge-hydroxylated boron nitride nanosheets as an effective additive to improve the thermal response of hydrogels.* 2015. **27**(44): p. 7196-7203.

168. Rosely, C.S., et al., *Influence of boron nitride nanosheets on the crystallization and polymorphism of poly (l-lactide).* 2018. **122**(24): p. 6442-6451.

169. Wei, B., et al., *A review of recent progress in preparation of hollow polymer microspheres.* 2009. **6**(3): p. 306-312.

170. Ramli, R.A.J.R.a., *Hollow polymer particles: a review.* 2017. **7**(83): p. 52632-52650.

171. Leung, C.C., I.T.S. Yu, and W.J.T.L. Chen, *Silicosis.* 2012. **379**(9830): p. 2008-2018.

172. Snider Jr, D.E.J.A.R.o.R.D., *The relationship between tuberculosis and silicosis*. 1978, American Lung Association. p. 455-460.

173. Ziskind, M., R.N. Jones, and H.J.A.r.o.r.d. Weill, *Silicosis.* 1976. **113**(5): p. 643-665.

174. Ranabhat, K., et al., *An introduction to solar cell technology.* 2016. **14**(4): p. 481-491.

175. Macdonald, E.K. and M.P.J.P.I. Shaver, *Intrinsic high refractive index polymers.* 2015. **64**(1): p. 6-14.